
Electronic Thesis and Dissertation Repository

3-5-2021 10:30 AM

Effect of Ion Implantation on Mechanical Properties and Kinetic Deformation Mechanisms in Inconel X-750

Loabat Shojaei-Kavan, *The University of Western Ontario*

Supervisor: Klassen, Robert J., *The University of Western Ontario*

A thesis submitted in partial fulfillment of the requirements for the Doctor of Philosophy degree in Mechanical and Materials Engineering

© Loabat Shojaei-Kavan 2021

Follow this and additional works at: <https://ir.lib.uwo.ca/etd>



Part of the [Mechanical Engineering Commons](#)

Recommended Citation

Shojaei-Kavan, Loabat, "Effect of Ion Implantation on Mechanical Properties and Kinetic Deformation Mechanisms in Inconel X-750" (2021). *Electronic Thesis and Dissertation Repository*. 7699.
<https://ir.lib.uwo.ca/etd/7699>

This Dissertation/Thesis is brought to you for free and open access by Scholarship@Western. It has been accepted for inclusion in Electronic Thesis and Dissertation Repository by an authorized administrator of Scholarship@Western. For more information, please contact wlsadmin@uwo.ca.

Abstract

The recent mechanical tests on the ex-service Inconel X-750 spacers have indicated significant embrittlement and reduced load carrying capacity compared to as installed condition. This is an immense safety concern to the nuclear industry, as in-service spacer examination and their replacement within fuel channels are very costly and impractical. The primary degradation mechanism is complex, and thus provides the focus of the current investigation. Despite few previous reports about hardness of non-irradiated and irradiated Inconel X-750, thermally-activated time-dependent deformation conditions have not been studied. This dissertation has attempted to overcome this scarcity of data by providing a series of fundamental investigations involving the use of novel pyramidal nanoscale indentation test techniques to measure the time-dependent plastic deformation of He⁺ at 300 °C and Ni⁺ at 25 °C at different doses separately. Established theories were applied to grain by grain nano indentation testing to assess the hardness of the X-750 alloy under different irradiation doses and temperatures data. Both He⁺ and Ni⁺ ion implantation at lower doses, resulted in softening of the X-750 alloy, however at higher irradiation doses indentation hardness was increased. Constant-load pyramidal indentation tests performed at 25 °C showed that the average indentation stress, σ_{ind} and strain rate $\dot{\epsilon}_{ind}$ increases with decreasing indentation depth and increasing levels of irradiation. The apparent activation energy, ΔG_0 , of the obstacles that limit the rate of dislocation glide during indentation, increased with increased He⁺ implantation dose whereas, it was decreased by increasing Ni⁺ irradiation as irradiation defects increased. On the other hand, apparent activation volume (V^*) and activation area (Δa), decreased by an increased indentation stress for both He⁺ and Ni⁺ irradiated samples. This indicates that the obstacles controlling deformation process are rate sensitive “thermal” obstacles. These approaches are unique to the literature since they demonstrate the individual effect of irradiation damage on mechanical behavior and operative kinetic plastic deformation on irradiated Inconel X-750.

Keywords

Nickel superalloy, heavy ion irradiation, helium implantation, nickel irradiation, nanoindentation hardness, constant loading rate, indentation stress, indentation strain rate, thermal activation energy, thermal activation strength, activation volume, activation area.

Summary for Lay Audience

Canadian deuterium uranium reactors (CANDU) fall into a subset of pressurized heavy water reactors (PHWR) that use heavy water coolant, D_2O , as opposed to H_2O in light water reactor (LWR) designs, as both a moderator and coolant. Helical spring annulus gas spacers in the fuel channels of current CANDU nuclear reactors are made from age-hardened Inconel X-750. Fuel channels are consisting of high temperature Zircalloy pressure tubes (Zr-2.5%Nb), cool Zircalloy-2 calandria tubes, and Inconel X-750 internal spacers that maintain an insulating gap filled with CO_2 gas between the two tubes. These Inconel X-750 garter spring components prevent contact between the two tubes that would otherwise generate a large heat sink and compromise the thermodynamic integrity of the reactor, in addition to causing eventual hydride blistering and rupturing of the pressure tube that could ultimately result in failure and a local loss of coolant accident (LOCA). Neutron irradiation is known to cause microstructural and mechanical property changes within these spacers. Recently, it has been found that these spacers become very brittle after long exposure to neutron irradiation and this is an ongoing concern for the operation of the nuclear reactors. As such the current research aims to use a novel technique of nanoscale mechanical testing to assess the effects of irradiation, temperature and fundamental kinetic deformation parameters in Inconel X-750. The data obtained can be useful in developing models to predict life-time of existing spacers and will also be helpful for the design of the future materials used in garter spring spacers.

Co-Authorship Statement

The research presented in this thesis is composed of three manuscripts, chapter three will be submitted to the journal of Philosophical Magazine A, chapters four and five will be submitted to the journal of Material Science and Engineering A. In all above mentioned chapters, ion implantations of the Inconel X-750 samples were performed by the assistance of Mr. Jack Hendriks at the Tandetron Ion Accelerator facilities and in chapter 3 EBSD scans were obtained by Mr. Ivan Barker at Zircon and Accessory Phase Laboratory (ZAPLab) at Western University. Three manuscripts are co-authored by Loabat Shojaei-Kavan and Prof. Robert J. Klassen. The experiments, analysis of data and manuscript preparation were performed by Loabat Shojaei-Kavan. Professor Klassen contributed by editing all the manuscript and, where necessary providing additional interpretation of data and suggestions for analysis.

Acknowledgments

I wish to express my sincere gratitude to my supervisor professor Robert J. Klassen for the opportunity, patience, and unfailing support throughout this project without which none of this would have been accomplished. His generosity and willingness to give time and feedback is very much appreciated. I also wish to thank my advisory committee, Prof. Jeffrey Wood and Prof. Liyang Jiang for their guidance, useful feedbacks, supports and valuable time during my Ph.D. program. I would like to extend my appreciation to Dr. Mark Daymond from Queen's University for accepting to be my external examiner.

I'd also like to thank Dr. Lyudmila Goncharova and Mr. Jack Hendriks of Western University's ion implantation facility for sample irradiation, Dr. Todd Simpson, and Dr. Sridhar Ramamurthy of Western University's Nanofabrication Laboratory and Surface Science Western (SSW) for Scanning Electron Microscopy (SEM) images, Mr. Ivan Barker at ZAPLab (Department of Earth Sciences) for Electron Backscatter Diffraction (EBSD). I also like to thank all my friends and lab mates at our Micro Mechanical testing laboratory. Also, I sincerely thank the office staff in MME department, especially Ms. Joanna Bloom for her helpful advice. I wish to thank the Natural Science and Engineering Research Council of Canada (NSERC), the University Network of Excellence in Nuclear Engineering (UNENE) and Ontario Graduate Scholarship (OGS) program who provided financial support for this research.

Dedications

To my beloved late mom and dad who taught me love, patience and perseverance

And

To the most precious love of my life, Arash

Table of Contents

Abstract.....	ii
Keywords.....	iii
Summary for Lay Audience.....	iv
Co-Authorship Statement.....	v
Acknowledgments.....	vi
Dedications.....	vii
List of Contents.....	viii
List of Tables.....	xii
List of Figures.....	xiii
List of Abbreviations.....	xx
List of Symbols.....	xxii
Chapter 1.....	1
1 Introduction.....	1
1.1 Ni-based superalloys and radiation effects.....	1
1.2 Inconel X-750 spacers in the CANDU reactor.....	2
1.3 Motivation.....	3
1.4 Research objectives.....	4
1.5 Structure of the thesis.....	5
1.6 References.....	6
Chapter 2.....	8
2 Literature review.....	8

2.1	Inconel X-750.....	8
2.2	Inconel X-750 in CANDU reactor.....	9
2.3	Radiation damage in CANDU reactor.....	10
2.3.1	Fast neutron damage.....	14
2.3.2	Thermal neutron damage.....	15
2.3.3	Production of helium and hydrogen.....	17
2.4	The impact of irradiation damage on the microstructure and mechanical properties of Inconel X-750.....	17
2.4.1	Irradiation hardening.....	18
2.4.2	Irradiation induced defects.....	19
2.4.3	Instability of gamma prime (γ') precipitate.....	29
2.5	Pyramidal indentation testing.....	33
2.5.1	Nano hardness testing.....	33
2.5.2	Basic fundamentals.....	33
2.5.3	Indentation stress.....	37
2.5.4	Indentation strain rate.....	39
2.6	Indentation strain rate and stress.....	39
2.6.1	Constant load rate tests (CLR).....	40
2.7	Indentation size effect (ISE).....	40
2.8	Thermally activated dislocation mechanisms.....	44
2.9	Summary.....	46
2.10	References.....	46
Chapter 3.....		56
3	Effect of high temperature He ⁺ and room temperature Ni ⁺ implantation on grain by grain indentation hardness of Inconel X-750.....	56
3.1	Introduction.....	56
3.2	Experimental procedure.....	57
3.2.1	Test material.....	57
3.2.2	Ion implantation.....	58

3.2.3	Electron Backscatter Diffraction (EBSD).....	60
3.2.4	Nanoindentation hardness testing.....	60
3.2.5	Microstructure evaluation.....	62
3.3	Results and discussion.....	62
3.3.1	Effect of irradiation damage on the hardness of Inconel X-750.....	62
3.3.2	Effect of helium accumulation on the hardness of Inconel X-750.....	65
3.3.3	Indentation size effect in unirradiated vs. irradiated material.....	66
3.4	Conclusion.....	72
3.5	Acknowledgments.....	73
3.6	References.....	73
Chapter 4.....		79
4	Effect of high temperature He ⁺ implantation on the kinetic deformation nanoindentation of Inconel X-750.....	79
4.1	Introduction.....	79
4.2	Experimental procedure.....	81
4.2.1	Test material.....	81
4.2.2	Ion implantation.....	81
4.2.3	Nanoindentation testing.....	82
4.3	Results.....	82
4.3.1	Calculation of projected area function of indentation.....	82
4.3.2	Indentation force -depth (<i>P-h</i>) plots.....	83
4.3.3	Indentation stress σ_{ind} versus indentation depth, <i>h</i>	85
4.3.4	Microstructure evaluation.....	87
4.4	Discussion.....	88
4.4.1	Obstacle-limited thermally-activated dislocation glide.....	88
4.4.2	Mechanism of indentation deformation.....	88
4.4.3	Apparent activation strength and activation volume.....	91
4.4.4	Haasen plot activation analysis.....	95
4.5	Conclusion.....	98
4.6	Acknowledgements.....	99

4.7	References.....	99
Chapter 5	104
5	Nano- scale kinetic deformation behavior of room temperature Ni ⁺ irradiated Inconel X-750.....	104
5.1	Introduction.....	104
5.2	Experimental procedure.....	106
5.2.1	Material preparation and ion implantation.....	106
5.2.2	Nano indentation testing.....	107
5.2.3	Microstructure evaluation.....	108
5.3	Results.....	109
5.3.1	Indentation load -depth (<i>p-h</i>) plots.....	109
5.3.2	Indentation depth dependence of σ_{ind}	111
5.3.3	Indentation strain rate $\dot{\epsilon}_{ind}$ versus indentation depth, <i>h</i>	113
5.3.4	Indentation stress σ_{ind} indentation strain rate, $\dot{\epsilon}_{ind}$	113
5.4	Discussion.....	114
5.4.1	Mechanism of indentation deformation.....	114
5.4.2	Apparent activation strength and activation volume.....	117
5.4.3	Haasen plot activation analysis.....	121
5.5	Conclusion.....	124
5.6	Acknowledgements.....	125
5.7	References.....	125
Chapter 6	133
6	Conclusions and future scope.....	133
6.1	Conclusions.....	133
6.2	Suggestion for future work.....	135
Curriculum vitae	137

List of Tables

Table 3-1 Chemical Composition of the Inconel X-750 (wt.%) [7].....	58
Table 3-2 The measured values of H_0 (GPa) and h^* (nm) versus irradiation doses.....	70

List of Figures

Figure 1.1: CANDU fuel channel with Inconel X-750 spacer coil highlighted [11].....	3
Figure 2.1: Schematic presentation of (a) γ (matrix) (b) γ' (gamma prime lattice structure) [21].....	9
Figure 2.2: Cross section schematic of a fuel channel in a CANDU reactor [22, 24].....	10
Figure 2.3: Spacer operation temperature with respect to pressure tube and calandria tube [24].....	10
Figure 2.4: Number ν_d of displaced atoms in the cascade as function of the PKA energy according to Kinchin-Pease model [25].....	12
Figure 2.5: SRIM output plots illustrate: (a) damage profile of 8 MeV Ni^+ in Inconel X-750 (b) ion range in target Inconel X-750 (c) Dislocations of 8 MeV Ni ions irradiating in Inconel X-750, shows the cascade dislocations of 3000 simulated ions.....	13
Figure 2.6: Neutron flux vs. neutron energy experienced by the Inconel X-750 spacer [22].....	15
Figure 2.7: DPA calculations for an average bundle power CANDU channel [23].....	16
Figure 2.8: Calculated productions of Helium and Hydrogen in an average power CANDU channel [23].....	17
Figure 2.9: TEM image of microstructure induced by irradiation at 600 °C to 0.27 dpa (a) $1/3\langle 111 \rangle$ type faulted Frank loops (b) $1/2\langle 110 \rangle$ perfect loops [13].....	20

Figure 2.10: Weak beam dark field micrograph showing the evolution irradiation induced lattice defects in (a) 6 o'clock (b) in 12 o'clock location [24].....	21
Figure 2.11: The defect size distribution in ex-service X-750 spacer at both 6 and 12 o'clock locations [24].....	21
Figure 2.12: Defect density variation as a function of irradiation dose at different temperatures [13].....	22
Figure 2.13: TEM micrograph close to zone axis [011] and $g = 200$ showing formation of SFT _s (a) 0.27 dpa at 60 °C (b) 0.27 dpa at 400 °C during irradiation with 1 MeV Kr ⁺² [12].....	23
Figure 2.14: Cavity size distribution in pinched and un-pinched region in ex-service X-750 spring spacer [8].....	24
Figure 2.15: TEM bright field micrograph showing cavity evolution at (a)12 o'clock [24] (b) 6 o'clock location [22].....	24
Figure 2.16: TEM micrographs showing cavity microstructures after irradiation to 5.4 dpa at 300 °C with (a) 200 appm helium (b) 5000 appm helium at room temperature [14].....	25
Figure 2.17: Under focus bright field micrographs showing cavity formation after helium implantation at 400 °C (a) 400 appm (b) 1000 appm (c) 5000 appm [15].....	27
Figure 2.18: Cavity density and cavity size, against amount of injected helium [15].....	27
Figure 2.19: The yield strength of Ni implanted with helium at the indicated temperatures plotted versus the cube root of helium concentration [48].....	29

Figure 2.20: (a) Disorder kinetics of γ' (b) Post-irradiation ChemiSTEM mapping of γ' precipitates after irradiation at 300 °C up to 0.06 and 5.4 dpa [24].....31

Figure 2.21: Microhardness of irradiated Inconel 718 as a function of irradiation dose [52].....32

Figure 2.22: Percent change in hardness at 150 nm contact depth, relative to the unirradiated material, for Inconel 718 as a function of Fe-only and from triple-beam irradiation [59].....32

Figure 2.23: High-magnification SEM scan of the tip of a Berkovich diamond indenter [62].....33

Figure 2.24: (a) Schematic illustration of indentation load–displacement curve [63] (b) unloading process showing parameters characterizing the contact geometry [64]34

Figure 2.25: Schematic representation of pile-up and sink-in [71].....38

Figure 2.26: Hardness variation as a function of indentation depth, showing the ISE in Cu [81].....41

Figure 2.27: Schematic representation of the Nix-Gao model for conical indenters [86].....42

Figure 2.28: A plot of H^2 vs. $1/h$ for (a) Cu [84] (b) Ag [87].....43

Figure 3.1: SEM image of chemically etched sample of the X-750 alloy which contains twins and inclusions as incoherent carbides (TiC, NbC) and small carbides (MC) Cr_{23}C_658

Figure 3.2: (a) Schematic illustration of irradiation and indentation direction with SRIM profile for He^+ and Ni^+ irradiation (b) He^+ and Ni^+ conditions along with number of ions (c) Ni^+ ion irradiation, depicting displacement damage dose variation vs target depth for samples

irradiated up to $\psi_{Ni} = 5$ dpa with thirteen kinetic energy levels ($E_{Ni^+} = 2- 8$ MeV) (d) SRIM simulation for helium implantation, showing helium concentration as a function of target depth with fourteen consecutive He^+ ion implantation energies ($E_{He^+} = 0.3 - 1.6$ MeV).....59

Figure 3.3: $500 \times 350 \mu m$ EBSD map of crystal orientation of an Inconel X-750 for as-received sample ($C_{He} = 0$ appm, $\psi_{Ni} = 0$ dpa). The location of nine indentations are shown by white circles.....61

Figure 3.4: Average indentation hardness versus ion irradiation damage for the Inconel X-750 samples $\psi_{Ni} = 0.01, 0.1, 1,$ and 5 dpa for both series and grain by grain hardness testing at 400 nm depth. Error bars represent the measurement of the amount of variation of hardness data for 10 to 12 indents for both experiments63

Figure 3.5: Average indentation hardness versus defect density. Defect density data assumed equivalent to those reported in from [25].....64

Figure 3.6: Average indentation hardness versus accumulated helium content for the Inconel X-750 samples $C_{He} = 100, 1000, 5000$ appm for both series and grain by grain hardness testing. Error bars represent the measurement of the amount of variation of hardness data for 10 to 12 indents for both experiments65

Figure 3.7: Average indentation hardness versus cavity size. TEM cavity size data were extracted from [11].....66

Figure 3.8: Indentation hardness as a function of indentation depth and ISE behaviour for (a) as-received (b) $\psi_{Ni} = 0.1$ dpa (c) $C_{He} = 1000$ appm. The error bars represent the measurement of the amount of variation of hardness data.....68

Figure 3.9: The characteristic indentation depth (h^*) reflecting the ISE of the measured hardness versus (a) C_{He} (appm) (b) ψ_{Ni} (dpa) (c) cavity size (d) cavity density (e) defect density.....71

Figure 4.1: SRIM simulation for helium implantation, showing helium concentration as a function of target depth.....82

Figure 4.2: Images (SEM) of Berkovich indenter that was used in present study: radius of indenter tip is 250.8 nm.....83

Figure 4.3: Representative indentation force P versus depth h curves for the tested Inconel X-750 alloy subjected to various levels of implanted helium concentration: (a) $C_{He} = 0$ (b) $C_{He} = 100$ appm (c) $C_{He} = 1000$ appm (d) $C_{He} = 5000$ appm.85

Figure 4.4: Average indentation stress σ_{ind} versus indentation depth h for the tested Inconel X-750 alloy subjected to various levels of implanted helium concentration: (a) $C_{He} = 0$ (b) $C_{He} = 100$ appm (c) $C_{He} = 1000$ appm (d) $C_{He} = 5000$ appm.....87

Figure 4.5: Plots of activation energy $\Delta G_{Thermal}$ versus τ_{equiv} for (a) $C_{He} = 0$ (b) $C_{He} = 100$ appm (c) $C_{He} = 1000$ appm (d) $C_{He} = 5000$ appm.....91

Figure 4.6: Apparent activation strength ΔG_0 of obstacles that limit dislocations glide versus helium concentration C_{He} (appm).....93

Figure 4.7: (a) Cavity size (nm) (b) density versus C_{He} (appm). Cavity size and density data are determined from [10].....93

Figure 4.8: Normalized activation volume, V^*/b^3 , versus indentation depth for tests performed at $\dot{P} = 0.3$ mN/s for different helium concentrations.....94

Figure 4.9: (a) Normalized activation volume, V^*/b^3 , at $\dot{P}= 0.3$ mN/s for different helium concentrations versus cavity size (nm) (b) and as cavity density as data are determined from [10].....95

Figure 4.10: $b^2/\Delta a$ versus τ_{equiv} for the indentation test performed on (a) $C_{He} = 0$ (b) $C_{He} = 100$ appm (c) $C_{He} = 1000$ appm (d) $C_{He} = 5000$ appm.....97

Figure 4.11: $b^2/\Delta a$ versus τ_{equiv} at 400 nm depth for different He⁺ implanted and as-received samples.....98

Figure 4.12: $b^2/\Delta a$ versus He⁺ concentration (appm) and as-received samples at 400 nm depth.....98

Figure 5.1: (a) Schematic illustration of irradiation and indentation direction with SRIM profile (b) Displacement damage profile versus target depth for samples irradiated up to $\psi_{Ni} = 5$ dpa.....107

Figure 5.2: Representative indentation force P versus depth h curves for the tested Inconel X-750 alloy subjected to various levels of Ni⁺ irradiation damages, in (a) $\psi_{Ni}= 0$ (b) $\psi_{Ni}= 0.1$ (c) $\psi_{Ni}= 1$ (d) $\psi_{Ni}= 5$110

Figure 5.3: Average indentation stress σ_{ind} versus indentation depth for all levels of irradiation damage materials, indented at three loading rates, in (a) $\psi_{Ni}= 0$ (b) $\psi_{Ni}= 0.1$ (c) $\psi_{Ni}= 1$ (d) $\psi_{Ni}= 5$ dpa.....112

Figure 5.4: Apparent average indentation strain rate $\dot{\epsilon}_{ind}$ versus indentation depth for as-received sample as indented at three loading rates. The shape of the curve is the same for the all irradiated Inconel X-750 at different dpa.....113

Figure 5.5: Logarithmic plot of σ_{ind} versus $\dot{\epsilon}_{ind}$ at loading rate of $\dot{P} = 0.3$ mN/s for all samples.....114

Figure 5.6: Plots of activation energy $\Delta G_{Thermal}$ versus τ_{equiv} for (a) $\psi_{Ni}= 0$ (b) $\psi_{Ni}= 0.1$ (c) $\psi_{Ni}= 1$ (d) $\psi_{Ni}= 5$ dpa.....	116
Figure 5.7: Apparent activation strength ΔG_0 of obstacles that limit dislocations glide versus defect density. Defect density data were determined from [11].....	118
Figure 5.8: Normalized activation volume, V^*/b^3 , versus indentation depth for tests performed at $\dot{P}= 0.3$ mN/s for different conditions.....	119
Figure 5.9: Normalized activation volume, V^*/b^3 , versus average indentation stress τ_{equiv} for tests performed at $\dot{P}= 0.3$ mN/s.....	119
Figure 5.10: Defect density versus ψ_{Ni} (dpa) as defect density data is determined from [11].....	120
Figure 5.11. Normalized activation volume, V^*/b^3 versus defect density. Defect density data is extracted from [11].....	121
Figure 5.12: $b^2/\Delta a$ versus τ_{equiv} for the indentation test performed on (a) $\psi_{Ni}= 0$ (b) $\psi_{Ni}= 0.1$ (c) $\psi_{Ni}= 1$ (d) $\psi_{Ni}= 5$ dpa.....	123
Figure 5.13: $b^2/\Delta a$ versus τ_{equiv} at 400 nm depth for different Ni^+ irradiated and as-received samples.....	123
Figure 5.14: $b^2/\Delta a$ versus dpa for different levels and as-received samples at 400 nm depth.....	124

List of Abbreviations

Abbreviations	Definition
APB	Anti Phase Boundary
appm	Atomic parts per million
CANDU	Canadian Deuterium Uranium Reactor
CLR	Constant Load Rate
dpa	Displacement Per Atom
EBS	Electron Back Scattered Diffraction
FCC	Face Centered Cubic
FIB	Focus Ion Beam
GND	Geometrically Necessary Dislocation
ISE	Indentation Size Effect
K-P	Kinchin-Pease
LWR	Light Water Reactor
PHWR	Pressurized Heavy Water Reactor
PKA	Primary Knock on Atom
SEM	Scanning Electron Microscope
SFT	Stacking Fault Tetrahedra
SRIM	Stopping Range of Ions in Matter software

SSD

Statistically Stored Dislocation

TEM

Transmission Electron Microscope

List of Symbols

Symbols	Definition
T_{melt}	Melting temperature
E_d	Threshold displacement energy
E_i	Energy of incident particle
E_c	Energy loss by electron stopping
m	Mass of incident particle
M	Mass of stationary atom
θ_s	Scattering angle in a collision system
γ	Maximum recoil energy
T	PKA energy
T_{max}	Maximum PKA energy
E_k	Kinetic energy
ν_d	Number of displaced atoms
φ	Incident ion fluence (ion/cm ²)
D	Vacancy production rate (vacancy/ion/Å)
N	Atomic density (atom/cm ³)
H	Indentation hardness
M	Taylor factor

σ_y	Yield stress
h	Indentation depth
σ_{ind}	Indentation stress
$\dot{\gamma}_{ind}$	Indentation shear strain rate
$\dot{\epsilon}_{ind}$	Indentation strain rate
h^*	Characteristic depth
ψ	Irradiation damage
C_{He}	Helium concentration
V^*	Apparent activation volume
Δa	Apparent activation area
$\Delta G_{Thermal}$	Thermal activation energy
σ_{equiv}	Equivalent Stress
τ_{equiv}	Equivalent shear stress
τ_{ind}	Indentation shear stress
$\dot{\gamma}_{equiv}$	Equivalent shear strain rate
ΔG_0	Apparent activation strength
b	Burger vector
μ	Elastic modulus
ρ_d	Defect density
E_R	Reduced elastic modulus

Chapter 1

1 Introduction

1.1 Ni-based superalloys and radiation effects

Ni-based superalloys possess excellent strength and creep properties in addition to oxidation and corrosion resistance at high temperatures. In the case of age-hardened Ni-based superalloys, their remarkable high temperature strength is attributed to the presences of γ' - ($\text{Ni}_3 [\text{Al}, \text{Ti}]$) or γ'' - ($\text{Ni}_3 [\text{Nb}, \text{Ti}]$) precipitates in the microstructure [1]. Therefore, they are regarded as good candidates for core components of nuclear reactors. For instance, Inconel 718 was successfully employed as bolts, grid spacers of fuel elements, and springs in fission reactors [2], and Inconel 600 is used as a part of flux detectors in CANDU reactors [3, 4]. The Ni based superalloy of Inconel X-750 is used for fasteners and centering pins in the core of pressurized water reactors, boiling water reactors, in CANDU fuel channels as spacers and also tensioning springs at the periphery of reactors [4]. Exposure to neutrons can result in microstructural changes to Ni-based superalloys by two mechanisms; 1) neutron-induced atomic displacement, which causes the metal to become hardened and to lose ductility, and 2) neutron-induced helium accumulation via the $^{58}\text{Ni}(n,\gamma)^{56}\text{Fe}$ transmutation process, which causes the metal to become embrittled. It is well known that the radiation damage from fast neutrons causes significant changes in microstructure and consequent mechanical properties of component materials in the reactors. Lattice displacement due to atomic collisions with high energy neutrons can introduce different types of defects of crystalline structure including; dislocation loops, cavities and other tiny unidentified defects. Hence, the microstructure changes may alter the mechanical properties through hardening of the material, reduced ductility and fracture toughness [5-7]. In addition, radiation damage of fast neutrons may affect the stability of the strengthening precipitates. In Ni based superalloys, any instability (disordering/dissolution) in γ' -precipitates can lead to significant degradation in mechanical properties. Apart from fast neutron induced displacements, Ni-based superalloys are subjected to thermal neutron irradiation in thermal reactors such as the CANDU reactor through (n, α) or (n, p) nuclear transmutations [28,29]. These nuclear

reactions result in considerable concentrations of helium and hydrogen, which will additionally affect nucleation of cavities [8, 9].

Owing to the relevance to nuclear industry and engineering materials, the irradiation damage effects on structure and properties of pure face centered cubic (FCC) metals are of great interest and have been the subject of study for many years. However, there is still a lack of understanding of the basic mechanisms underlying irradiation induced damages in some commercial Ni-based superalloys such as Inconel X-750 [3-5].

1.2 Inconel X-750 spacers in the CANDU reactor

The core of Canadian Deuterium Uranium (CANDU) reactor contains around four hundred horizontal fuel channels arranged inside a large, cylindrical, steel calandria vessel. Each fuel channel contains a hot pressure tube (operating at 260°C-310°C) surrounded by an insulating gas gap (CO₂) that separates it from a cool calandria tube (operating at 60 °C to 70 °C). Both tubes are made from zirconium alloys. Helical garter spring spacers, made from the Ni-based Inconel X-750 alloy, are stretched around the pressure tube at four locations along the tube to prevent it from touching the calandria tube (Figure 1.1). The annular gap between the calandria tube and the pressure tube is filled with flowing CO₂ for the purpose of detecting the presence of moisture if leaks develop [10]. Contact between the tubes would lower the efficiency of the reactor by allowing heat transfer from the hot pressure tube to the cool calandria tube and may result in a safety issue involving hydride formation and cracking of the pressure tube. Modern CANDU spacers are garter springs tightly fitted onto the pressure tube that maintain an insulating gap between the hot Zr-2.5% Nb pressure tube and the cool Zircalloy-2 calandria tube. After time in-service, due to the combined weight of the fuel bundle and heavy water coolant, the pressure tube creeps and sags with respect to the calandria tube. Spacers provide support to the hot pressure tubes, at four locations separating them from the cold calandria tubes and withstand the pressure tubes from creep deformation.

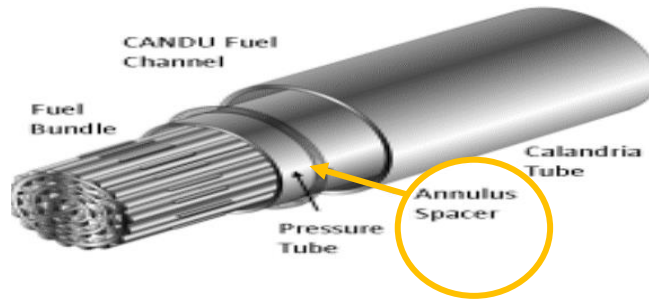


Figure 1.1: CANDU fuel channel with Inconel X-750 spacer coil highlighted [11].

1.3 Motivation

It was reported that the ex-service CANDU Inconel X-750 spacers become severely brittle and no longer function properly as planned over a long time exposure inside reactor [32]. The CANDU industry has initiated research to address the aging of Inconel X-750 spacers in order to determine service conditions for risk assessment, to understand the conditions responsible for material degradation and to demonstrate fitness-for-service. Although spacers were never found to have failed in-service, upon handling for inspections for post irradiation examination experiments they suddenly fractured.

While the main mechanisms underlying the irradiation-induced damage are not well known, TEM based studies of the microstructural stability of irradiated Inconel X-750 indicated the correlation between irradiation doses, temperature, and helium concentration on the type of irradiation induced damage formed in the material [8, 12-15]. In order to simulate the neutron irradiation induced damage over a wide range of temperatures, heavy ion irradiation is employed instead of using reactor neutrons. Previous studies have shown that heavy ion bombardment can be used to create crystallographic damage consisting of dislocation loops similar in size and nature to that produced by neutron irradiation of metals [12, 16]. The benefit of using Ni^+ irradiation for this research is the production of defects without causing significant chemical composition change to the test material which also stays non-radioactive after irradiation. Another benefit is the production of damage at a very fast rate. It takes about 3 hours for Ni^+ to produce 5 dpa of damage to the top several micron thick layer of Inconel X-750 material, whereas neutron irradiation takes about 5

years to produce the same amount of damage. While studies are still ongoing to understand the relationship of these mechanisms, experimental data to measure the effect of these mechanisms on the mechanical properties of Inconel X-750 alloy are still insufficient. Also, there is insufficient data to correlate the microstructural changes to the kinetic deformation mechanism via stress and strain analysis. Development of such a correlation remains the necessary missing link before accurate predictions of garter spring spacer lifetime as a function of in-reactor location and irradiation history can be made.

1.4 Research objectives

To address the aforementioned research needs, the primary theme of this research is to apply the pyramidal indentation test techniques to investigate the effect of helium accumulation and irradiation induced damage, by using He^+ and Ni^+ implantation at high and room temperatures and to study the kinetics of local plastic deformation on the mechanical properties, to assess the effect of indentation stress and strain, strength of the obstacles, and deformation volume during plastic deformation.

The objectives of this study are:

1. To study the effect of He^+ accumulation and Ni^+ crystallographic defects on the indentation depth dependence of the hardness of Inconel X-750 via grain by grain nano indentation technique.
2. To investigate the indentation size effect (ISE) in un-irradiated X-750 and explore the effect of irradiation-induced defects on ISE.
3. To study the effect of He^+ and Ni^+ implantation on the operative deformation kinetics of Inconel X-750; namely, to determine their effect on the apparent activation strength and activation volume of the deformation rate controlling obstacles within the microstructure.

1.5 Structure of the thesis

The research in this dissertation will be presented in manuscript format. Three individual manuscripts will be submitted to journals are included. Each part of the work will be introduced individually in the following chapters by the School of Graduate and Postdoctoral Studies at Western University. The dissertation contains 6 chapters, 3 of which contain detailed description of different investigations carried out in this research.

Chapter 2 of this thesis contains a review of published literature on the theories, mechanisms and techniques which were applied to achieve the objective of this study. Description of the radiation-induced damage and its general effect on the mechanical properties of metals, particularly Ni-based superalloys, and FCC metals, are also included.

Chapter 3 presents the results of a study of the effect of high temperature He⁺ and room temperature Ni⁺ implantation on grain by grain indentation hardness of Inconel X-750 and effect of irradiation induced defects on ISE.

Chapter 4 presents the effect of high Temperature He⁺ implantation on the kinetic deformation nanoindentation of Inconel X-750 during constant-load pyramidal nanoindentation of Inconel X-750.

Chapter 5 reports nano- scale kinetic deformation behavior of room temperature Ni⁺ irradiated Inconel X-750.

Finally, general, and specific conclusions drawn from the research along with recommendations for future research are presented in Chapter 6.

1.6 References

- [1] M. Stopher, The effects of neutron radiation on nickel-based alloys, *Materials Science and Technology* 33(5) (2017) 518-536.
- [2] J. Hunn, E. Lee, T. Byun, L. Mansur, Ion-irradiation-induced hardening in Inconel 718, *Journal of nuclear materials* 296(1-3) (2001) 203-209.
- [3] M. Griffiths, G. Bickel, S. Douglas, Irradiation-induced embrittlement of INCONEL 600 flux detectors in CANDU reactors, 18th International Conference on Nuclear Engineering, American Society of Mechanical Engineers Digital Collection, 2010, pp. 293-298.
- [4] O. Woo, C. Judge, H. Nordin, D. Finlayson, C. Andrei, The microstructure of unirradiated and neutron irradiated Inconel X750, *Microscopy and Microanalysis* 17(S2) (2011) 1852-1853.
- [5] Z. Yao, R. Schäublin, M. Victoria, The microstructure and tensile properties of pure Ni single crystal irradiated with high energy protons, *Journal of nuclear materials* 307 (2002) 374-379.
- [6] I. Robertson, J. Vetrano, M. Kirk, M. Jenkins, On the formation of vacancy type dislocation loops from displacement cascades in nickel, *Philosophical Magazine A* 63(2) (1991) 299-318.
- [7] R. Holt, M. Griffiths, R. Gilbert, c-Component dislocations in Zr-2.5 wt% Nb alloy, *Journal of Nuclear Materials* 149(1) (1987) 51-56.
- [8] H.K. Zhang, Z. Yao, G. Morin, M. Griffiths, TEM characterization of in-reactor neutron irradiated CANDU spacer material Inconel X-750, *Journal of Nuclear Materials* 451(1-3) (2014) 88-96.
- [9] M. Griffiths, The effect of irradiation on Ni-containing components in CANDU® reactor cores: a review, *Nuclear Review* 2(1) (2014) 1-16.

- [10] G.S. Was, Fundamentals of radiation materials science: metals and alloys, springer2016.
- [11] <http://www.civil.uwaterloo.ca/watrisk/research.html>.
- [12] H.K. Zhang, Z. Yao, C. Judge, M. Griffiths, Microstructural evolution of CANDU spacer material Inconel X-750 under in situ ion irradiation, Journal of Nuclear Materials 443(1-3) (2013) 49-58.
- [13] H.K. Zhang, Z. Yao, M.R. Daymond, M.A. Kirk, Elevated temperature irradiation damage in CANDU spacer material Inconel X-750, Journal of Nuclear Materials 445(1-3) (2014) 227-234.
- [14] H. Zhang, Z. Yao, M.R. Daymond, M.A. Kirk, Cavity morphology in a Ni based superalloy under heavy ion irradiation with cold pre-injected helium. I, Journal of Applied Physics 115(10) (2014) 103508.
- [15] H. Zhang, Z. Yao, M.R. Daymond, M.A. Kirk, Cavity morphology in a Ni based superalloy under heavy ion irradiation with hot pre-injected helium. II, Journal of Applied Physics 115(10) (2014) 103509.

Chapter 2

2 Literature review

Nickel-based superalloys have emerged as the material of choice when significant resistance to loading under static, fatigue and creep conditions and high temperature is required. This is particularly true when operating temperatures are beyond about 800 °C [1, 9, 10]. Consequently, Ni-based superalloys have been proposed as structural materials in next generation nuclear reactors due to their superior high-temperature mechanical properties and corrosion resistance [17, 18]. The strength of Ni-based superalloys in most cases originates from presence of γ' (Ni_3 [Al, Ti]) precipitates, having the FCC $L1_2$ structure and γ'' (Ni_3 [Ti, Nb]), possessing the HCP (hexagonal-close-packed structure) DO_{22} structure. Inconel X-750, a Ni-based superalloy, is precipitation hardened with γ' phase and is used for fasteners and centering pins in the cores of pressurized and boiling water reactors. It is also used in CANDU fuel channels as spacers as well as tensioning springs at the periphery of reactors [9]. This chapter reviews previously published findings related to Inconel X-750 and its use within CANDU nuclear reactors. This is followed by a review on the effect of irradiation-induced changes in microstructure of Ni-based superalloys and their effect on mechanical properties of FCC metals.

2.1 Inconel X-750

Inconel X-750, a Ni-based super-alloy with high strength and creep resistance, is a widely used super-alloy at elevated temperature approaching $0.8T_{\text{melt}}$ in CANDU reactors [19, 20]. The material contains approximately 70 wt.% Ni, and of this; approximately 68% is the isotope ^{58}Ni , which has a high thermal neutron capture cross section. The microstructure of the age hardened X-750 consists of equiaxed grains of the FCC γ -matrix with mean grain size of 15 - 45 μm . The microstructure observations show that two types of carbides can be detected, including large micron-sized MC ((Ti, Nb) C) within the matrix grains and smaller $M_{23}C_6$ (Cr_{23}C_6) carbides which are located mostly on grain boundaries. $\text{Ni}_3(\text{Al, Ti})$ or gamma prime (γ'), is the most important strengthening precipitate in X-750 [20]. It is in a form of coherent precipitates with an $L1_2$ ordered structure which has a small lattice

misfit (0.5%) with γ -matrix from the face center cubic (FCC) γ matrix due to the solute aggregates, Al and Ti [8]. Schematic FCC crystal structure of γ' is presented in (Figure 2.1) in which the Ni atoms are located at the face centers and the aluminum or titanium atoms are at the cube corners.

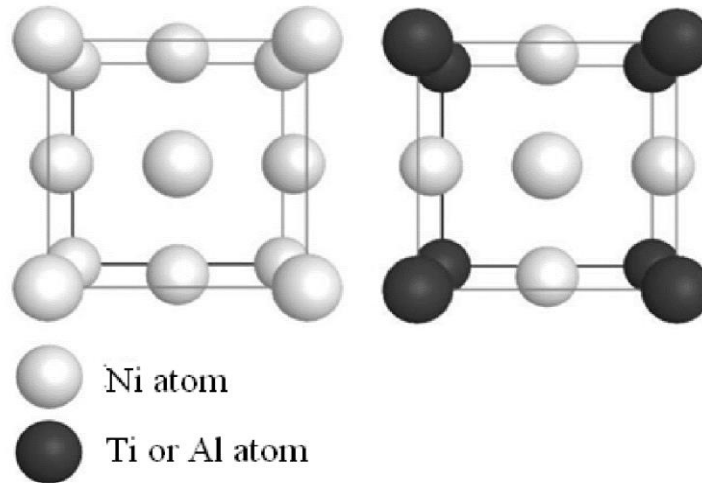


Figure 2.1: Schematic presentation of (a) γ (matrix) (b) γ' (gamma prime lattice structure) [21].

2.2 Inconel X-750 in CANDU reactor

In CANDU reactors, the X-750 alloy is used as a fuel channel spacer material which separates the Zr-2.5wt%Nb hot pressure tube from Zircaloy-2 cold calandria tube preventing the formation of hydrides and blisters in pressure tube (Figure 2.2) [22-24]. Each CANDU reactor contains about 380 fuel channels with four spacers per channel. This means there are about 1520 X-750 spacers in every reactor [10]. After time in-service, due to the combined weight of the fuel bundle and heavy water coolant, the pressure tube creeps and sags with respect to the calandria tube, “pinching” the spacer between the hot pressure tube and cold calandria tube [8, 12, 13, 22, 23]. This creates a circumferential temperature variation around the spacer. At 6 o’clock location, where the spacer is ‘pinched’ to both pressure tube and calandria tube, the spacer temperature is 120 °C- 280 °C. At 12 o’clock location where the spacer is ‘non-pinched’ to the calandria tube, the operation temperature is 300 °C- 330 °C (Figure 2.3). The variability in the pinched material results from local

contact points at the bottom of the fuel channel; locations in direct contact with the pressure tube operate close to the higher bound temperature, 280 °C, and locations in direct contact with the calandria tube operate close to the lower bound temperature, 105 °C.

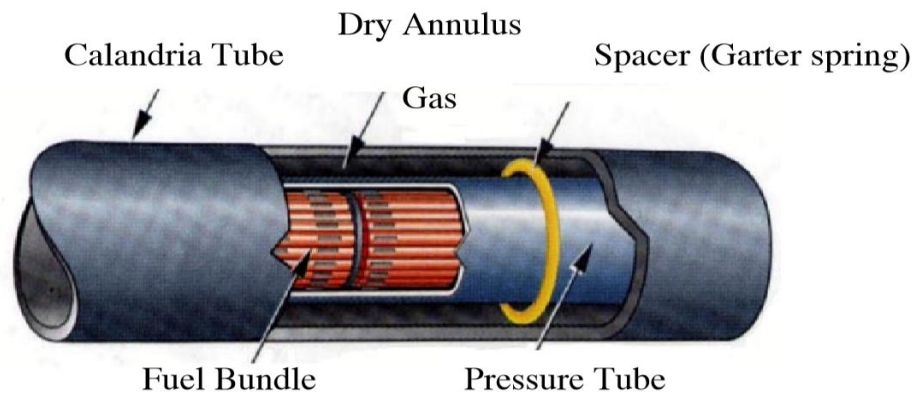


Figure 2.2: Cross section schematic of a fuel channel in a CANDU reactor [22, 24].

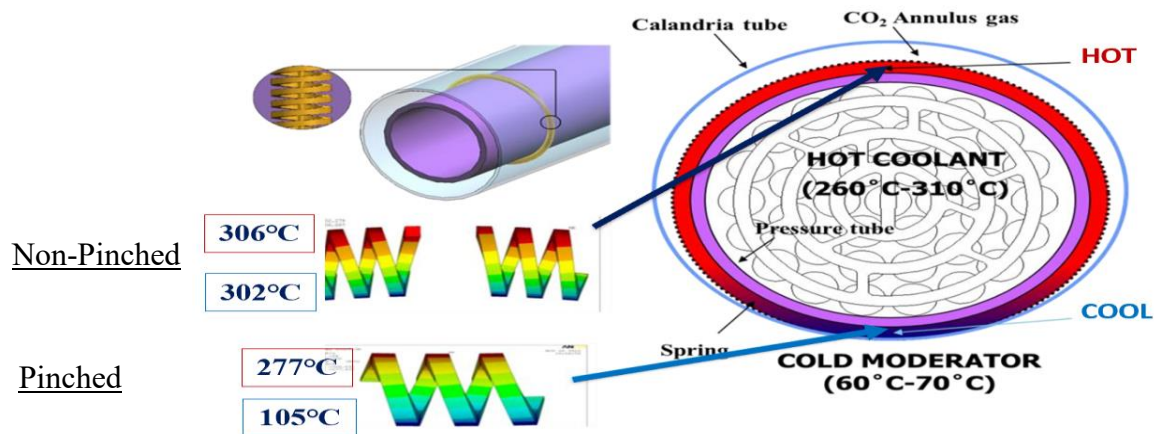


Figure 2.3: Spacer operation temperature with respect to pressure tube and calandria tube [24].

2.3 Radiation damage in CANDU reactor

Radiation damage is the result of redistribution in atoms of the target metal structure caused by the transfer of energy. There are several steps in development of radiation damage including: interaction of an energetic particle with a lattice atom followed by transfer of

kinetic energy to the lattice atom causing a primary knock-on atom (PKA). This in turn results in the displacement of atom and its passage through the lattice and subsequent additional knock-on atoms. The displacement cascade will finally end leaving primary knock-on atom as an interstitial. [25]. Described processes would result in formation vacancies and interstitials (Frenkel pairs) altering the structural and mechanical properties of irradiated materials. The energy of the PKA depends on the mass and the energy of incident particle which is given by:

$$T = \frac{\gamma}{2} E_i (1 - \cos \theta) \quad (2.1)$$

where E_i is the energy of incident particle and θ is the scattering angle for incident particle while γ is the maximum recoil energy which is defined as:

$$\gamma = \frac{4mM}{(m + M)^2} \quad (2.2)$$

where m and M is the mass of incident particle and PKA, respectively. Many models were developed to quantify the number of atoms displaced by one PKA. The most frequently used model is that of Kinchin-Pease (referred to here as the K-P model) [26]. In this model the minimum energy required for an atom displacement during collision is called threshold displacement energy (E_d). The magnitude of E_d varies and is dependent on the structure of lattice, the direction of PKA and the thermal energy of the lattice [25]. However, Kinchin and Pease [26] proposed a theory to calculate the average number of displaced atoms initially created by PKA of energy T which is described in Eq. 2.3 where E_c is the energy loss by electron stopping.

$$v_d = \begin{cases} 0 & \text{for } T < E_d \\ 1 & \text{for } E_d < T < 2E_d \\ \frac{T}{2E_d} & \text{for } 2E_d < T < E_c \\ \frac{E_c}{2E_d} & \text{for } T \geq E_c \end{cases} \quad (2.3)$$

If the PKA energy is greater than E_c no additional displacements occur until electron energy losses reduce the PKA energy to E_c . For all energies less than E_c , electronic stopping is ignored, and only atomic collisions occur. Between E_d and E_c , however, there is a linear relationship between the PKA energy and the number of displaced atoms (Frenkel pairs) produced (Figure 2.4).

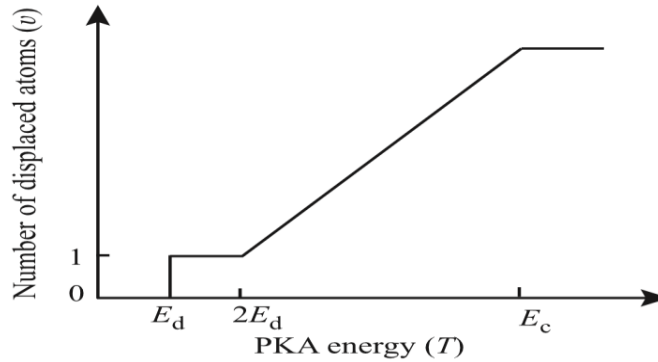


Figure 2.4: Number ν_d of displaced atoms in the cascade as function of the PKA energy according to Kinchin-Pease model [25].

Displacement Per Atom (dpa) or particle induced atomic displacement damage is a measure of the number of times an atom is displaced from its lattice position by collision of a single particle (neutron or ion) with a specific kinetic energy. The extent that high energy incident ions deflect and displace the atoms of the target substrate is assessed by computation. The most common software used for this is the SRIM (Stopping and Range of Ions in Materials) software [9, 20, 21, 23, 27]. SRIM is a collision approximation model that employs a Monte Carlo simulation to estimate probabilistic values for ion-atom interactions. It uses the Kinchin-Pease formula to estimate the number of atom knock-outs per incident ion. Basically, SRIM software is used to calculate the dpa as a function of particle penetration depth. The software works by running thousands of ion-atom interaction simulations, each expressed in terms of the Kinchin-Pease model, and predicts the resulting ion path and atom-displacement events. From each simulated ion implantation, SRIM calculates the mean, and variance of the penetration depth and the number of ion-induced displacements (i.e. irradiation damage events) of the substrate atom. SRIM input information like the implanted ion type, chemical composition of the target

compound and the ion energy range over which the calculation has to be performed. SRIM output data (Figure 2.4) then gives the number of atomic displacements (vacancies) produced by a single particle, i.e. Ni^+ or He^+ , based on the ion energy and target material properties. By using these data, it is possible to calculate the ion fluence required to create a certain level of irradiation damage, and corresponding dpa, as [27]:

$$dpa = \frac{\phi \times 10^8 \times D}{N} \quad (2.4)$$

where ϕ is the incident ion fluence (ion/cm^2), D is the vacancy production rate ($\text{vacancy}/\text{ion}/\text{\AA}$) calculated by SRIM and N is the atomic density (atom/cm^3) of the target material.

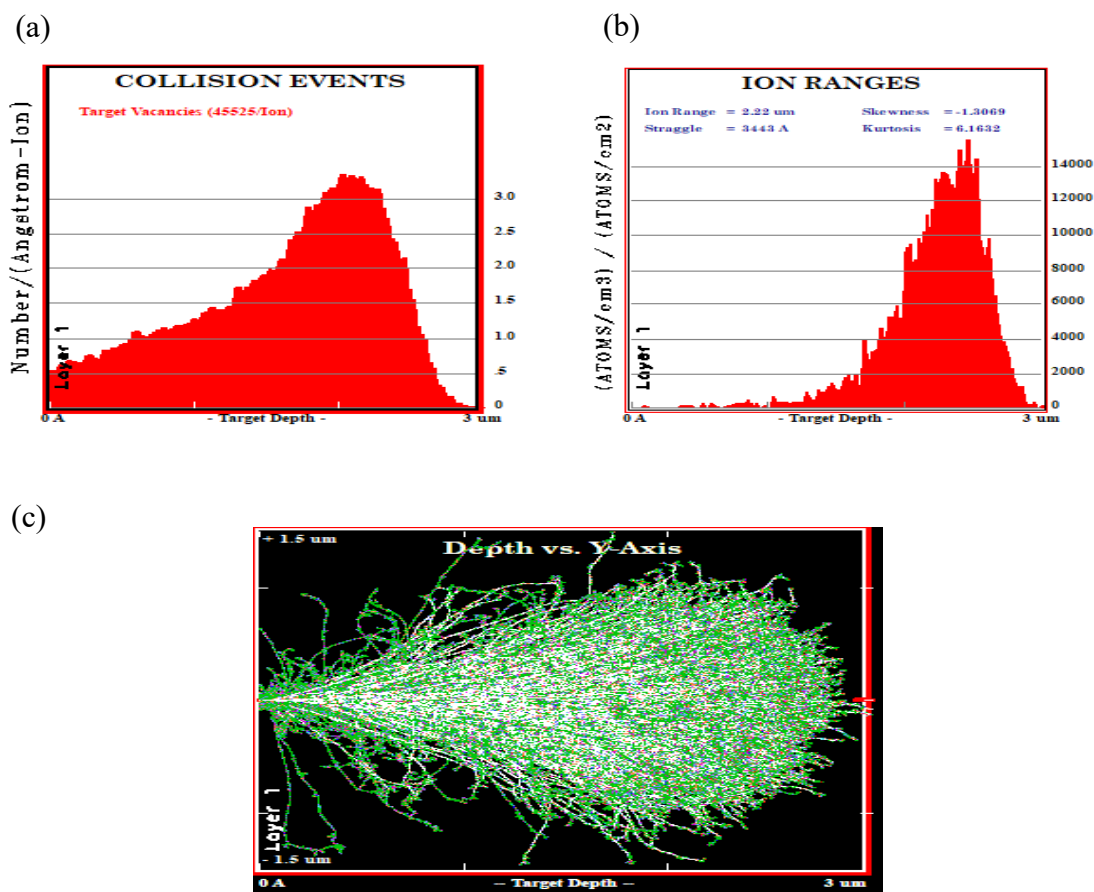


Figure 2.5: SRIM output plots illustrate: (a) damage profile of 8 MeV Ni^+ in Inconel X-750 (b) ion range in target Inconel X-750 (c) Dislocations of 8 MeV Ni ions irradiating in Inconel X-750, shows the cascade dislocations of 3000 simulated ions.

In the reactor core, radiation damage occurs primarily due to the direct displacements caused by fast neutrons resulting in collision cascades [1]. Displacement damage to Inconel X-750 however can also occur from the interaction of thermal neutrons. Thermal neutrons create damage primarily by neutron absorption causing transmutation of a nucleus and particle emission [1]. The recoil of the nucleus and to a lesser extent the emitted particles themselves then lead to displacement damage. In order to simulate and investigate radiation-induced damage, accelerated ion irradiation is an alternative to real reactor conditions. In addition, this laboratory-based irradiation allows for a controlled condition in terms of material, dose and temperature selection. However, accelerated ion implantation has been used by material scientists for decades to study radiation-induced damage formation in nuclear materials. Not only to simulate the microstructural changes created by neutrons, accelerated particles irradiation is also used to understand radiation damage fundamental processes in a controlled condition, for which neutron irradiation is difficult to approach, such as material selection, dose level control, and irradiation temperature control [13-15, 22, 28, 29]. In addition, by using a high energy heavy ion irradiation, crystallographic damages can be generated at a faster rate, about 4 orders of magnitude greater than in reactor irradiation damage. Irradiation with high energy heavy ions, producing PKA with higher energy (~5 KeV), results in the production of dense atomic displacement cascades similar to that of neutron irradiation. This allows one to create levels of irradiation damage in a test sample that is consistent with an “end of life” in reactor component after only several hours of ion implantation [30].

2.3.1 Fast neutron damage

As aforementioned, atomic displacement damage in reactor core is largely caused by direct collisions between neutrons and component atoms, occurring in several stages. In Ni, the energy of an incoming neutron required to displace the Ni atom from its lattice site is the threshold energy, which is approximately 600 eV[31]. If this minimum neutron energy is reached, the displaced Ni atom will then have a recoil energy of approximately 40 eV (enough energy to create a primary knock-on-atom (PKA). Neutron energies below 600 eV cannot displace Ni nuclei from lattice positions to create interstitial and vacancy point defects (i.e. Frenkel Pairs) [31]. If the neutron energy is above the threshold displacement

energy, the recoil energy of the PKA is transferred to nearby nuclei. The PKA is charged and thus partially slowed by electrical repulsion leading to heat. However, much of its energy is transferred by direct collision to nearby nuclei which, in turn, recoil and are displaced from their lattice positions [9]. The accumulated irradiation induced displacements are highly dependent upon the incident energies of the neutrons, which may span ten orders of magnitude in a thermal reactor: from 0.0001eV to 10 MeV [22]. The neutron irradiation is varied with the location of material components in the reactor. On average in CANDU fuel channel, each Ni atom in the spacers will be displaced approximately once per year by fast neutrons, equivalent to a total contribution of approximately 25 dpa in a CANDU spacer by end of its service life [22]. The damage is augmented with a presence of thermal neutron irradiation. However, in Ni-rich components this direct damage is supplemented by more than a factor of two due to the broad thermal neutron spectrum causing transmutations by the absorption of neutrons [23].

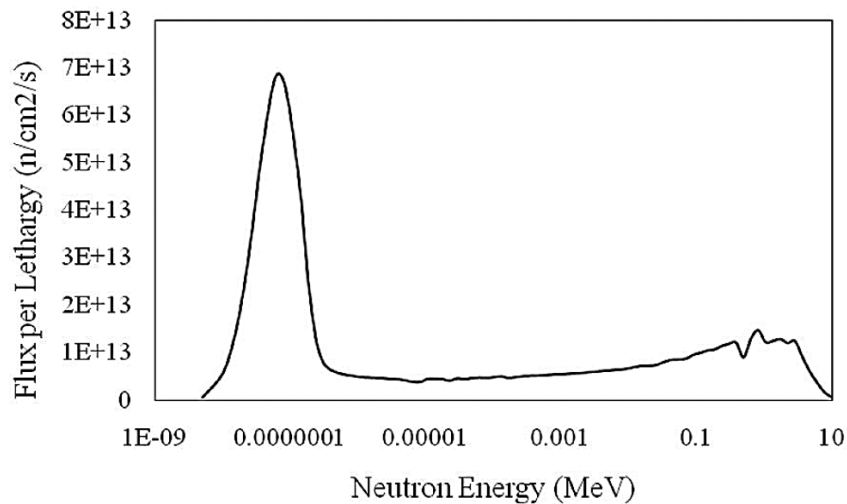
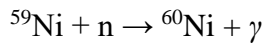
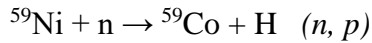
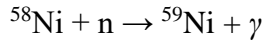


Figure 2.6: Neutron flux vs. neutron energy experienced by the Inconel X-750 spacer [22].

2.3.2 Thermal neutron damage

Comparing to fast neutron irradiation induced damages, displacements caused by thermal neutrons are usually of negligible importance. However, for components containing Ni, absorption of thermal neutrons will cause transmutation and must be noted for components

containing natural nickel such as the Inconel X-750 garter springs (which contain ~70% wt.% Ni, 68% of which is ^{58}Ni), neutron absorption at thermal energies will cause the following transmutations:



With the abundance of thermal energy neutrons in the CANDU reactor, ^{59}Ni (which does not exist in natural nickel) will be generated by thermal neutron captured by ^{58}Ni [9]. Transmutation of ^{58}Ni to ^{59}Ni occur with subsequent (n, γ) , (n, p) and (n, α) reactions as shown above. The ^{59}Ni (n, γ) , (n, p) and (n, α) reactions are very exothermic, producing both charged particles and heavy atomic recoils which lead to radiation damage. For the (n, α) reaction with ^{59}Ni the total damage energy is 176.2 keV per neutron capture and therefore the subsequent total number of displacements per neutron capture in ^{59}Ni is 1762 [32]; whereas the hydrogen and gamma reactions produce 222 and 4.9 displacements respectively [33]. The ^{59}Ni isotope produced by the ^{58}Ni (n, γ) reaction and the subsequent (n, α) , (n, p) and (n, γ) reactions make up the majority of the total dpa. Figure 2.7 shows the total and individual displacement damage per atom for both fast neutrons and (n, α) reaction.

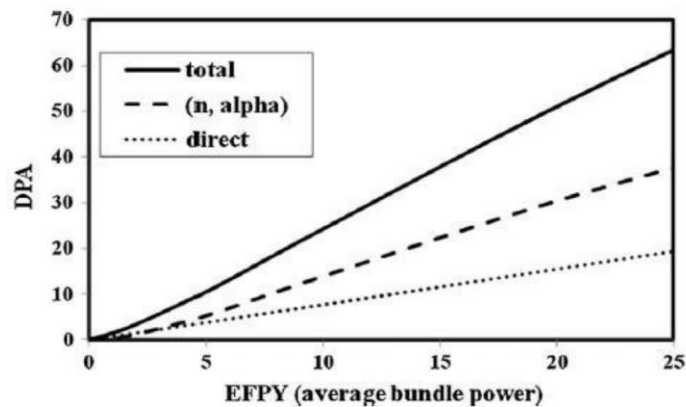


Figure 2.7: DPA calculations for an average bundle power CANDU channel [23].

2.3.3 Production of helium and hydrogen

Total dpa is not the only factor to consider when attempting to understand the effects of irradiation on the mechanical properties in the Inconel spacer material. The transmutation reaction also produces a high concentration of both hydrogen and helium in the spacer material. As previously shown, the (n, α) and (n, p) reactions generate helium and hydrogen. As helium will act to stabilize small vacancy clusters to form bubbles and/or cavities thereby accelerating the onset of void swelling which could contribute to a form of grain boundary embrittlement [9, 14, 15, 29, 32, 34]. In average, the CANDU reactor spacer will have generated approximately 20,000 appm He (2 at. %), and 5000 appm H by the end-of-life [23].

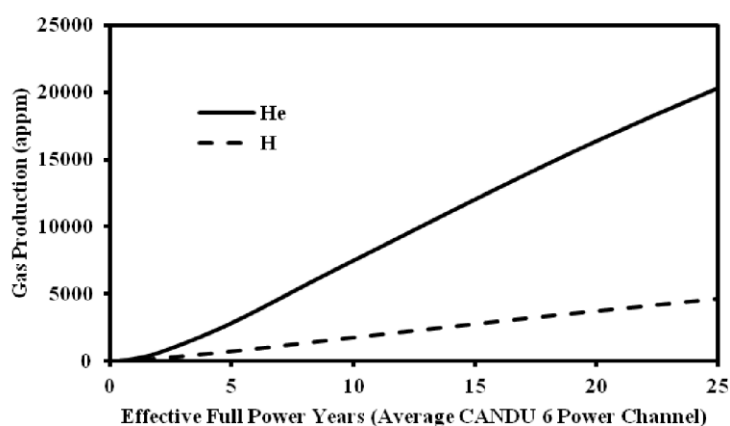


Figure 2.8: Calculated productions of helium and hydrogen in an average power CANDU channel [23].

2.4 The impact of irradiation damage on the microstructure and mechanical properties of Inconel X-750

Radiation damage can significantly alter the microstructure of materials and thus lead to drastic changes in the mechanical properties. The TEM observations on X-750 spacers removed from the CANDU reactor reveal two main microstructural damages, including introduction of the high density defects as well as inducing instability (disordering/dissolution) in the structure of strengthening phase, γ' precipitate [8, 13,

23]. The microstructural evolutions are strongly dependent upon the operation temperature which is varied at different locations of the spacer (Figure 2.3). As mentioned earlier, radiation by energetic particles can displace atoms from their lattice site through displacements cascade and produce point defects. These point defects may follow one of three regimes; either recombine with their opposite peer to annihilate, escape from cascade to become free migrating defects, or accumulate to form defect clusters. The defect agglomeration in FCC structure appear either in 3D clusters such as cavities and Stacking Fault Tetrahedra (SFT), or in planar way to form dislocation loops [35]. In Inconel X-750 components, these defects are visible at relatively low irradiation temperature $< 400\text{ }^{\circ}\text{C}$ [8, 12]. This section will review the impact of irradiation on the microstructure and mechanical properties of FCC metals, with emphasis on Ni rich alloys.

2.4.1 Irradiation hardening

Irradiation of a metal causes strengthening by source hardening and friction hardening [25]. Source hardening is the increase in stress required to start a dislocation moving on its glide plane. Source hardening due to irradiation-produced defect clusters in the vicinity of Frank–Read sources. These clusters increase the stress required to expand the loops and to permit source multiplication [25, 36]. Once the stress level is sufficient to release the source, the moving dislocations can eliminate the small clusters and reduce the stress needed to continue the deformation. Friction hardening refers to the stress required to sustain plastic deformation, which is often termed the flow stress, or friction stress [25, 37]. The forces responsible for resisting dislocation motion through a crystal lattice arise from the dislocation network and obstacles such as defect clusters, loops, precipitates, voids, etc. The friction hardening consists of long-range and short-range hardening. Long-range stresses are caused by dislocation–dislocation stress field interaction. Short-range stresses have their origin in interaction between the moving dislocation and obstacles. Therefore, the friction hardening can be described by [25]

$$\sigma_F = \sigma_{LR} + \sigma_{SR}$$

where σ_F is the friction stress and the subscripts LR and SR represent long and short-range contributions, respectively, and σ_{SR} is given by:

$$\sigma_{SR} = \sigma_{loops} + \sigma_{cavities} + \sigma_{Precipitates}$$

The degradation of mechanical properties of materials in nuclear environments is a major issue in the nuclear industry so understanding material performance and the failure mechanisms of reactor components in reactor environments is critical. Towards this purpose, it is crucial to understand the effect of irradiation induced microstructure changes on subsequent mechanical properties. Therefore, following sections explain the mechanical behavior of irradiated material by emphasizing on the effect of irradiation induced defects on the dislocation movements, cavity and helium production, and instability of γ' precipitate during deformation of Ni-based superalloys.

2.4.2 Irradiation induced defects

As was mentioned, radiation by energetic particles like heavy ions can cause atomic displacements to produce point defects (self-interstitial atoms and vacancies) in the structure of metallic materials. These point defects may then recombine to annihilate, escape from cascade to become free migrating defects, or accumulate to form clusters during cooling of the cascades. The generation and accumulation of point defects can lead to the formation of either planar defects, such as dislocation loops, or 3-dimensional agglomerations, such as voids and SFTs [8, 24]. Dislocation loops that are seen consist of Frank loops and perfect loops (Figure 2.9) [13]. Perfect loops with a Burgers vector of $1/2 \langle 101 \rangle$ were characterized as the majority of irradiation-induced dislocation loops, and Frank loops with a Burger's vector of $1/3 \langle 111 \rangle$. Both types are formed by either removing or introducing extra layer of atoms from the matrix causing an intrinsic or extrinsic stacking fault respectively. The majority observed dislocation loops in FCC metals are interstitial in type [34]. Basically, the deformation will be accommodated by the formation of dislocation cell structure at relatively lower irradiation dose; however, localized deformation in the form of defect free bands or dislocation channels is the deformation mechanism at higher doses. Yao et al. [5] systematically studied the deformation mechanism of single crystal

pure Ni irradiated with high energy proton beam. They showed that the plastic deformation during tensile test is accommodated by different mechanisms depending on the imposed radiation dose. In addition, in situ TEM observations of ion irradiated X-750 reveals that the size of the dislocation loops is mainly depend on irradiation temperature [13]. Figure 2.10-b presents the case of 12 o'clock, (300 °C -330 °C) small SFT_s (<5 nm) and large (~20 nm) dislocation loops. However, TEM observations at the location of 6 o'clock with lower operation temperature shows that the size and density of defects are quite different from the 12 o'clock with higher operation temperature. The density of defects is visibly higher than those at 12 o'clock and the size of defects are smaller, most of which are approximately 1–2 nm and no defects larger than 5 nm are observed [24]. The size distribution of defects in both 6 and 12 o'clock is plotted in Figure 2.11.

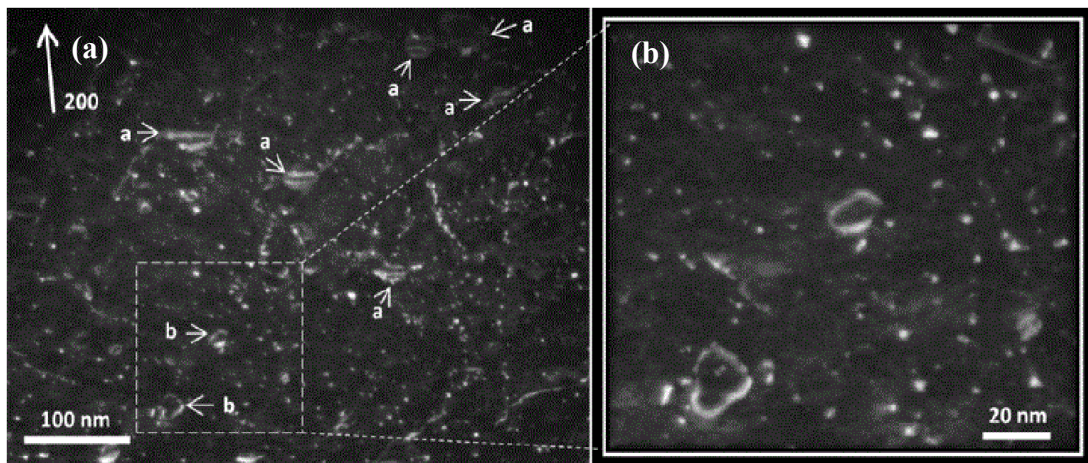


Figure 2.9: TEM image of microstructure induced by irradiation at 600 °C to 0.27 dpa. (a) $1/3\langle 111 \rangle$ type faulted Frank loops (b) $1/2\langle 110 \rangle$ perfect loops [13].

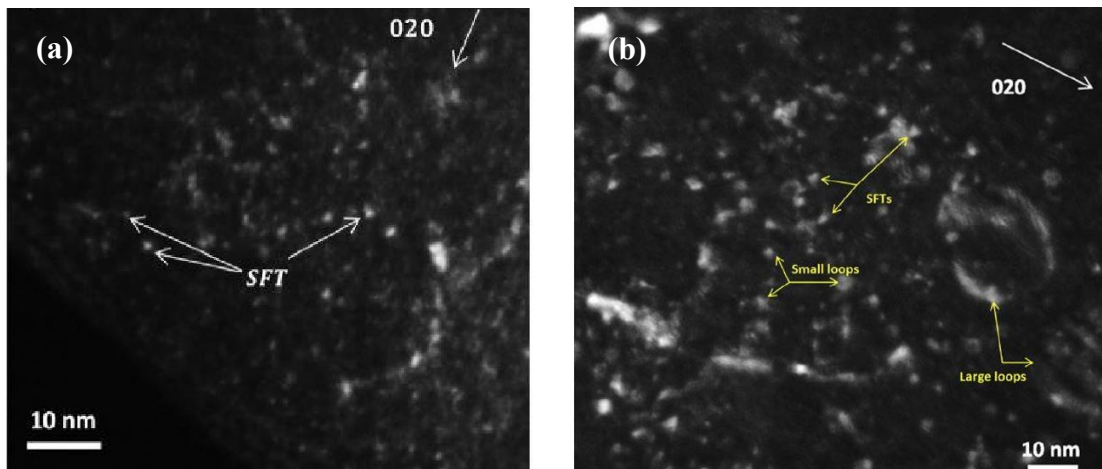


Figure 2.10: Weak beam dark field micrograph showing the evolution irradiation induced lattice defects in (a) 6 o'clock (b) in 12 o'clock location [24].

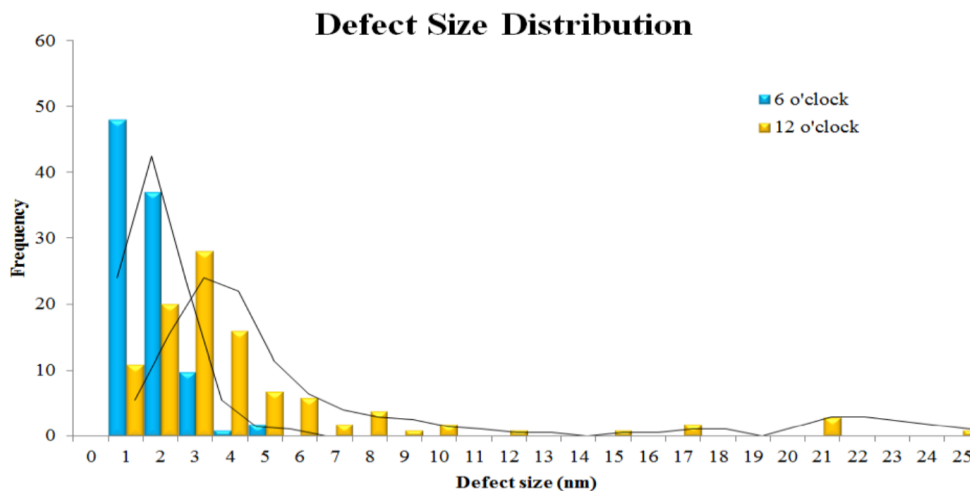


Figure 2.11: The defect size distribution in ex-service X-750 spacer at both 6 and 12 o'clock locations [24].

All loops form at lower irradiation temperatures ($< 400\text{ }^{\circ}\text{C}$) are relatively small loops (1-5 nm); while, irradiation at higher temperatures ($> 500\text{ }^{\circ}\text{C}$) leads to the development of much larger ones of both Frank and perfect loops. At a low dose, the accumulation of defects is mostly concerned with individual cascade events. At a dose greater than or equal to 0.68 dpa, a saturation of defects is reached, which was the result of damage overlapping. The defect density versus irradiation dose is plotted at Figure 2.12. It is worthwhile mentioning that the number density of defects varies as a function of irradiation dose level. Indeed,

continuous in-situ TEM observation of irradiated X-750 spacer material shows that at all irradiation temperatures the number density of defects increases rapidly in the first few steps of the irradiation [38].

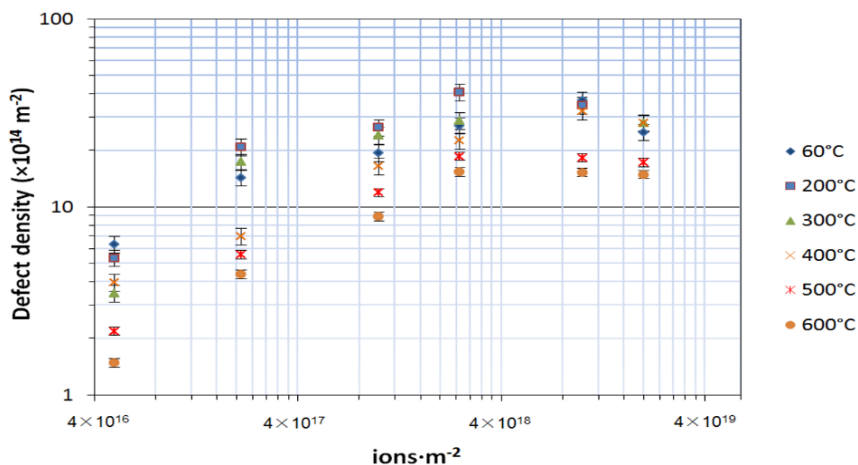


Figure 2.12: Defect density variation as a function of irradiation dose at different temperatures [13].

The mechanism of formation of the SFT_s by the displacement cascades is still not clear. The widely used model of Silcox and Hirsch [39] explains the formation of an SFT by the collapse of a triangular loop of vacancies. Silcox and Hirsch proposed SFT formation as a vacancy disc nucleates on a $\{1\ 1\ 1\}$ plane and collapses to form a loop bounded by Frank partial dislocations ($1/3\langle 111\rangle$). Each of the Frank partials to form a low energy stair-rod partial ($1/6\langle 101\rangle$) and a Shockley partial ($1/6\langle 121\rangle$) dislocation. An SFT then forms as the Shockley partials glide towards the apex of the tetrahedron formed by three intersecting $\{1\ 1\ 1\}$ planes and the original loop $\{1\ 1\ 1\}$ plane. The reaction of Shockley partials at each intersection of $\{1\ 1\ 1\}$ planes produces stair-rod partial dislocations. The resulting SFT has four triangular $\{1\ 1\ 1\}$ planes bounded by six stair-rod partial dislocations [40, 41]. Figure 2.13 shows irradiation induced SFT_s in Inconel X-750 after irradiation to 0.27 dpa at 60 °C and 400 °C. The size of SFT_s varies with changing irradiation temperature; however, it is approximately constant with irradiation dose changing.[12]. Their size is proportional to the irradiation temperature, but not to the irradiation dose, with mainly 1-2 nm at low irradiation temperature but larger size has been seen at higher temperature. This

is because the SFT_s act as sinks and absorb the free migrating vacancies and thus grow [12].

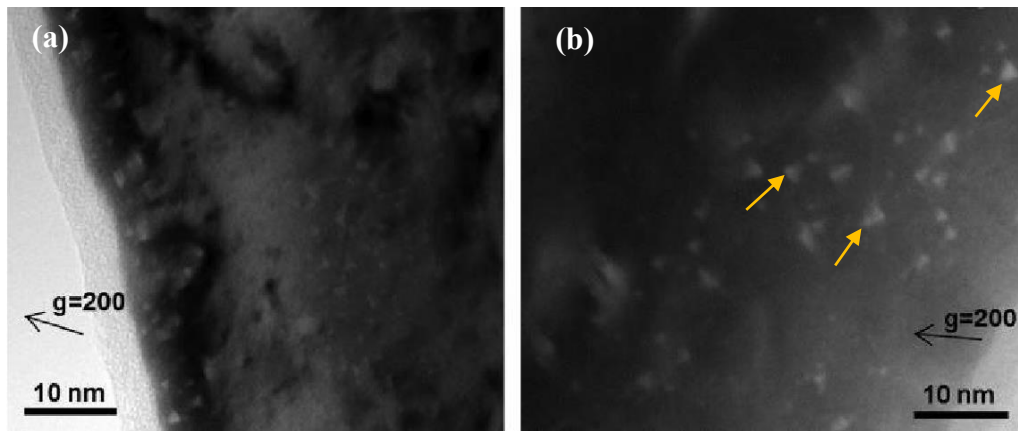


Figure 2.13: TEM micrograph close to zone axis [011] and $g = 200$ showing formation of SFT_s. (a) 0.27 dpa at 60 °C (b) 0.27 dpa at 400 °C during irradiation with 1 MeV Kr⁺² [12].

The largest contributors to radiation hardening are the high densities of radiation produced immobile defect clusters because they have strong barrier strengths and the high resistance to dislocation motion [12, 41, 42]. However, at a critical dose, the density of these defects is known to saturate and reach an equilibrium when the recombination and nucleation of these defects become even, and defect density remains stable with sustained irradiation [12, 41]. Therefore, irradiation hardening from defects such as dislocation loops and SFT_s reaches a maximum value. Transmutation reaction results in the high rate production of helium in X-750 spacer material during service in the reactor. Cavities are basically a three-dimensional clustering of vacancies. It may be empty and termed as voids or filled with gas and called bubbles. Cavities were observed in ex-service X-750 spacer as a result of high rate of helium production during transmutation reaction [8]. The size, distribution and density of the cavities are highly dependent on the operation temperature as shown in Figure 2.14 [8]. At the pinched part of the spacer, 6 o'clock (lower operation temperature) the cavities are uniformly distributed in the matrix with small size of 1-2 nm, while at the un-pinched part, 12 o'clock (higher operation temperature), larger cavity size was detected and are not distributed homogeneously; mostly segregate along the grain boundaries and precipitate interfaces [8].

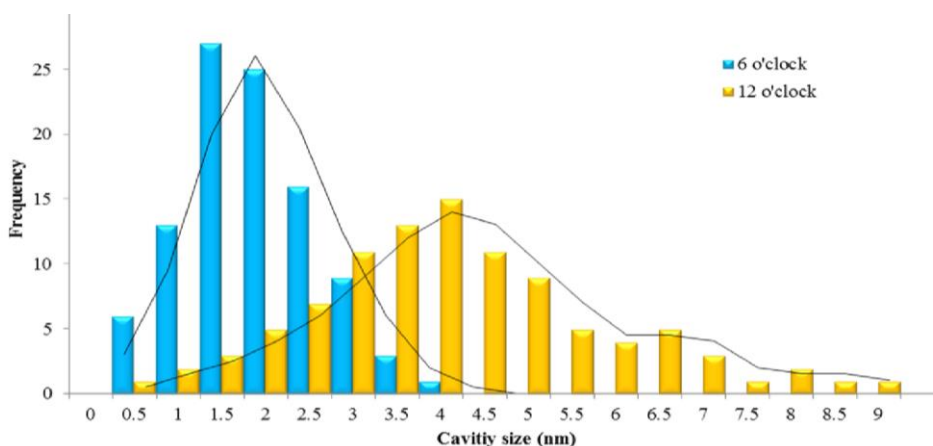


Figure 2.14: Cavity size distribution in pinched and un-pinched region in ex-service X-750 spring spacer [8].

The mutual trapping effect of helium atoms and irradiation-induced vacancies leads to the formation of cavities in the microstructure of the alloy. Figure 2.15- a shows cavities in the 12 o'clock location. However, irradiation-induced cavities in the 6 o'clock location are much smaller (~1–2 nm) than those in the 12 o'clock sample. In addition, the cavities distribution in the matrix at the lower temperature tends to be more uniform.

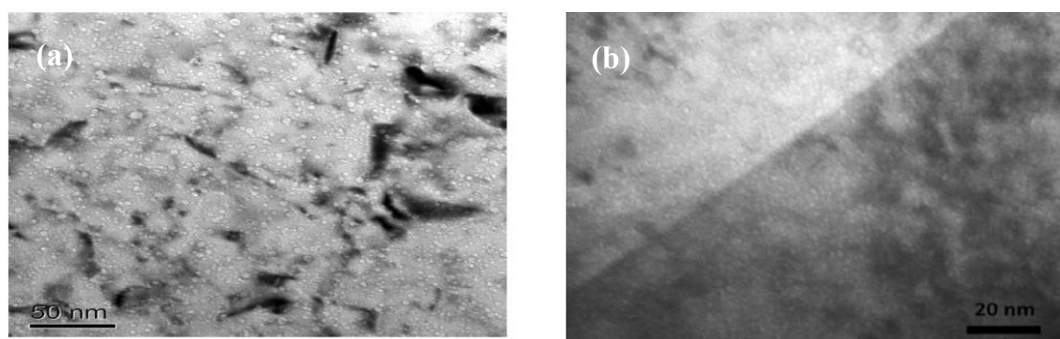


Figure 2.15: TEM bright field micrograph showing cavity evolution at (a)12 o'clock [24] (b) 6 o'clock location [22].

The absence of cavities under ion irradiation even at high temperature indicates that helium, produced from the (n, α) and (p, α) reaction during neutron and proton irradiation, respectively, is essential in nucleation of cavities in Inconel X-750. Cavity nucleation, which is basically clustering of vacancies, requires three prerequisites [43, 44]. First, the temperature should be high enough for vacancies to be mobile. Second, supersaturation of

vacancies is necessary. Third, sufficient vacancies should survive from recombination and annihilation, which requires the creation of interstitial-biased sinks such as interstitial loops. In addition to all the factors, the existence of helium atoms to trap the vacancies and stabilize them is crucial to form cavities. Cavities (void or bubbles) formation and growth is of great concern in radiation environment. Bubbles are known to cause grain boundary embrittlement [23], and void swelling which is an increase in volume and a decrease in density leads to changes in component dimensions and mechanical properties [1, 25]. Therefore, it is suggested that to better understand the cavity nucleation, growth and their effect on the material properties through energetic particle irradiation experiments, helium must be injected into the metal prior or simultaneous to energetic particle irradiation to simulate reactor environment [14, 15, 22, 29, 45]. TEM observations of irradiation of helium pre-implanted X-750 alloy show that cavity morphology depends on the amount of helium, irradiation dose, and irradiation temperature [14]. The more implanted helium, the more cavities nucleated. In other words, the given number of irradiations induced vacancies are dispersed to more nucleated cavities as shown in Figure 2.16. Helium concentration is believed to affect the size of cavities through influencing number of cavity nucleation site [42]. The more implanted helium, the more cavities nucleated [46].

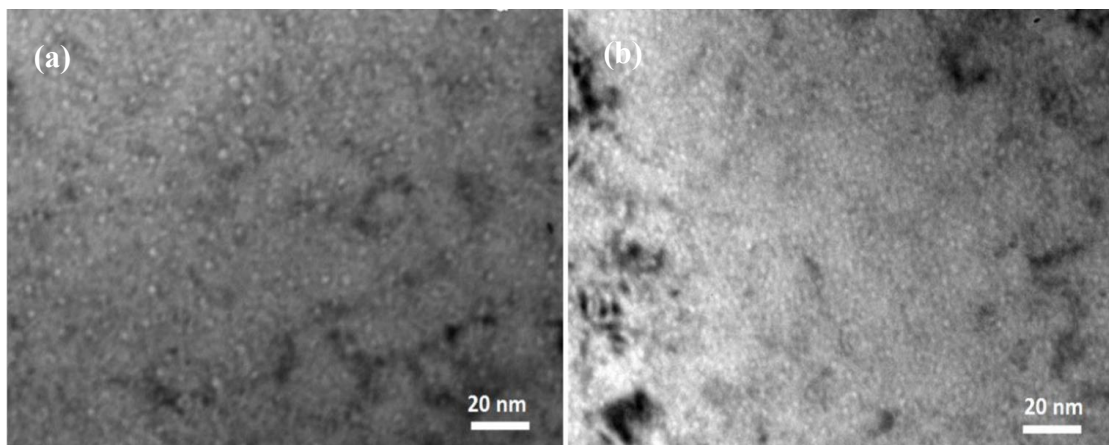


Figure 2.16: TEM micrographs showing cavity microstructures after irradiation to 5.4 dpa at 300 °C with (a) 200 appm helium (b) 5000 appm helium at room temperature [14].

In the actual CANDU reactor environment, helium is produced by transmutation at the service temperature of 200 °C ~ 330 °C [22]. At these temperatures, helium is mobile and can easily migrate [47]. However, in contrast to neutron irradiated Inconel X-750, sink of cavities to grain boundaries and phase boundaries were not found during heavy ion irradiation with cold pre-injected helium, in a wide irradiation temperature range from 60°C to 500°C. The absence of cavity segregation to boundaries during heavy ion irradiation with cold pre-injected helium might be caused by the mutual trapping effect between helium atoms and vacancies [15]. Helium was immobile in the material while being injected at room temperature as helium atoms may have already been trapped in vacancies to form cavity embryos [14]. Once this has occurred, the migration of helium was limited. Consequently, fewer helium atoms migrated to the boundaries to assist the cavity nucleation.

In contrast to previous heavy ion irradiations with cold pre-injected helium (room temperature) , in high temperature injected helium heterogeneous nucleation of cavities was observed. Cavity distribution was found to be consistent with in-reactor neutron irradiation induced cavity microstructures. This implies that diffusion of helium is greatly dependent on the injection temperature, and helium pre-injection at high temperature is preferred for simulating the migration of the transmutation produced helium [15]. As shown in (Figure 2.17-a) , cavities were observed within grains after helium pre-injections at 400 °C. After 400 appm helium heterogeneously distributed low density cavities ($2.27 \times 10^{22} \text{ m}^{-3}$) (arrowed) with sizes smaller than ~1 nm was observed. After 1000 appm helium implantation (Figure 2.17-b), a substantially higher density ($5.79 \times 10^{23} \text{ m}^{-3}$) of cavities with sizes of 1~2 nm was noted. Line dislocations tended to be the preferred nucleation sites for cavities. The size of cavities at dislocations was slightly larger than those in the matrix. In sample implanted with 5000 appm helium (Figure 2.17-c), highly dense ($8.52 \times 10^{23} \text{ m}^{-3}$) and uniformly distributed cavities with sizes of ~ 2 nm present.

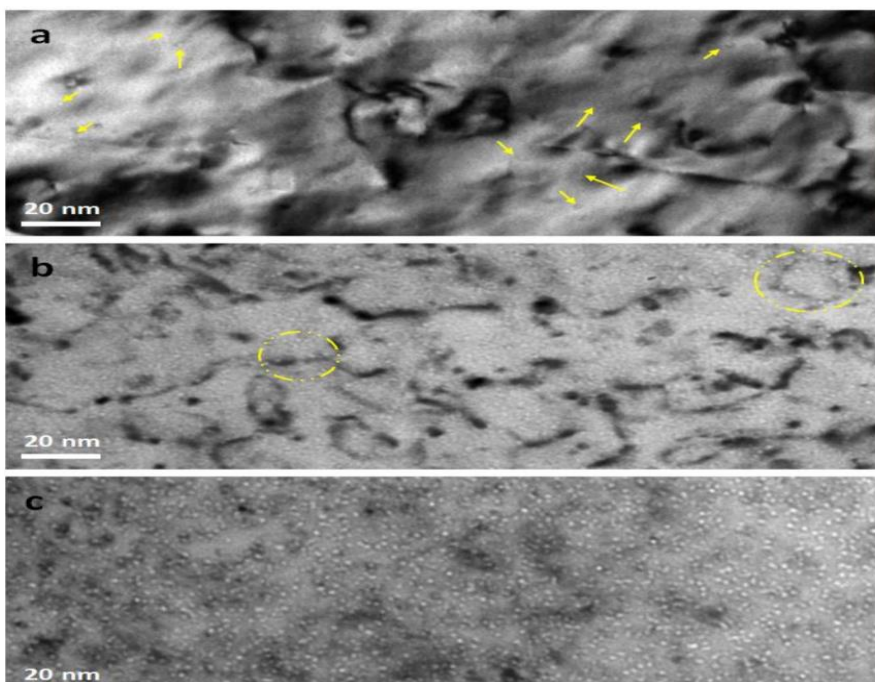


Figure 2.17: Under focus bright field micrographs showing cavity formation after helium implantation at 400 °C (a) 400 appm (b) 1000 appm (c) 5000 appm [15].

Cavity mean size and density against helium dosage are shown in Figure 2.18, where an obvious increase of size and density with the increasing helium dosage can be observed.

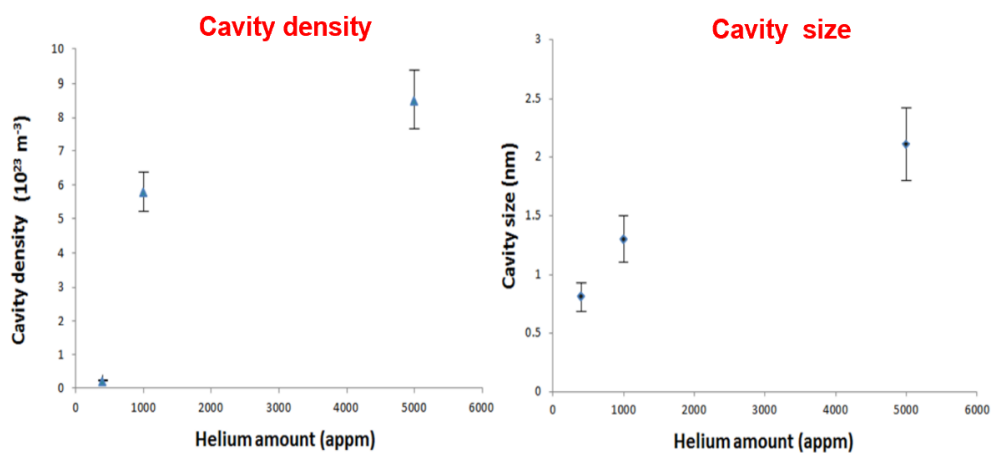


Figure 2.18: Cavity density and cavity size, against amount of injected helium [15].

This implies helium pre-injection at an elevated temperature followed by heavy ion irradiation is likely more practical for simulating the real situation of helium diffusion in the reactor environment. Increasing irradiation temperature can lead to increase in vacancy diffusion rate which enhances the cavity growth. In addition, higher irradiation temperature results in lower density of cavity due to the decrease of vacancy supersaturation [13]. So, as a result, it is also found that helium implantation at room temperature and high temperature results in cavity formation in grain boundary and grain interior in Ni and Ni superalloy [15, 48].

The way that the cavities affect the mechanical behavior depends on how they interact with dislocation motion. Nanometer-size bubbles are at first considered to be shearable obstacles through which dislocations can pass easily. However, it has been found later on that voids and gas filled bubbles will retard dislocation motion in metals, leading to an increase in strength [49, 50]. It has been suggested that matrix hardening associated with bubbles can be estimated using a standard dispersed barrier model originally proposed by Orowan as the bubbles will pin the dislocation motion much like precipitates [51].

Knapp et al [48] on the hardening effect of helium bubbles in pure Ni. They found that helium bubble strengthening effect depends on helium concentration, bubble density, and bubble size. In this study, Ni was implanted with helium up to 10 at. % at different temperatures to have different size and density of bubbles. Subsequent nanoindentation testing indicated that the hardness of implanted sample was 7 times higher than the unimplanted samples on the hardening effect of helium bubbles in pure Ni. They found that helium bubble strengthening effect depends on helium concentration, bubble density, and bubble size and that different temperatures produce different size and density of bubbles. Figure 2.19 shows the measured strengths for all the samples plotted against helium concentration.

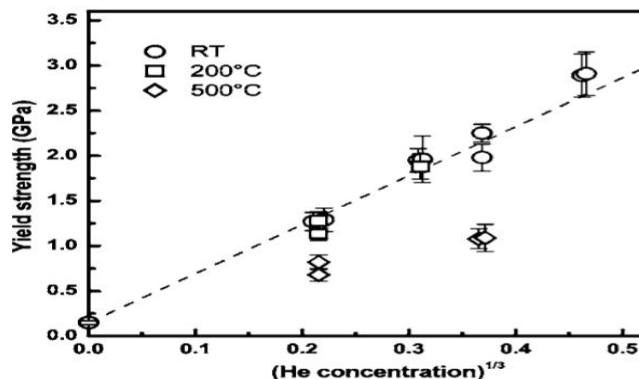


Figure 2.19: The yield strength of Ni implanted with helium at the indicated temperatures plotted versus the cube root of helium concentration [48].

2.4.3 Instability of gamma prime (γ') precipitate

Coherent secondary precipitates such as γ' make super-alloys such as Inconel X-750 very strong and resistant to creep at elevated temperatures [20]. The same mechanisms that lead to irradiation hardening in some alloys can also affect the stability of the, γ' precipitates, leading to loss of strength following irradiation [52]. During irradiation, it is believed that two mechanisms operate, including ballistic mixing arising from irradiation to disorder the precipitates and the thermal recovery results in dynamic reordering [51, 53, 54]. The ballistic mixing from collision cascade predominates at low temperatures where the rate of thermal recovery is low, and the ordered phase can be easily disordered. Conversely, upon increasing the irradiation temperature above a critical point where the competition between cascade displacement and thermal recovery reaches a balance, the aging effect would overwhelm, and the γ' precipitates will remain stable. The critical temperature can be varied with respect to the chemical composition of materials and irradiation dose rate [38, 51].

The contribution of the γ' phase to the strength of the alloy, which is referred to as precipitation strengthening, involves both interfacial strengthening and ordered strengthening [31]. The ordered strengthening, which originates from the formation of antiphase boundaries (APB_s) in the ordered, γ' phase, plays a dominant role in the strengthening. Dislocation movement during deformation within the ordered γ' phase with the L1₂ structure is different from what happens in typical FCC structures. The work of

Yamaguchi et al. [55] and Paidar et al.[56] showed that the $[10\bar{1}]$ superdislocation dissociates into two $\frac{1}{2} [10\bar{1}]$ superpartials. In this case, the two superpartials $\frac{1}{2} [10\bar{1}]$ are separated by an APB. The dissociation primarily occurs on $[5\bar{7}]$ planes and the APB is also on $\{111\}$ planes; however, after cross slip of superpartials dislocations, the APB tends to lie on the $(0\ 1\ 0)$ plane because it has minimal energy on this plane. Therefore, the superpartials core is not confined to the plane determined by the APB and thus the dislocation is sessile with respect to glide on $(0\ 1\ 0)$.

The contribution of an ordering strengthening mechanism to the deformation behavior of superalloys strongly depends on the degree of order of the γ' precipitates. The disordering of $L1_2$ -ordered γ' precipitates at a very low dose of irradiation (0.06 dpa) is one of the important changes during heavy ion irradiation [24]. However, it was found that there is a critical temperature for disordering process and the γ' phase stays ordered under irradiation at higher temperature than critical temperature [24]. In a recent systematic TEM study performed by Zhang et al [24] on X-750 the alloy was irradiated with Kr^{2+} ions at a dose rate of 10^{-3} dpa/sec up to a maximum dose of 5.4 dpa at a range of irradiation temperatures 60 °C - 400 °C and then a following investigation at 500 °C and 600 °C. The dose related change in γ' disordering was followed by imaging its superlattice diffraction patterns at several doses and irradiation temperatures. These results showed that at temperatures below 400 °C, γ' precipitates become disordered at a low dose (0.06 dpa), while it remains stable up to 5.4 dpa at higher irradiation temperature as shown in Figure 2.20. However, a trend toward the dissolution of γ' was indicated.

(a)

		Temperature K (°C)					
		333 (60)	473 (200)	573 (300)	673 (400)	773 (500)	873 (600)
Dose (dpa)	0	*	*	*	*	*	*
	0.015	*	*	*	*	*	*
	0.06	o	o	o	o	*	*
	0.27	o	o	o	o	*	*
	0.68	o	o	o	o	*	*
	2.70	o	o	o	o	*	*
	5.40	o	o	o	o	*	*

• Indicates the superlattice reflections observed; o indicates no superlattice reflection observed; γ' were disordered at dose <0.06 dpa when the material was irradiated at temperature 333 K to 673 K (60 °C to 400 °C), but they stayed ordered at ≥ 773 K (500 °C).

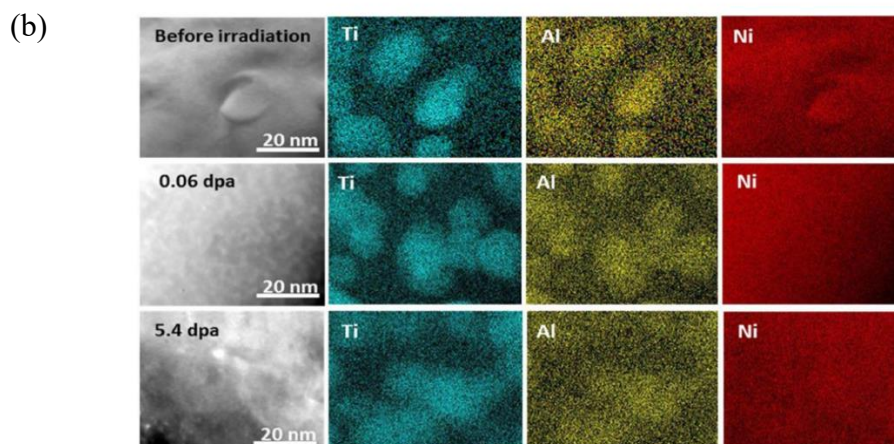


Figure 2.20 (a) Disordering kinetics of γ' (b) Post-irradiation ChemiSTEM mapping of γ' precipitates after irradiation at 300 °C up to 0.06 and 5.4 dpa [24].

In addition, Nelson et al. [58] systematically studied the stability of Ni_3Al , γ' precipitates in Nimonic PE16 (Fe-rich FeCr-Ni-based alloy with Al and Ti additions) and Ni-Al model alloys. They observed that during heavy ion bombardment at room temperature, γ' precipitate became disordered at about 0.1 dpa in both aged Ni-Al alloys and PE16. Camus et al. [38] showed that at a dose rate of 10^{-3} dpa/s and at temperatures below approximately 270 °C, that the γ' precipitates will be disordered first and dissolved later. The impact of γ' disordering or dissolution on mechanical properties of irradiated X-750 alloy has not been studied yet. But it is extensively investigated in Inconel 718 which is precipitation hardened with both γ' and γ'' . The results show that the irradiation led to softening of material instead of hardening indicating the contribution of secondary phases to mechanical properties overwhelms that of irradiation induced defects like loops or cavities. Carsughi et al. [52] studied the effect of proton irradiation on mechanical properties of Inconel 718. Figure 2.21 presents the hardness values versus irradiation doses indicating a decrease in hardness with increasing irradiation dose. Complementary work by Hashimoto et al. [59] investigated the effect of 3.5 MeV Fe^+ , 370 keV He^+ and 180 keV H^+ either single or simultaneous irradiation on Inconel 718 hardness behavior. The obtained results are indicated in Figure 2.22, showing the softening behavior of post-irradiation hardness tests with increasing dose. By TEM examination it is revealed that in the Fe-irradiated sample, the γ' and γ'' superlattice diffraction spots vanished at 1 dpa, indicating the cause of

softening is the loss of coherency of the γ' and γ'' precipitates. Even though the Fe-ion irradiation also introduced radiation defects, the loss of the precipitates outweighed the hardening contribution from these defects.

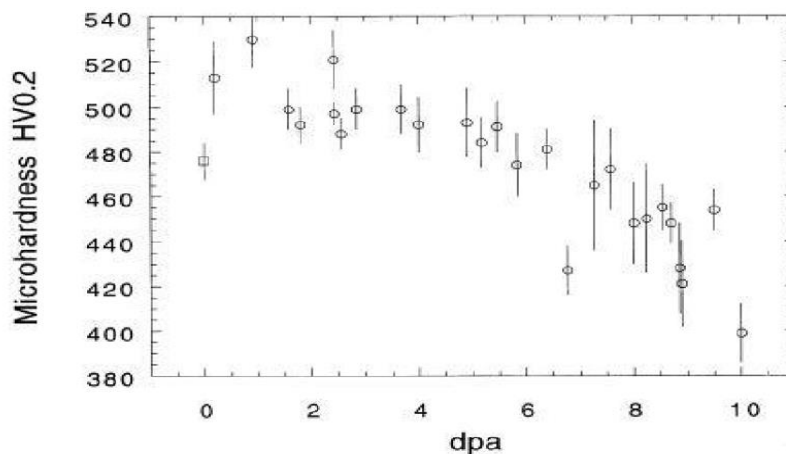


Figure 2.21: Microhardness of irradiated Inconel 718 as a function of irradiation dose [52].

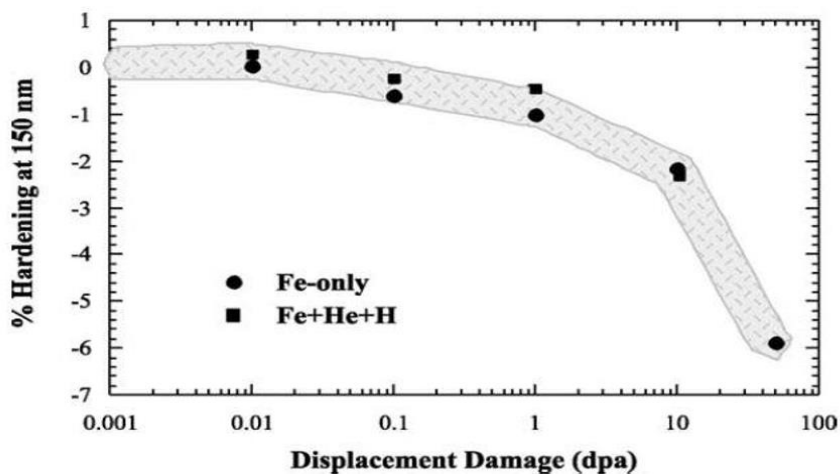


Figure 2.22: Percent change in hardness at 150 nm contact depth, relative to the unirradiated material, for Inconel 718 as a function of Fe-only and from triple-beam irradiation [59].

2.5 Pyramidal indentation testing

2.5.1 Nano hardness testing

Nano-indentation testing is a fairly mature technique which uses the recorded depth of penetration of an indenter into the specimen along with the measured applied load to determine the area of contact and hence the hardness of the test specimen. Many other mechanical properties can also be obtained from the experimental load–displacement curve, the most straight-forward being the elastic modulus. [60]. Nanoindentation has been proven to accurately profile ion irradiated zones of material and the transition interface between irradiated and nonirradiated material, where injected interstitials sit, is in good agreement with SRIM software [61]. Several examples have reported the potential of this technique for testing ion irradiated materials [2, 28, 29, 60].

2.5.2 Basic fundamentals

The three-sided Berkovich indenter is the most popular geometry for nano-indentation testing. A typical Berkovich indenter tip is shown in Figure 2.23. A schematic representation of a typical data set obtained with a Berkovich indenter is presented in Figure 2.24, where the parameter P designates the load and h is the displacement relative to the initial un-deformed surface.

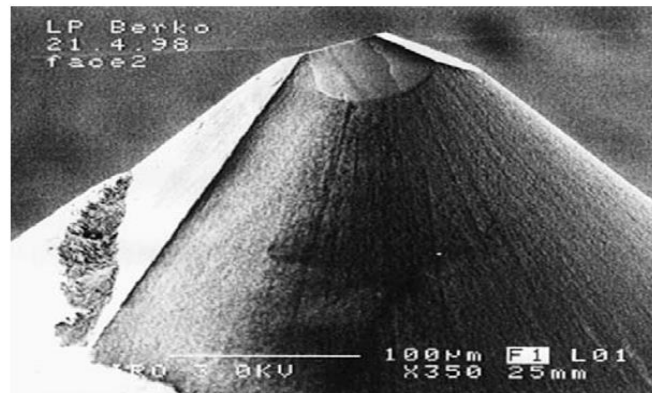


Figure 2.23: High-magnification SEM scan of the tip of a Berkovich diamond indenter [62].

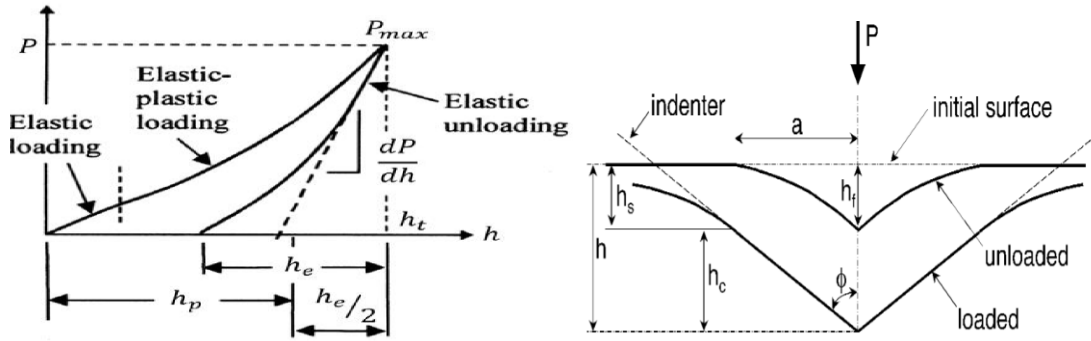


Figure 2.24: (a) Schematic illustration of indentation load–displacement curve [63] and (b) unloading process showing parameters characterizing the contact geometry [64] .

In Figure 2.24 there are three important quantities that must be measured from the P – h curves: the maximum load, P_{max} the total displacement h_t , and the elastic unloading stiffness, $S = dp/dh$, defined as the slope of the upper portion of the unloading curve during the initial stages of unloading (also called the contact stiffness). Finally, another important parameter is the plastic depth, h_p , the permanent depth of penetration after the indenter is fully unloaded. The exact procedure used to measure H and E is based on the unloading processes, in which it is assumed that the behavior of the Berkovich indenter can be modeled by a conical indenter with a half-included angle, ϕ , that gives the same depth-to-area relationship, $\phi = 70.3^\circ$.

The test ends by reducing the indentation force allowing the sample to elastically push the indenter, this distance is the elastic indentation depth, h_e . These tests usually include partial unloading during the indentation cycle. Through testing of the force-depth data at an unloading, the plastic depth, h_p , has been approximated as:

$$h_p = h_t - \frac{h_e}{2} \quad (2.5)$$

where h_e is the elastic depth and h_t is the total depth as illustrated in Figure 2.24 [63]. Assuming that pile-up is negligible, the elastic models show that the amount of sink-in, h_s , is given by [65]:

$$h_s = \varepsilon \frac{P_{Max}}{S} \quad (2.6)$$

where ε is a constant that depends on the geometry of the indenter which is $\varepsilon = 0.72$ for a conical indenter, $\varepsilon = 0.75$ for a paraboloid of revolution (which approximates to sphere at small depths), and $\varepsilon = 1.00$ for flat punch [65]. As a result, the maximum displacement, h_{max} can be divided into the contact depth, h_c , and the displacement of the sample surface at the perimeter of contact, h_s :

$$h_{max} = h_c + h_s \quad (2.7)$$

The three-sided pyramidal Berkovich indenter tip makes a sharper point than the four-sided Vickers microhardness punch allowing for more precise shallow nano indents. The area function also sometimes called the projected (cross section) area of the indenter at a specific distance back from its tip and must carefully be calibrated by independent measurements so that deviations from non-ideal indenter geometry are considered. The area, A_p , of the indentation, projected normal to the indentation direction, can be calculated from h_p , which for a perfect three-sided pyramidal “Berkovich” indenter, is given as:

$$A_p = \pi \cdot \tan^2 \alpha \cdot h_p^2 \cong 24.5 h_p^2 \quad (2.8)$$

where $\alpha = 70.3^\circ$ and represent the effective semi-angle of the conical indenter equivalent to the Berkovich [63]. The area function of an actual indenter will be affected by a certain amount of indenter tip rounding causing A_p to typically be expressed by a higher order function of h_p . In this case $A_p(h_p)$ is determined experimentally by performing indentations on a standard of well-known hardness, such as quartz or sapphire. The area function in conjunction with the force allows the indentation hardness, H , to be calculated as:

$$H = \frac{P}{A_p(h_p)} \cong \frac{P}{24.5 h_p^2} \quad (2.9)$$

During micro-indentation hardness studies, it is important to realize that the volume of the sample that is plastically deforming, and hence contributing to the calculated hardness value, extends significantly deeper than the actual indentation. This makes it critical to be able to determine the actual depth of the plastic zone beneath the indenter. K. L. Johnson [63] analyzed the size of the plastic zone beneath an axisymmetric conical indentation made in an isotropic non-hardening material and determined that the plastic zone radius, c , was related to the indentation width, a , as:

$$\frac{c}{a} = \left[\frac{E_r \tan \alpha}{6\sigma_y(1-\nu)} + \frac{2}{3} \left(\frac{1-2\nu}{1-\nu} \right) \right]^{\frac{1}{3}} \quad (2.10)$$

where ν is the Poisson's ratio, σ_y is the yield stress, α is the apex angle of the indenter [64], and E_r is the reduced elastic modulus which is introduced because the indenter is not a perfectly rigid body. Because the indenter is not a perfectly rigid body, this is accounted for by introducing a reduced modulus E_r , which is a superposition of the moduli of the indenter and indented material. Therefore, E_r is the combination of the elastic moduli of the indenter head and the indented sample and is determined by [62, 63]:

$$\frac{1}{E_r} = \frac{(1-\nu^2)}{E} + \frac{(1-\nu'^2)}{E'} \quad (2.11)$$

where ν' and E' , and ν and E represent the Poisson's ratio and elastic modulus of the indenter and the sample respectively. Considerable study has been made upon the relationship between H and the yield stress, σ_y , of the indented material. Tabor reported that the hardness of the majority of common metals was approximately $3\sigma_y$ and subsequent more detailed studies of specific alloy systems have shown that this relationship holds surprisingly well for the vast majority of ductile metals [66, 67].

As mentioned earlier, Nano-indentation test is essential to test ion-irradiated samples, since the high-energy ions only penetrate a few micrometers into the test material.

2.5.3 Indentation stress

The stress under an indentation varies from high levels in the vicinity of the tip to vanishingly small values in remote regions. Moreover, the stress state is highly multiaxial in nature and its degree of tri-axially varies with position. However, a characteristic (or effective) indentation stress is commonly expressed. This characteristic indentation stress σ_{ind} is taken as the applied load P , divided by the indentation contact area A_{ind} . For a Berkovich indenter:

$$A_{ind} = 3\sqrt{3}h^2 \tan^2\theta \quad (2.12)$$

where h is the depth of indent and $\theta = 65.3^\circ$ is half of the included angle of the indenter. Therefore, one can write the indentation stress as σ_{ind} :

$$\sigma_{ind} = \frac{P}{cA_{ind}} = \frac{P}{24.5Ch^2} \quad (2.13)$$

where c is the correction factor when considering pile-up and/or sink-in.

At a particular depth of penetration, the indentation contact area is dependent not only upon the indenter tip shape, but also the elastic properties of the indented material. Materials with limited elasticity accommodate the volume of the indenter by plastic flow of the material, eventually causing the indented material to pile-up around the indenter tip. Elastic materials accommodate the indenter by longer range elastic deformation. In such cases the material appears to sink-in around the tip. Sink-in is often associated with well annealed samples, Figure 2.25 is a schematic of these two situations shown in cross section and top view. These figures demonstrate that the extent of elastic deformation can dramatically change the contact area from that predicted by the total displacement of the probe. Bolshakov and Pharr [68] did extensive finite element analysis on the influence of material properties on the shape of the deformation zone during indentation testing. They suggested that the ratio of the final indentation depth to the maximum indentation depth

$\left(\frac{h_f}{h_{max}}\right)$ can be used to assess pile-up/sink-in phenomena in the indentation testing. It was suggested that in work-hardened samples $\frac{h_f}{h_{max}} \geq 0.7$ results in pile-up and $\frac{h_f}{h_{max}} \leq 0.7$ yields sink-in behavior [69]. If indenter geometry is self-similar at all depths, C should be independent of depth for a homogeneous material [70]. The amount of pile-up corresponds to the size of the plastic zone, or the load applied. A parameter describing the ratio of the indentation contact area to the triangular area was then determined for each set of indentations:

$$c = \frac{A_i}{A_c} \quad (2.14)$$

where A_i refers to the actual indentation projected contact area, and A_c to the ideal cross-sectional area of the indenter. For an indentation where pile-up has occurred, $c < 1$; for sink-in $c > 1$ [70]. If indenter geometry is self-similar at all depths, c should be independent of depth for a homogeneous material [70]. Figure 2.25 shows a plot of c as a function of depth for the strain-hardened and the annealed copper samples.

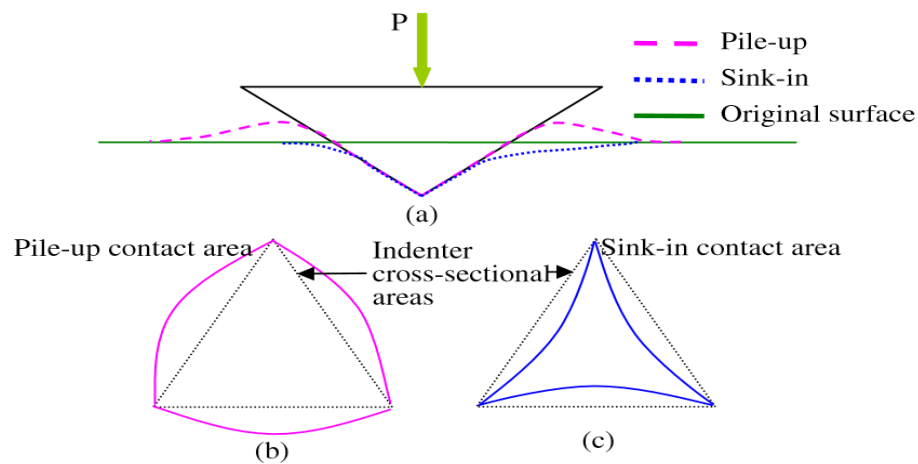


Figure 2.25: Schematic representation of pile-up and sink-in [71].

2.5.4 Indentation strain rate

Following the argument described in the previous section for the effective indentation stress, Atkins et al. [67] derived a relationship for the effective average indentation shear strain rate $\dot{\gamma}_{ind}$, as a function of the distance r from the center of an indentation, the diameter of the hydrostatic volume of deformed material beneath the indentation d , and the rate of change of this diameter with respect to time \dot{d} :

$$\dot{\gamma}_{ind} = \frac{3}{2} \frac{d^2}{r^3} \dot{d} \quad (2.15)$$

This relationship was used by Pollock et al.[72], who selected the maximum strain rate (located at the boundary between the hydrostatic volume and the region deforming plastically) as the characteristic value of the indentation strain rate. In addition, they noted that, for a conical indenter, the value of d and the indentation depth h are linearly related, leading to the following equation:

$$\dot{\epsilon} = k \frac{\dot{h}}{h} \quad (2.16)$$

Where k is constant.

2.6 Indentation strain rate and stress

There are four types of tests that have been employed using depth-sensing indentation systems to gain insight into the relationship between indentation strain rate and indentation stress [73]: indentation load relaxation (ILR) tests [74] constant load rate (CLR) tests [75] constant-load indentation creep tests and constant strain rate (CSR) tests [76]. In the following section CLR test mechanism is discussed.

2.6.1 Constant load rate tests (CLR)

In a CLR test, the indenter is loaded at a constant loading rate until the indenter has reached a prescribed depth in the material. A complete series of experiments would involve this procedure utilizing a different loading rate for each indent made and calculating the indentation stress for that loading rate from the applied load and the achieved depth. Researchers [76-80] have used CLR indentation testing, at a wide range of loading rates and indentation depths, in order to measure the rate sensitivity of materials. Indentation is, indeed, a preferable method, since the tested volume of material is scale-able with respect to the microstructure, to measure the strain rate sensitivity of metals and alloys.

By taking the indentation stress σ_{ind} and indentation strain rate $\dot{\epsilon}_{ind}$ proportional to flow stress and flow strain rate, one can write:

$$\sigma_{ind} = D \dot{\epsilon}_{ind}^m \quad (2.17)$$

Where D is a temperature dependent constant and by taking logarithm of both sides of Eq. 2.17 and simply yields:

$$m = \frac{d \ln \sigma_{ind}}{d \ln \dot{\epsilon}_{ind}} \quad (2.18)$$

2.7 Indentation size effect (ISE)

Scale-dependent behavior is observed in indentation testing when the size of the hardness impression is small, resulting in an indentation size effect. In nano-indentation size effect the hardness values increase at small depths, giving rise to the expression “smaller is stronger”. Figure 2.26 presents the typical ISE for cold worked and single crystal copper.

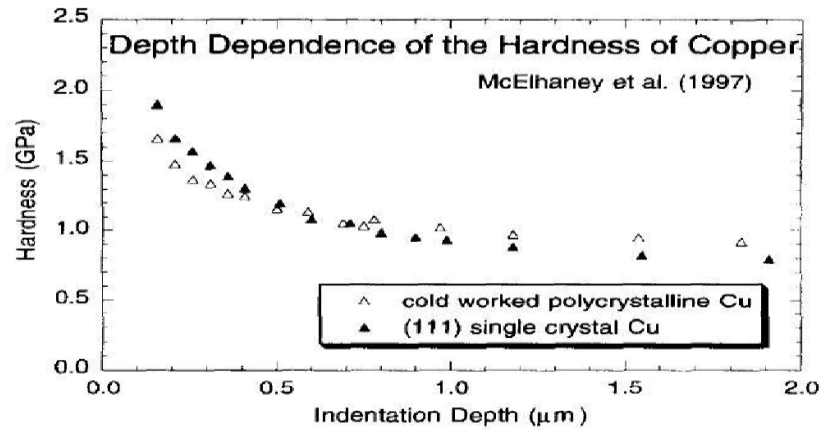


Figure 2.26: Hardness variation as a function of indentation depth, showing the ISE in Cu [81].

In order to characterize and explain the ISE, many of research activities have tried to model the phenomenon. Modeling efforts can be categorized roughly into two types, depending on whether the model is mechanistically based [82, 83], relying on dislocation descriptions of the hardening mechanisms, or phenomenological, introducing material length-scale parameters into conventional descriptions of continuum plasticity [84]. Because the latter often invokes the concept of a plastic strain gradient, such approaches are commonly referred to as strain gradient plasticity models. Size effects in the indentation hardness may arise from either the strong gradients of plastic strain that are naturally created in micrometer scale indentations or from dislocation starvation effects for nanometer scale indentations [85] that may arise when intense plastic deformation is forced to occur across a very small volume of an initially defect-free crystalline material. This is clearly evident during nano/micro-indentation tests when the measured indentation stress σ_{ind} is clearly greater at small indentation depths. It is well documented that an indentation size effect (ISE) exists where the measured hardness increases with decreasing indentation depth. Nix and Gao have modelled the ISE based on the volumetric density of geometrically necessary dislocations (GND) contained within the hemispherical plastic zone beneath the visible indent [81]. The model is based on the concept of geometrically necessary dislocations (GND_s), that is, dislocations that must be present near the indentation to accommodate the volume of material displaced by the indenter at the surface. In the Nix-Gao model, the

indenter is assumed to be a rigid cone whose self-similar geometry is defined by the angle, θ , between the indenter and the undeformed surface (Figure 2.27).

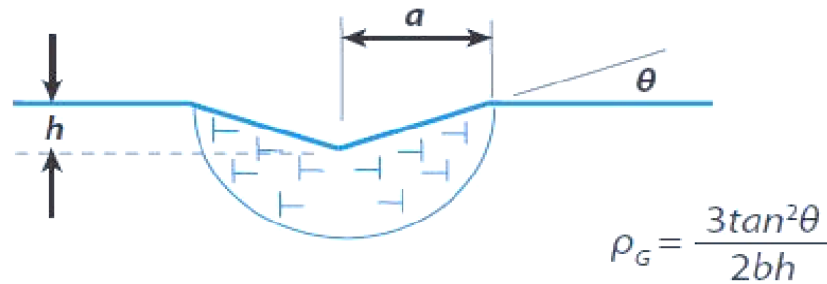


Figure 2.27: Schematic representation of the Nix-Gao model for conical indenters [86].

The basic principle underlying the model is that the GND_s exist in addition to the usual statistically stored dislocations (SSD_s) produced during uniform straining, giving rise to an extra hardening component that becomes larger as the contact impression decreases in size.

In addition, two key assumptions are made: 1) the total dislocation density is simple mathematical sum of the geometrically necessary part, ρ_{GND} , and the statistically stored part, ρ_{SSD} , that is, $\rho_t = \rho_{GND} + \rho_{SSD}$ and 2) the GND_s are constrained to reside within a hemispherical volume (Figure. 2.25), where the radius of the volume is equal to the radius of contact of the indenter in the surface (a). Simple geometric considerations then lead to:

$$\rho_{GND} = \frac{3 \tan^2 \theta}{2bh} \quad (2.19)$$

This is a very important relation, as it contains the essential physics of the ISE; namely, the hardness increases at small depths because the geometrically necessary component of the dislocation density is inversely proportional to the depth and rises dramatically and without bound when the contact is small. Combining the above relations leads to famous Nix-Gao model for ISE:

$$H^2 = H_o^2 \left(1 + \frac{h^*}{h}\right) \quad (2.20)$$

In which H_o represent the macroscopic hardness

$$H_o = 3\sqrt{3}\alpha\mu b\sqrt{\rho_{SSD}} \quad (2.21)$$

And h^* represents characteristic depth below which the extra hardening becomes appreciable and depends on both material parameters, ρ_{SSD} and geometric parameters (θ) and is thus not strictly a material constant.

$$h^* = \frac{(3\tan^2\theta)}{(2b\rho_{SSD})} \quad (2.22)$$

For statistically stored dislocations we have:

$$\rho_{SSD} = \frac{H_o^2}{27(\alpha\mu b)^2} \quad (2.23)$$

Figure 2.28 shows the plots of H^2 vs. $1/h$ for the Cu data of McElhaney et al.[84] and the Ag data of Ma and Clarke [87], both obtained with Berkovich indenter. The remarkable linearity of these data sets at all but the smallest depths (large $1/h$) has served as the primary evidence for the Nix-Gao model [81].

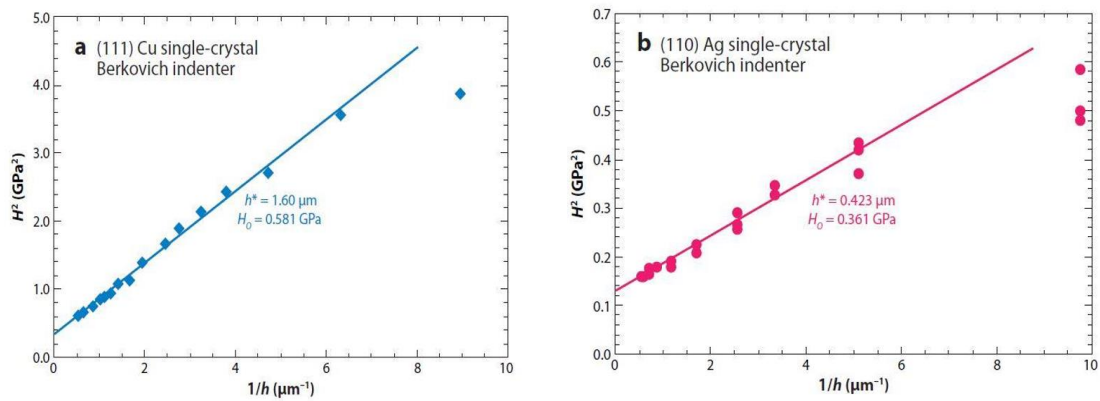


Figure 2.28: A plot of H^2 vs. $1/h$ for (a) Cu [84] (b) Ag [87].

2.8 Thermally activated dislocation mechanisms

During plastic deformation in certain ranges of temperature and strain rate, different micro mechanisms may play important roles and, therefore, one must consider the operative dislocation–based deformation mechanisms in order to explain the deformation behavior. The motion of dislocations through fields of discrete sub-micrometer sized particles was studied since the 1970 in connection with the plastic deformation of metals and alloys.

Considering ambient temperature plastic flow, in the FCC alloys, the stress necessary for dislocation motion can be divided into two components; athermal (called also internal stress) and thermally activated (called also effective stress) [80, 88, 89]. The athermal stress is related to long range obstacles and the creation of new dislocations leading to strain hardening. The athermal stress is only weakly depending upon temperature through the effect of temperature on the elastic modulus of the material. Athermal stress is strain rate independent and depends on the microstructure (grain size, precipitates, and dislocation–dislocation interactions). The athermal component can be written as:

$$\tau_i = \alpha\mu b\sqrt{\rho_t} \quad (2.24)$$

where μ is the elastic shear modulus, α is a constant describing the interaction between dislocations, and b is the Burgers vector of dislocations.

The thermal effective stress component is strain rate and temperature dependent (it increases when the strain rate increases or the temperature decreases). It is related to the interaction of the mobile dislocations with small discrete obstacles within the microstructure. The dislocation can only continue to move if they are able to overcome these obstacles with the combined help of the applied stress and thermal vibration.

The general expression for the applied flow stress is therefore given as the sum of the athermal and thermal components of the stress required to move a dislocation through a field of micro-structural scale obstacles as:

$$\tau = \tau_i + \tau^*(\tau, \dot{\gamma}) \quad (2.25)$$

where τ_i is the athermal, and τ^* is thermal component of the stress. The shear strain rate $\dot{\gamma}$ is directly related to the mean velocity \bar{v} of the dislocations by the Orowan equation [90]

$$\dot{\gamma} = \rho_m b \bar{v} \quad (2.26)$$

where ρ_m is the mobile dislocations density. The dislocation velocity is controlled by obstacles (their strength and inter-obstacle spacing), the temperature, and the effective applied shear stress as [90-92]:

$$\bar{v} = \beta b v \exp \left[\frac{-\Delta G_{Thermal}(\tau)}{kT} \right] \quad (2.27)$$

Where β is a dimensionless constant, v is the frequency of atomic vibration, and $\Delta G_{Thermal}(\tau)$ is the thermal activation energy required for a dislocation, subjected to an applied shear stress τ , to overcome the deformation-rate limiting obstacle. The resulting shear strain rate $\dot{\gamma}$, for such an obstacle-limited dislocation glide deformation process can be written in terms of an Arrhenius-type rate equation as:

$$\dot{\gamma} = \gamma_o \exp \left[\frac{-\Delta G_{Thermal}(\tau)}{kT} \right] \quad (2.28)$$

where the pre-exponent term γ_o is related to the total dislocation density, which can be expressed by $\rho_m = \alpha \left(\frac{\tau}{\mu b} \right)^2$, as:

$$\gamma_o = \dot{\gamma}_P \left(\frac{\tau}{\mu} \right)^2 \quad (2.29)$$

$$\dot{\gamma}_{ind} = \dot{\gamma}_P \left(\frac{\tau_{ind}}{\mu} \right)^2 \exp \left[\frac{-\Delta G_{Thermal}(\tau)}{kT} \right] = \dot{\gamma}_P \left(\frac{\tau}{\mu b} \right)^2 b^2 \exp \left[\frac{-\Delta G_{Thermal}(\tau)}{kT} \right] \quad (2.30)$$

$$\dot{\gamma}_{ind} = \dot{\gamma}_P \rho_m b^2 \exp \left[\frac{-\Delta G_{Thermal}(\tau)}{kT} \right] \quad (2.31)$$

2.9 Summary

The primary objective of this research is to investigate the effect of heavy ion irradiation at room temperature and helium implantation at high temperature on the mechanical properties and local plastic deformation parameters of Inconel X-750 spacer material in CANDU reactor. Descriptions of the theories, mechanisms and techniques which were applied to achieve the objective were discussed in this chapter. The following chapters include detailed descriptions of all the investigations carried out for this research. In addition, and to best of my knowledge, no studies have been performed on plasticity and kinetic deformation mechanism via thermal activation energy on Inconel X-750 to this date.

2.10 References

- [1] M. Stopher, The effects of neutron radiation on nickel-based alloys, *Materials Science and Technology* 33(5) (2017) 518-536.
- [2] J. Hunn, E. Lee, T. Byun, L. Mansur, Ion-irradiation-induced hardening in Inconel 718, *Journal of nuclear materials* 296(1-3) (2001) 203-209.
- [3] M. Griffiths, G. Bickel, S. Douglas, Irradiation-induced embrittlement of INCONEL 600 flux detectors in CANDU reactors, 18th International Conference on Nuclear Engineering, American Society of Mechanical Engineers Digital Collection, 2010, pp. 293-298.
- [4] O. Woo, C. Judge, H. Nordin, D. Finlayson, C. Andrei, The microstructure of unirradiated and neutron irradiated Inconel X750, *Microscopy and Microanalysis* 17(S2) (2011) 1852-1853.
- [5] Z. Yao, R. Schäublin, M. Victoria, The microstructure and tensile properties of pure Ni single crystal irradiated with high energy protons, *Journal of nuclear materials* 307 (2002) 374-379.

- [6] I. Robertson, J. Vetrano, M. Kirk, M. Jenkins, On the formation of vacancy type dislocation loops from displacement cascades in nickel, *Philosophical Magazine A* 63(2) (1991) 299-318.
- [7] R. Holt, M. Griffiths, R. Gilbert, c-Component dislocations in Zr-2.5 wt% Nb alloy, *Journal of Nuclear Materials* 149(1) (1987) 51-56.
- [8] H.K. Zhang, Z. Yao, G. Morin, M. Griffiths, TEM characterization of in-reactor neutron irradiated CANDU spacer material Inconel X-750, *Journal of Nuclear Materials* 451(1-3) (2014) 88-96.
- [9] M. Griffiths, The effect of irradiation on Ni-containing components in CANDU® reactor cores: a review, *Nuclear Review* 2(1) (2014) 1-16.
- [10] M. Griffiths, G. Bickel, S. Donohue, P. Feenstra, C. Judge, D. Poff, L. Walters, M. Wright, L. Greenwood, F. Garner, Degradation of Ni-alloy components in CANDU® reactor cores, Atomic Energy of Canada Limited, 2013.
- [11] "<http://www.civil.uwaterloo.ca/watrisk/research.html>.
- [12] H.K. Zhang, Z. Yao, C. Judge, M. Griffiths, Microstructural evolution of CANDU spacer material Inconel X-750 under in situ ion irradiation, *Journal of Nuclear Materials* 443(1-3) (2013) 49-58.
- [13] H.K. Zhang, Z. Yao, M.R. Daymond, M.A. Kirk, Elevated temperature irradiation damage in CANDU spacer material Inconel X-750, *Journal of Nuclear Materials* 445(1-3) (2014) 227-234.
- [14] H. Zhang, Z. Yao, M.R. Daymond, M.A. Kirk, Cavity morphology in a Ni based superalloy under heavy ion irradiation with cold pre-injected helium. I, *Journal of Applied Physics* 115(10) (2014) 103508.
- [15] H. Zhang, Z. Yao, M.R. Daymond, M.A. Kirk, Cavity morphology in a Ni based superalloy under heavy ion irradiation with hot pre-injected helium. II, *Journal of Applied Physics* 115(10) (2014) 103509.

- [16] C. Heintze, C. Recknagel, F. Bergner, M. Hernández-Mayoral, A. Kolitsch, Ion-irradiation-induced damage of steels characterized by means of nanoindentation, *Nuclear Instruments and Methods in Physics Research Section B: Beam Interactions with Materials and Atoms* 267(8-9) (2009) 1505-1508.
- [17] K. Murty, I. Charit, Structural materials for Gen-IV nuclear reactors: Challenges and opportunities, *Journal of Nuclear Materials* 383(1-2) (2008) 189-195.
- [18] P. Yvon, F. Carré, Structural materials challenges for advanced reactor systems, *Journal of Nuclear Materials* 385(2) (2009) 217-222.
- [19] S. Metals, inconel alloy x-750, Special Metals Corp., New Hartford, NY, Product Specifications SMC-067, available at: [http://www.specialmetals.com/documents/Inconel% 20alloy% 20X-750. pdf](http://www.specialmetals.com/documents/Inconel%20alloy%20X-750.pdf) (2004).
- [20] R.C. Reed, *The superalloys: fundamentals and applications*, Cambridge university press 2008.
- [21] C.D. Judge, *The Effects of Irradiation on Inconel X-750*, 2015.
- [22] C. Judge, M. Griffiths, L. Walters, M. Wright, G. Bickel, O. Woo, M. Stewart, S. Douglas, F. Garner, Embrittlement of Nickel Alloys in a CANDU Reactor Environment CANDU (CANadian Deuterium Uranium)® is a registered trademark of Atomic Energy of Canada Limited, *Effects of Radiation on Nuclear Materials: 25th Volume*, ASTM International 2013.
- [23] C.D. Judge, N. Gauquelin, L. Walters, M. Wright, J.I. Cole, J. Madden, G.A. Botton, M. Griffiths, Intergranular fracture in irradiated Inconel X-750 containing very high concentrations of helium and hydrogen, *Journal of Nuclear Materials* 457 (2015) 165-172.
- [24] H.K. Zhang, Z. Yao, M.A. Kirk, M.R. Daymond, Stability of Ni₃(Al, Ti) gamma prime precipitates in a nickel-based superalloy inconel X-750 under heavy ion irradiation, *Metallurgical and Materials Transactions A* 45(8) (2014) 3422-3428.

- [25] G.S. Was, *Fundamentals of radiation materials science: metals and alloys*, Springer 2016.
- [26] G. Kinchin, R. Pease, The displacement of atoms in solids by radiation, *Reports on progress in physics* 18(1) (1955) 1.
- [27] M. Li, M. Kirk, P. Baldo, D. Xu, B. Wirth, Study of defect evolution by TEM with in situ ion irradiation and coordinated modeling, *Philosophical Magazine* 92(16) (2012) 2048-2078.
- [28] P. Changizian, A. Brooks, Z. Yao, M. Daymond, Nano-scale Mechanical Properties and Microstructure of Irradiated X-750 Ni-Based Superalloy, *Metallurgical and Materials Transactions A* 49(2) (2018) 498-514.
- [29] C. Judge, V. Bhakhri, Z. Jiao, R. Klassen, G. Was, G. Botton, M. Griffiths, The effects of proton irradiation on the microstructural and mechanical property evolution of inconel X-750 with high concentrations of helium, *Journal of Nuclear Materials* 492 (2017) 213-226.
- [30] G. Was, Z. Jiao, E. Getto, K. Sun, A. Monterrosa, S. Maloy, O. Anderoglu, B. Sencer, M. Hackett, Emulation of reactor irradiation damage using ion beams, *Scripta Materialia* 88 (2014) 33-36.
- [31] A. E521-16, *Standard Practice for Investigating the Effects of Neutron Radiation Damage Using Charged-Particle Irradiation*, ASTM International West Conshohocken, PA, 2016.
- [32] L. Greenwood, F. Garner, Hydrogen generation arising from the ^{59}Ni (n, p) reaction and its impact on fission—fusion correlations, *Journal of Nuclear Materials* 233 (1996) 1530-1534.
- [33] F. Garner, L. Greenwood, B. Oliver, A reevaluation of helium/dpa and hydrogen/dpa ratios for fast reactor and thermal reactor data used in fission-fusion correlations, *Effects of Radiation on Materials: 18th International Symposium*, ASTM International, 1999.

- [34] S. Zinkle, 1.03-Radiation-Induced effects on microstructure, *Comprehensive nuclear materials* 1 (2012) 65-98.
- [35] R. Schäublin*, Z. Yao, N. Baluc, M. Victoria, Irradiation-induced stacking fault tetrahedra in fcc metals, *Philosophical magazine* 85(4-7) (2005) 769-777.
- [36] H. Ullmaier, Radiation damage in metallic materials, *Mrs Bulletin* 22(4) (1997) 14-21.
- [37] K.L. Murty, Role and significance of source hardening in radiation embrittlement of iron and ferritic steels, *Journal of nuclear materials* 270(1-2) (1999) 115-128.
- [38] E. Camus, C. Abromeit, F. Bourdeau, N. Wanderka, H. Wollenberger, Evolution of long-range order and composition for radiation-induced precipitate dissolution, *Physical Review B* 54(5) (1996) 3142.
- [39] J. Silcox, P. Hirsch, Direct observations of defects in quenched gold, *Philosophical Magazine* 4(37) (1959) 72-89.
- [40] M. Kiritani, Story of stacking fault tetrahedra, *Materials chemistry and physics* 50(2) (1997) 133-138.
- [41] J. Hunn, E. Lee, T. Byun, L. Mansur, Helium and hydrogen induced hardening in 316LN stainless steel, *Journal of Nuclear Materials* 282(2-3) (2000) 131-136.
- [42] J.J. Kai, F.R. Chen, T.S. Duh, Effects of grain boundary misorientation on radiation-induced solute segregation in proton irradiated 304 stainless steels, *Materials Transactions* 45(1) (2004) 40-50.
- [43] K. Farrell, P. Maziasz, E. Lee, L. Mansur, Modification of radiation damage microstructure by helium, *Radiation effects* 78(1-4) (1983) 277-295.
- [44] K. Farrell, Experimental effects of helium on cavity formation during irradiation—a review, *Radiation Effects* 53(3-4) (1980) 175-194.

- [45] J. Kai, G. Kulcinski, 14 MeV nickel-ion irradiated HT-9 ferritic steel with and without helium pre-implantation, *Journal of nuclear materials* 175(3) (1990) 227-236.
- [46] L. Mansur, W. Coghlan, Mechanisms of helium interaction with radiation effects in metals and alloys: A review, *Journal of Nuclear Materials* 119(1) (1983) 1-25.
- [47] M. Lewis, Diffusion and trapping of ion-implanted helium in nickel, *Journal of Nuclear Materials* 149(2) (1987) 143-149.
- [48] J. Knapp, D. Follstaedt, S. Myers, Hardening by bubbles in He-implanted Ni, *Journal of applied physics* 103(1) (2008) 013518.
- [49] R. Scattergood, D. Bacon, The strengthening effect of voids, *Acta Metallurgica* 30(8) (1982) 1665-1677.
- [50] P. Coulomb, On the blocking of dislocations by cavities and small precipitate particles, *Acta Metall* 7 (1959) 556-559.
- [51] R.E. Stoller, The role of cascade energy and temperature in primary defect formation in iron, *Journal of nuclear materials* 276(1-3) (2000) 22-32.
- [52] F. Carsughi, H. Derz, P. Ferguson, G. Pott, W. Sommer, H. Ullmaier, Investigations on Inconel 718 irradiated with 800 MeV protons, *Journal of nuclear materials* 264(1-2) (1999) 78-88.
- [53] M.L. Jenkins, M. Wilkens, Transmission electron microscopy studies of displacement cascades in Cu₃Au: H. Experimental investigation of cascades produced by energetic Cu⁺ ions, *Philosophical Magazine* 34(6) (1976) 1155-1167.
- [54] E. Schulson, The ordering and disordering of solid solutions under irradiation, *Journal of Nuclear Materials* 83(2) (1979) 239-264.
- [55] M. Yamaguchi, V. Paidar, D. Pope, V. Vitek, Dissociation and core structure of $\langle 110 \rangle$ screw dislocations in L1₂ ordered alloys I. Core structure in an unstressed crystal, *Philosophical Magazine A* 45(5) (1982) 867-882.

- [56] V. Paidar, M. Yamaguchi, D. Pope, V. Vitek, Dissociation and core structure of $\langle 110 \rangle$ screw dislocations in L12 ordered alloys II. Effects of an applied shear stress, *Philosophical Magazine A* 45(5) (1982) 883-894.
- [57] C. Abromeit, S. Müller, N. Wanderka, Stability of γ' phase in the stoichiometric Ni₃Al alloy under ion irradiation, *Scripta metallurgica et materialia* 32(10) (1995) 1519-1523.
- [58] R. Nelson, J. Hudson, D. Mazey, The stability of precipitates in an irradiation environment, *Journal of Nuclear Materials* 44(3) (1972) 318-330.
- [59] N. Hashimoto, J. Hunn, T. Byun, L. Mansur, Microstructural analysis of ion-irradiation-induced hardening in inconel 718, *Journal of nuclear materials* 318 (2003) 300-306.
- [60] P. Hosemann, C. Shin, D. Kiener, Small scale mechanical testing of irradiated materials, *Journal of Materials Research* 30(9) (2015) 1231.
- [61] P. Hosemann, J. Swadener, D. Kiener, G. Was, S. Maloy, N. Li, An exploratory study to determine applicability of nano-hardness and micro-compression measurements for yield stress estimation, *Journal of Nuclear Materials* 375(1) (2008) 135-143.
- [62] A.C. Fischer-Cripps, Critical review of analysis and interpretation of nanoindentation test data, *Surface and coatings technology* 200(14-15) (2006) 4153-4165.
- [63] K. Johnson, The correlation of indentation experiments, *Journal of the Mechanics and Physics of Solids* 18(2) (1970) 115-126.
- [64] W.C. Oliver, G.M. Pharr, Measurement of hardness and elastic modulus by instrumented indentation: Advances in understanding and refinements to methodology, *Journal of materials research* 19(1) (2004) 3-20.
- [65] I.N. Sneddon, The relation between load and penetration in the axisymmetric Boussinesq problem for a punch of arbitrary profile, *International journal of engineering science* 3(1) (1965) 47-57.

- [66] J.T. Busby, M.C. Hash, G.S. Was, The relationship between hardness and yield stress in irradiated austenitic and ferritic steels, *Journal of Nuclear Materials* 336(2-3) (2005) 267-278.
- [67] D. Tabor, *The hardness of metals*, Oxford university press 2000.
- [68] A. Bolshakov, G. Pharr, Influences of pileup on the measurement of mechanical properties by load and depth sensing indentation techniques, *Journal of materials research* 13(4) (1998) 1049-1058.
- [69] J. Chen, Y. Shen, W. Liu, B.D. Beake, X. Shi, Z. Wang, Y. Zhang, X. Guo, Effects of loading rate on development of pile-up during indentation creep of polycrystalline copper, *Materials Science and Engineering: A* 656 (2016) 216-221.
- [70] K. McElhaney, J.J. Vlassak, W.D. Nix, Determination of indenter tip geometry and indentation contact area for depth-sensing indentation experiments, *Journal of Materials research* 13(5) (1998) 1300-1306.
- [71] W. Lee, Y. Chen, Simulation of micro-indentation hardness of FCC single crystals by mechanism-based strain gradient crystal plasticity, *International Journal of Plasticity* 26(10) (2010) 1527-1540.
- [72] H. Pollock, D. Maugis, M. Barquins, *Microindentation techniques in materials science (ASTM STP 899)*, American Society for Testing and Materials, Philadelphia, PA, 1986.
- [73] W. LaFontaine, B. Yost, R. Black, C.-Y. Li, Indentation load relaxation experiments with indentation depth in the submicron range, *Journal of Materials Research* 5(10) (1990) 2100-2106.
- [74] M. Mayo, W. Nix, *Strength of Metals and Alloys*, edited by Kettunen, PO, Lepisto, TK, and Lehtonen, ME, Pergamon, Oxford, 1988.
- [75] C. Charitidis, Multiscale approach of hardness in aluminium alloy: consideration of rate dependent behaviour, *Materials Science and Technology* 28(9-10) (2012) 1127-1134.

- [76] B. Lucas, W. Oliver, Indentation power-law creep of high-purity indium, *Metallurgical and materials Transactions A* 30(3) (1999) 601-610.
- [77] D. Peykov, E. Martin, R.R. Chromik, R. Gauvin, M. Trudeau, Evaluation of strain rate sensitivity by constant load nanoindentation, *Journal of Materials Science* 47(20) (2012) 7189-7200.
- [78] R. Schwaiger, B. Moser, M. Dao, N. Chollacoop, S. Suresh, Some critical experiments on the strain-rate sensitivity of nanocrystalline nickel, *Acta materialia* 51(17) (2003) 5159-5172.
- [79] M. Haghshenas, L. Wang, R. Klassen, Depth dependence and strain rate sensitivity of indentation stress of 6061 aluminium alloy, *Materials Science and Technology* 28(9-10) (2012) 1135-1140.
- [80] M. Haghshenas, R. Klassen, Indentation-based assessment of the dependence of geometrically necessary dislocations upon depth and strain rate in FCC materials, *Materials Science and Engineering: A* 586 (2013) 223-230.
- [81] W.D. Nix, H. Gao, Indentation size effects in crystalline materials: a law for strain gradient plasticity, *Journal of the Mechanics and Physics of Solids* 46(3) (1998) 411-425.
- [82] H. Gao, Y. Huang, W. Nix, J. Hutchinson, Mechanism-based strain gradient plasticity—I. Theory, *Journal of the Mechanics and Physics of Solids* 47(6) (1999) 1239-1263.
- [83] Y. Huang, H. Gao, W. Nix, J. Hutchinson, Mechanism-based strain gradient plasticity—II. Analysis, *Journal of the Mechanics and Physics of Solids* 48(1) (2000) 99-128.
- [84] N. Fleck, G. Muller, M.F. Ashby, J.W. Hutchinson, Strain gradient plasticity: theory and experiment, *Acta Metallurgica et materialia* 42(2) (1994) 475-487.

- [85] W.D. Nix, J.R. Greer, G. Feng, E.T. Lilleodden, Deformation at the nanometer and micrometer length scales: Effects of strain gradients and dislocation starvation, *Thin Solid Films* 515(6) (2007) 3152-3157.
- [86] G.M. Pharr, E.G. Herbert, Y. Gao, The indentation size effect: a critical examination of experimental observations and mechanistic interpretations, *Annual Review of Materials Research* 40 (2010) 271-292.
- [87] N. Fleck, J. Hutchinson, A reformulation of strain gradient plasticity, *Journal of the Mechanics and Physics of Solids* 49(10) (2001) 2245-2271.
- [88] C. Gao, L. Zhang, A constitutive model for dynamic plasticity of FCC metals, *Materials Science and Engineering: A* 527(13-14) (2010) 3138-3143.
- [89] Z. Trojanová, K. Máthis, P. Lukáč, G. Németh, F. Chmelík, Internal stress and thermally activated dislocation motion in an AZ63 magnesium alloy, *Materials Chemistry and Physics* 130(3) (2011) 1146-1150.
- [90] H.J. Frost, M.F. Ashby, *Deformation mechanism maps: the plasticity and creep of metals and ceramics*, Pergamon press 1982.
- [91] U.F. Kocks, A. AS, A. MF, *Thermodynamics and kinetics of slip*, (1975).
- [92] A. Haseeb, Modeling of the effects of athermal flow strength and activation energy for dislocation glide on the nanoindentation creep of nickel thin film at room temperature, *Computational materials science* 37(3) (2006) 278-283.

Chapter 3

3 Effect of high temperature He⁺ and room temperature Ni⁺ implantation on grain by grain indentation hardness of Inconel X-750

In this study we investigated the effect of irradiation damage and accumulated helium on the hardness and indentation size effect (ISE) of Inconel X-750. Both He⁺ at 300 °C and Ni⁺ ion implantation at 25 °C at lower doses resulted in softening of the X-750 alloy and this might be attributed to the diffusion of He⁺ to dislocations, and precipitate-matrix interfaces or partial annihilation of dislocation network at 300 °C ($C_{He} = 100$ appm) and disordering of γ' precipitates at 25 °C ($\psi_{Ni} = 0.01$ and 0.1 dpa). The hardening behavior observed at higher irradiation damage ($\psi_{Ni} = 1$ dpa) was due to increases in defect density acting as irradiation obstacles. At $\psi_{Ni} = 5$ dpa the hardness is decreased by 8% from as received due to overlapping/saturation of defects and dissolution γ' at higher irradiation dosage.

3.1 Introduction

Garter spring spacers are essential components of CANDU nuclear reactors. They are not only used to maintain an insulating gas gap, but also separate the pressure tubes from the calandria tubes within the fuel channels. The spacers are made of the heat-treated Ni-based alloy Inconel X-750. This alloy is strengthened by both incoherent (TiC, NbC, and Cr₂₃C₆) and coherent Ni₃ (Al,Ti) γ' precipitates. The alloy retains its strength and creep resistance at elevated temperature due to the high thermal stability of the γ' precipitates. High energy particle, ion or neutron, irradiation has been observed to destabilize γ' precipitates in Ni-based alloys [1-3]. The temperature dependence of this destabilization is unusual in that γ' precipitates appear to become disordered during low temperature neutron irradiation but remain stable during high temperature neutron irradiation [2, 4-6]. Inconel X-750 in-reactor components are also exposed to significant helium accumulation as a result of ongoing ^{59}Ni (n,α) ^{56}Fe transmutation. The helium accumulation within Inconel X-750 spacers can reach

approximately 40,000 appm by the end of its service life in a CANDU nuclear reactor [7]. The effect of accumulated helium on promoting hardening and embrittlement of metals is well established and is correlated to the formation of cavities/bubbles at grain boundaries and at precipitate/matrix interfaces [3, 8-12]. It has been reported that in ex-service spacers high temperature (260 °C- 310 °C) irradiation results in larger cavities/bubbles along grain boundaries when compared with lower temperatures. [9, 11-13]. The use of high energy ion implantation to simulate the effect neutron irradiation on material's microstructure and mechanical properties has now become well accepted and frequently used to study the effect of neutron-induced crystal damage on the properties of nuclear materials [14]. Ion implantation temperature may significantly affect the rate of ion-induced microstructural changes. For example, helium cavity nucleation was noticed only when He⁺ implantation temperature was performed above 200 °C, and γ' precipitate disordering was only observed at relatively low implantation temperature [11, 15]. Therefore, in this study we sought to investigate the effect of Ni⁺ and He⁺ ion irradiation at different temperatures on the grain by grain nano indentation hardness of Inconel X-750.

3.2 Experimental procedure

3.2.1 Test material

The chemical composition of the Inconel X-750 alloy used in this study is given in Table 3-1. The alloy was annealed at 1010 °C (30 min) followed by air cooling to room temperature, cold working by 18%, and then ageing at 728 °C (16 h). The average grain size was found to be between 25 and 50 μm . Four samples (6 \times 6 \times 3 mm) were cut by EDM from the aged X-750 material. The samples were mechanically ground with successively finer grit SiC impregnated papers and then polished in an aqueous slurry of 0.02 μm diameter colloidal SiO₂. This process created a surface free of polishing-induced plastic deformation. As-received sample by SEM were lightly sputter polished/etched with low energy (10 keV) Cs⁺ ions to reveal grain structure and was imaged with high-resolution back-scattered electrons (Figure 3.1). Finally, in order to reveal grains and grain boundaries the samples were chemically etched by immersion in a solution of equal parts HCL, HNO₃

, and acetic acids for 40 seconds [16]. The chemical solution was removed by rinsing the samples with distilled water and blowing it dry in air .

Table 3-1: Chemical Composition of the Inconel X-750 (wt.%) [7]

Elements	Ni	Cr	Fe	Nb	Co	Mn	Cu	Al	Ti	Si	C
Bal.	70	14.0-17.0	5.0-9.0	0.7-1.2	1.0	1.0	0.5	0.4-1.0	2.25-2.75	0.5	0.08

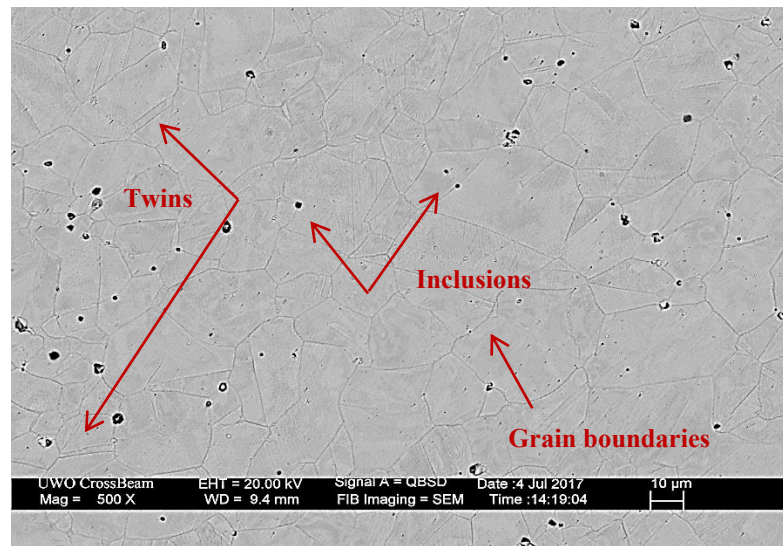


Figure 3.1: SEM image of chemically etched sample of the X-750 alloy which contains twins and inclusions as incoherent carbides (TiC, NbC) and small carbides (MC) Cr₂₃C₆.

3.2.2 Ion implantation

Set of Inconel X-750 samples were Ni⁺ implanted at 25 °C to create levels of irradiation damage up to $\psi_{Ni} = 5$ dpa without significantly changing the chemical composition of the Ni-based alloy. Sequential Ni⁺ implantations were performed at thirteen kinetic energy levels, from 2 to 8 MeV, with a high current tandem ion accelerator at the University of Western Ontario, London, Ontario Canada to invoke uniform irradiation damage over a depth of about 3 μm (Figure 3.2-c). The Ni⁺ exposure was controlled to achieve calculated average levels of $\psi_{Ni} = 0.01, 0.1, 1.0$ and 5.0 dpa. Another set of samples were He⁺

implanted at 300 °C in fourteen kinetic energy levels, from 0.3 to 1.6 MeV, to ensure uniform helium concentration to a depth of about 3 μm (Figure 3.2-d). The ion beam exposure was controlled to achieve average helium concentrations of $C_{\text{He}} = 100, 1000,$ and 5000 appm. The average atomic displacements induced by these implantations were 0.001, 0.01, 0.05 dpa respectively. The Stopping Range of Ions in Matter (SRIM-2013) software, was used to calculate the average implanted ion depth and the average ion-induced crystal damage using the Kinchin-Pease approximation [17] with threshold displacement energy of 40 eV. Table 2 lists the ion implantation conditions tested.

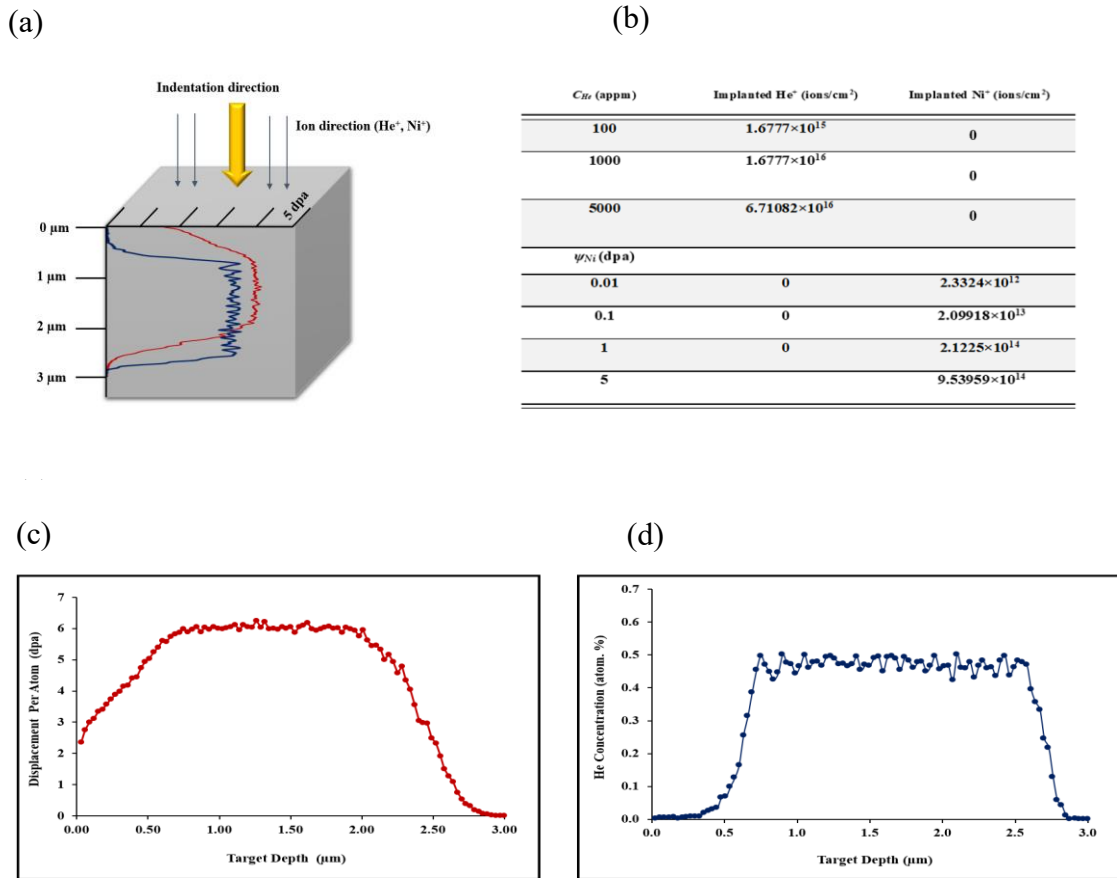


Figure 3.2: (a) Schematic illustration of irradiation and indentation direction with SRIM profile for He^+ and Ni^+ irradiation (b) He^+ and Ni^+ conditions along with number of ions (c) Ni^+ ion irradiation, depicting displacement damage dose variation vs target depth for samples irradiated up to $\psi_{\text{Ni}} = 5$ dpa with thirteen kinetic energy levels ($E_{\text{Ni}^+} = 2 - 8$ MeV) (d) SRIM simulation for helium implantation, showing helium concentration as a function of target depth with fourteen consecutive He^+ ion implantation energies ($E_{\text{He}^+} = 0.3 - 1.6$ MeV).

3.2.3 Electron Backscatter Diffraction (EBSD)

EBSD scans were performed to identify the grains, upon which the indentation hardness tests were performed. No surface preparation was required for EBSD after the ion implantations. Eight EBSD scans of approximately $500 \times 350 \mu\text{m}$ were sequentially acquired with a step size of $1\mu\text{m}$ over the entire sample surface (Figure 3.3). MTEX 4.5.2 [18] free software for the MATLAB 2018a environment was used to construct grain maps and grains statistic.

3.2.4 Nanoindentation hardness testing

Grain by grain nanoindentation hardness tests were used to assess the effect of He^+ and Ni^+ implantation on the hardness of the variously oriented matrix grains within the ion-implanted X-750 samples. For each implantation condition at least ten grains (Figure 3.3) were selected and nanoindentation hardness tests were performed on them with a Nano-Test indentation testing platform (Micro Materials Ltd, Wrexham UK). The tests were performed with a diamond Berkovich indenter, at a constant indentation loading rate of $\dot{P} = 1\text{mNs}^{-1}$ and to the max total indentation depth of $h_{max} = 500 \text{ nm}$. All indentation tests performed in this study were made to a plastic indentation depth of about 400 nm . The reason for considering the hardness at this depth is to make sure that the hardness measurement is carried out within the irradiated depth of the sample. If we assume that the plastic zone is 5 times bigger than the indentation depth [19, 20] then, for sampling within the irradiated depth (about $3 \mu\text{m}$), the plastic indentation depth should be less than 600 nm . The area, A_p , of the indentation, projected normal to the indentation direction, can be calculated from h_p , which for a perfect three-sided pyramidal ‘‘Berkovich’’ indenter, is given as:

$$A_p = \pi \cdot \tan^2 \alpha \cdot h_p^2 = 24.5h_p^2 \quad (3.1)$$

where $\alpha = 70.32^\circ$ and represent the effective semi-angle of the conical indenter equivalent to the Berkovich [21]. The area function of an actual indenter will be affected by a certain

amount of indenter tip rounding causing A_p to typically be expressed by a higher order function of h_p . In this case $A_p(h_p)$ is determined experimentally by performing indentations on a standard of well-known hardness, such as quartz or sapphire. The area function in conjunction with the force allows the indentation hardness, H , to be calculated as:

$$H = \frac{P}{A_p(h_p)} \cong \frac{P}{24.5(h_p)^2} \quad (3.2)$$

In order to minimize the effect of grain boundaries and the neighboring grains on the measured hardness, the indentation tests were only performed in the center of large grains of diameter greater than $40 \mu\text{m}$. Another set of experiment of 12 indents (4×3 matrix) as series of indents were made to the max depth of $h_{max} = 1200 \text{ nm}$ in 11 partial unloading. Each indent spaced $25 \mu\text{m}$ apart to ensure that the plastic zones of individual indentations did not overlap. In this way, the hardness was measured at precisely controlled locations and the variation of hardness through the $3 \mu\text{m}$ ion-implanted zone could be assessed.

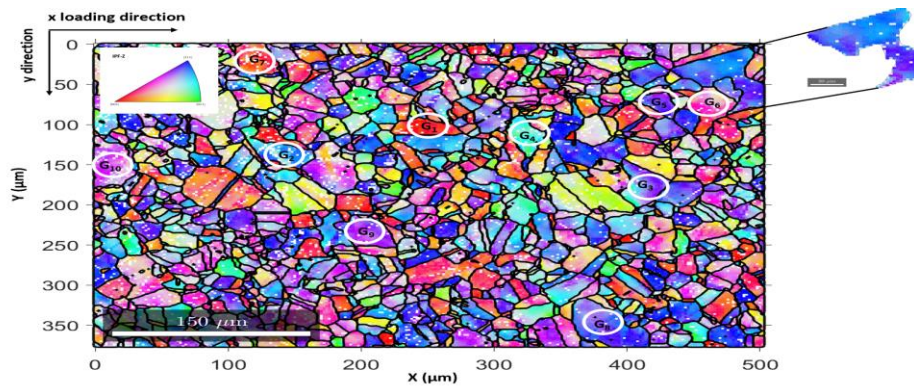


Figure 3.3: $500 \times 350 \mu\text{m}$ EBSD map of crystal orientation of an Inconel X-750 for as-received sample ($C_{He} = 0 \text{ appm}$, $\psi_{Ni} = 0 \text{ dpa}$). The location of nine indentations are shown by white circles.

Instrumented indentation testers use a well-established method in which an indenter tip with a known geometry is driven into a specific area of the material to be tested by applying an increasing normal load. The indentation depth is monitored throughout the experiment by means of a displacement sensor. For each loading-unloading cycle, the applied load value is plotted with respect to the corresponding position of the indenter. The resulting load vs. indentation depth curves provide data specific to the mechanical nature of the

material under examination [21]. Established models, see Eqs. (3.1, 3.2), are used to calculate quantitative hardness values from the data [21].

3.2.5 Microstructure evaluation

In order to establish a link between nanohardness parameters determined in this study and the irradiation effect of He^+ and Ni^+ on microstructural evolution, previously published data from Zhang et al. [11, 15] were adapted. These data included microstructural changes examined from TEM results after separate Kr^{+2} at 60 °C irradiation ($\psi = 0.01, 0.06, 0.27, 0.68, 2.7$ and 5.4 dpa) and high pre implanted He^+ at 400 °C ($C_{\text{He}} = 400, 1000$ and 5000 appm) on Inconel X-750. In order to derive equivalent microstructural changes for the doses used in the current study, the original data were replotted and fitted with the best fit curve (polynomial second order) and equivalent microstructural values were calculated from the equation derived. Zhang et al. showed that there was a correlation between defect number density and heavy ion irradiation doses but not with the defect size (SFT and dislocation loops) between 60 °C to 400 °C. However, in the case of high implanted He^+ , there was a strong correlation between both cavity size and density with increasing He^+ implanted doses. Therefore, in this study we choose to show the most affected microstructural changes with heavy ion irradiation and He^+ implantation doses meaning defect number density in the case of Ni^+ irradiation and both cavity size and density for He^+ implantation.

3.3. Results and discussion

3.3.1 Effect of irradiation damage on the hardness of Inconel X-750

Grain by grain nano-hardness profiles as a function of 25 °C Ni^+ induced displacement damage, from $\psi_{\text{Ni}} = 0$ to 5 dpa, is plotted in Figure 3.4.

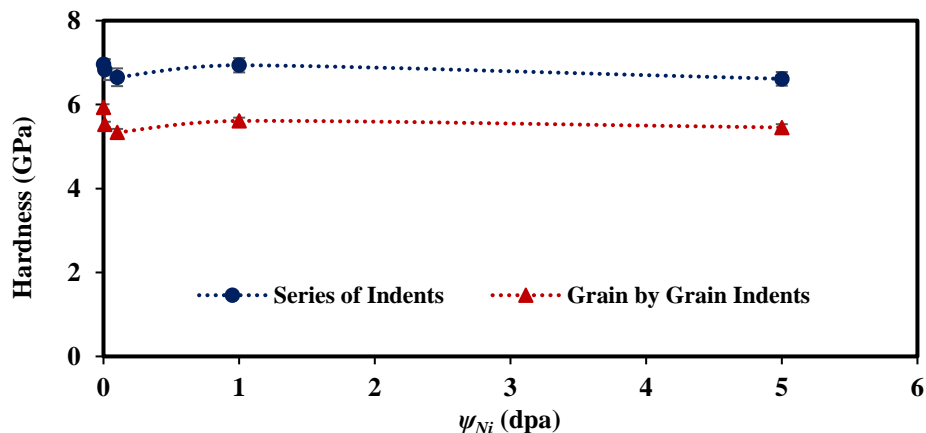


Figure 3.4: Average indentation hardness versus ion irradiation damage for the Inconel X-750 samples $\psi_{Ni} = 0.01, 0.1, 1,$ and 5 dpa for both series and grain by grain hardness testing at 400 nm depth. Error bars represent the measurement of the amount of variation of hardness data for 10 to 12 indents for both experiments.

Hardness values were indicated at $h = 400$ nm when multi-energy ion implantations are used. In the non-implanted state (as-received sample), the Inconel X-750 alloy was displayed a high nanoindentation hardness of about 6.0 ± 0.07 GPa in grain by grain and 7.0 ± 0.1 GPa in series of indents which is consistent with its age hardened state. The results show an increase trend in hardness with increasing ψ_{Ni} . However, a drop in this trend occurs in the early implantation stages, between $\psi_{Ni} = 0$ and 0.1 dpa when the hardness is dropped by about 10% in grain by grain and for series of indents about 5%. The indentation hardness then increases steadily with increasing ψ_{Ni} beyond 0.1 dpa. Nano-indentation hardness values presented in this study for this dose are similar to previously reported findings on X-750 [22, 23] and other superalloy [24]. In-situ TEM observation of irradiation-induced γ' instability by Zhang et al. have shown that disordering of the γ' hardening phase after a low dose of 0.06 dpa at irradiation temperature less than 400 °C [14] which is also supported by [23] as at lower dose of $\psi_{Ni} = 0.1$ and 0.5 dpa the superlattice reflections disappeared, indicating that γ' disordering has occurred. Therefore, it can be strongly anticipated that disordering also occurred in the irradiated 0.1 dpa sample. Although increases in Ni^+ ions dose produces an increasingly significant number of defects in the microstructure, disordering of γ' precipitates likely overbalance the hardening effect of the defects and is the main reason of irradiation-induced softening behaviour during nano-indentation as it is shown in Figure 3.5.

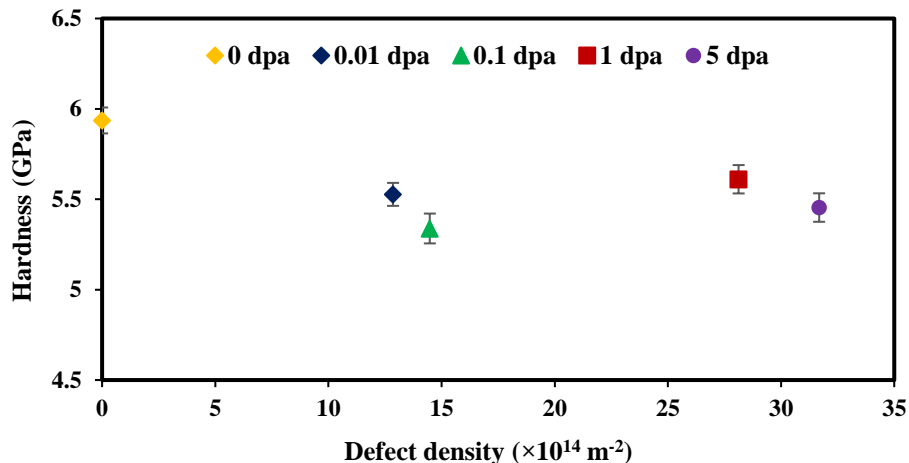


Figure 3.5: Average indentation hardness versus defect density. Defect density data assumed equivalent to those reported in from [25].

Similar softening behaviour was reported after ion irradiation of precipitation-hardened Inconel 718 [24, 26]. Interpretation of the reduced strength can be achieved by understanding the deformation mechanism of the γ' phase in the ordered condition versus the disordered state. The ordered strengthening, which originates from the formation of antiphase boundaries (APB_s) in the ordered γ' phase, plays a dominant role in the strengthening. There is a recent report showing that at the higher implantation levels, i.e. 1 dpa, a re-formation of Ti/Al rich regions are observed but in a disordered state (i.e. no super-lattice diffraction spots arise). These incoherent Al/Ti rich regions (precipitates), still harden the alloy. [23]. Similar formation of precipitates at 1 dpa was previously reported, under similar ion implantation conditions (dose and temperature), in other Ni superalloys [27, 28]. As a result, the high density of defects including dislocation loops generated during irradiation are strong obstacles for subsequent dislocation movement. This is confirmed by about 5% increase hardness in $\psi_{Ni} = 1$ dpa compared to 0.1 dpa in grain by grain nanoindentation hardness testing. However, in $\psi_{Ni} = 5$ dpa vs 1 dpa γ' starts to dissolve into the matrix and saturation of defects occurs [2], so the hardness values decreased by about 3%. In grain by grain indents, we tried to avoid grain boundaries, artifacts, and twins. It should be noted, however, that other investigations have not reported a reformation of Ti/Al rich regions resulting from ion implantation crystal damage [2]. Therefore, continued studies are required to completely characterize the microstructural evolution of ion-implanted Inconel X-750.

3.3.2 Effect of helium accumulation on the hardness of Inconel X-750

As mentioned previously, He^+ implantation in this study was carried out at 300 °C. This is important as helium cavity nucleation was reported when He^+ implantation temperature was above 200 °C [12, 15]. Figure 3.6 indicates that the hardness of the Inconel X-750 increases continuously with increasing helium concentration.

The difference between the hardness results of grain by grain versus series indentation, could be attributed mainly due to grain size, grain boundaries and twins which were avoided in grain by grain indentation. It is assumed that nano indentation of these locations could result in higher hardness value as was seen in series indents.

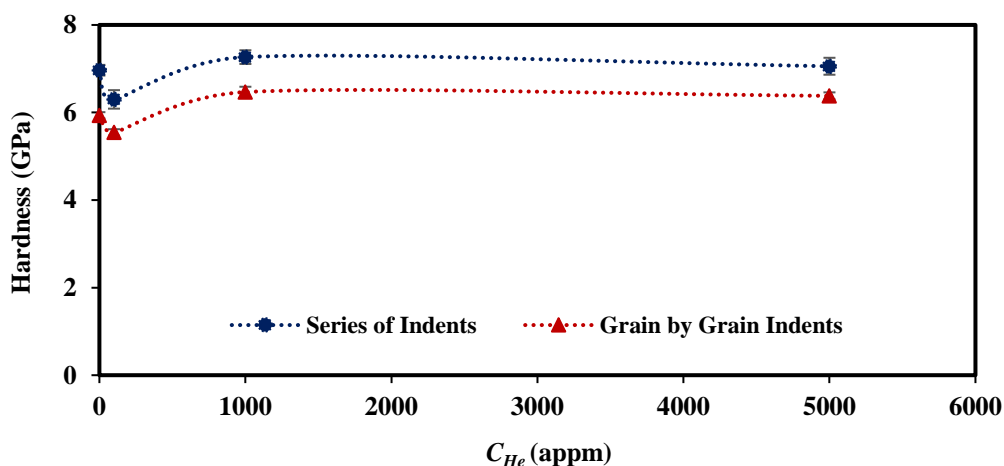


Figure 3.6: Average indentation hardness versus accumulated helium content for the Inconel X-750 samples $C_{\text{He}} = 100, 1000, 5000$ appm for both series and grain by grain hardness testing. Error bars represent the measurement of the amount of variation of hardness data for 10 to 12 indents in both experiments.

This is consistent with previous reports on the effect of implanted helium on increasing indentation hardness of pure Ni due to production of helium nano-/micro-cavities which act as obstacles to dislocation glide [10]. Based on Zhang et al [12] helium pre-injection at room temperature produced minor irradiation damages including tiny defect clusters and no obvious cavities. This implies that diffusion of helium is greatly dependent on the injection temperature. It should be noted that helium pre-injection at high temperature is preferred for simulating the actual migration of the transmutation produced helium in a

nuclear reactor. In our study, the lower hardness at $C_{He} = 100$ appm ($\sim 5.54 \pm 0.07$ GPa) compared to as-received ($\sim 6.0 \pm 0.07$ GPa) might be attributed to the migration of helium to dislocations, grain boundaries, and precipitate-matrix interfaces. This process is greatly depended upon the implantation temperature, and the rate of partial annihilation of dislocation networks [11, 29] as indicated by previously reported observation that the hardness doesn't drop with C_{He} at room temperature [23]. We observed, an increase in hardness between $C_{He} = 100$ and 1000 appm and this is consistent with increased He cavity size/ density (Figure 3.7). The indentation hardness at $C_{He} = 1000$ appm, to $C_{He} = 5000$ appm remains essentially constant (whin experimental error). Similar observations were reported previously for He^+ implanted Inconel 718 [24, 26].

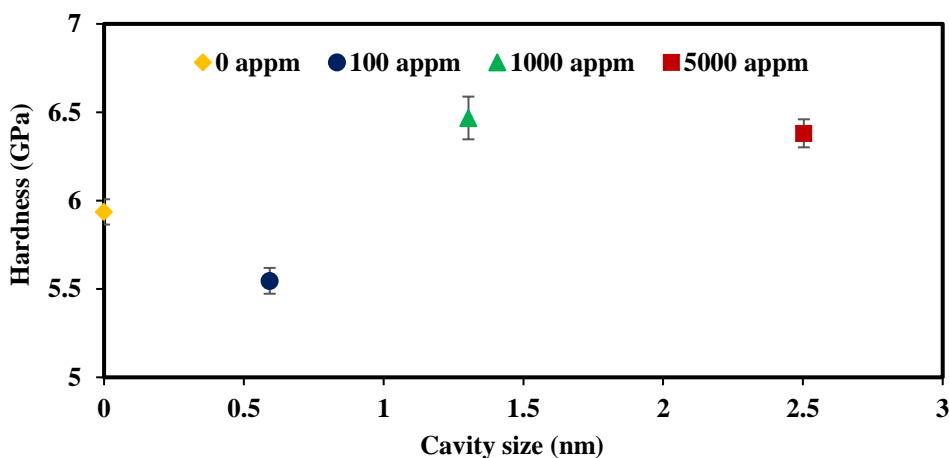


Figure 3.7. Average indentation hardness versus cavity size. TEM cavity size data were extracted from [11].

3.3.3 Indentation size effect in unirradiated vs. irradiated material

As expected, decreasing hardness with increasing indentation depth was observed in the indentation behavior for all tested materials. This is called the indentation size effect (ISE), which is well explained by Nix and Gao [30] based on the concept of geometrically necessary dislocations (GND_s), that is, dislocations that must be present to accommodate the imposed strain by the indenter at the surface [31]. To quantify the ISE in the irradiated

and un-irradiated X-750, the Nix-Gao (NG) was employed which gives a relation between the hardness and indentation depth according to Eq. (3.3):

$$\frac{H}{H_0} = \sqrt{1 + \frac{h^*}{h}} \quad (3.3)$$

where H is the indentation hardness at the depth of the h , H_0 is the macroscopic hardness, i.e., the hardness at a very large depth and h^* is the characteristic depth, which characterizes the depth-dependence of hardness. Figure 8 shows the average indentation hardness plotted versus indentation depth between for (a) as-received, (b) $\psi_{Ni} = 0.1$ dpa and (c) $C_{He} = 1000$ appm, implanted X-750 samples. For all test conditions, decreasing hardness with increasing indentation depth was observed. We have used the popular Nix-Gao model to quantify the dependence of the ISE upon displacement per atom (dpa) and helium concentration (appm) in Figure 3.8.

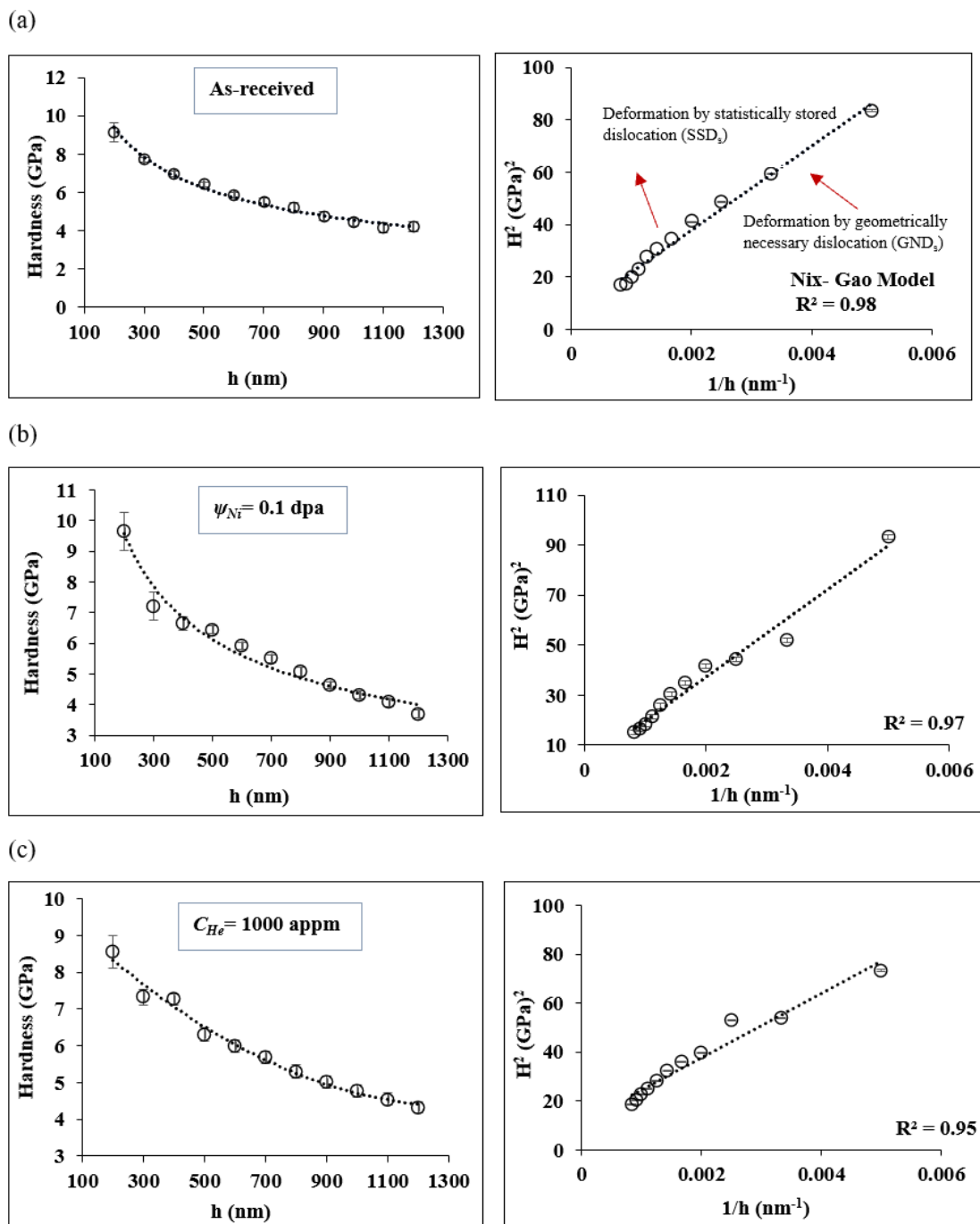


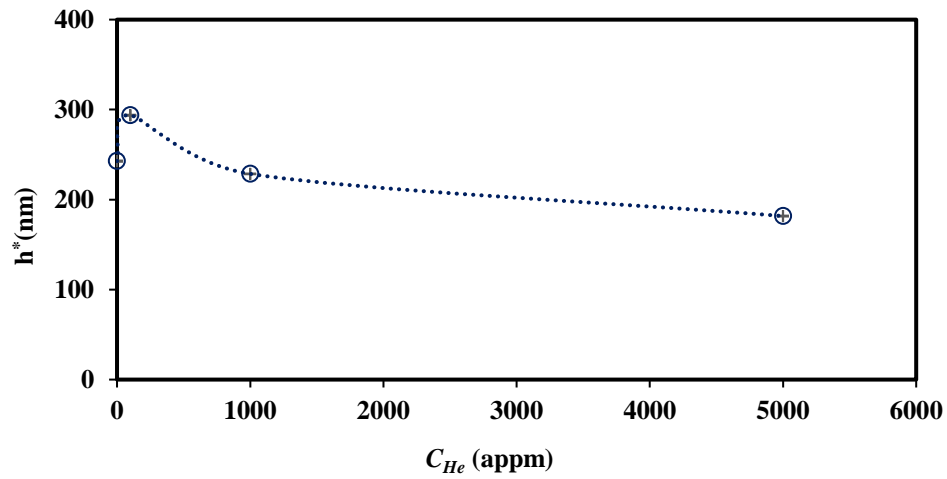
Figure 3.8: Indentation hardness as a function of indentation depth and ISE behaviour for (a) as-received (b) $\psi_{Ni} = 0.1$ dpa (c) $C_{He} = 1000$ appm. The error bars represent the measurement of the amount of variation of hardness data.

The Nix–Gao model agrees well with the linear relation between H^2 and $1/h$ especially for large indentation depths for all samples. However, in as received sample, in $1/h$ values above 0.002 nm (h less than 500 nm), clear scatters are observed in the data indicating that Nix-Gao model may deviate for shallow indents. This is attributed to sample surface effects and artifacts, indenter tip radius as well as large density of GNDs near the surface [32-35]. However, when plastic deformation is controlled by previously established dislocation structures in the larger depth of indentation, the imposed strain is accommodated by source-limited dislocation structures when the deformation volume is small. The source-limited deformation mechanism has also been observed by Shan et al. [36] through in situ nano-compression experiments inside a TEM during deformation of pure nickel pillars of different sizes. They found a stepwise stress increasing trend rather than continuous increasing, which was attributed to the progressive exhaustion of dislocation sources. Indeed, they showed that if there are enough productive dislocation sources to accommodate the deformation, a stress drop will occur; however, the stress will increase when there are limited dislocation sources, or the pre-existing sources become exhausted. The results presented in Table 3.2 for h^* reduction after irradiation implies a lower size effect in irradiated material vs. un-irradiated X-750, which agrees with the observations of previous authors in other irradiated FCC materials [19, 37]. Figure 3.9-a presents the characteristic indentation depth h^* decreasing with increasing helium concentration levels. For instance, h^* is decreased from $h^* = 243$ to 182 nm, when implanted to 5000 appm at 300°C. In contrast, nickel implantation results in a pronounced change in h^* and hence a change in the ISE of the X-750. When Ni^+ was implanted to 0.1 dpa h^* increases by 28% ($h^* = 243$ to 312 nm in Figure 3.9-b).

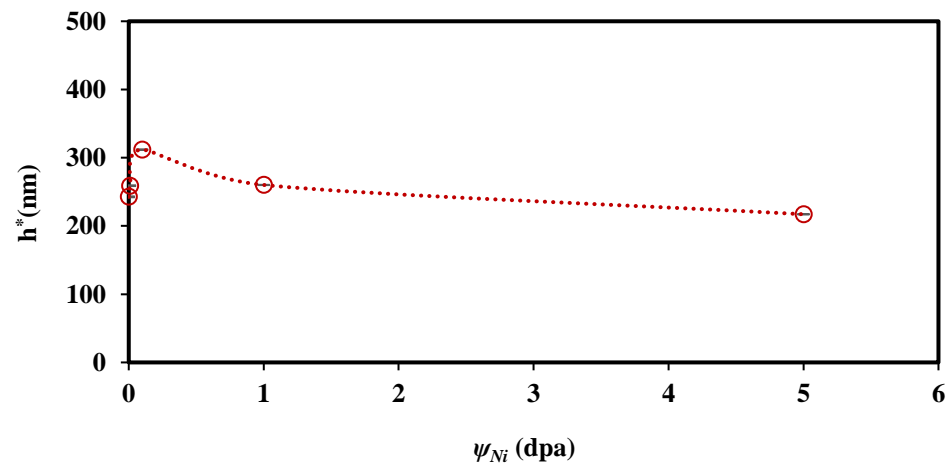
Table 3-2: The measured values of H_o (GPa) and h^* (nm) versus irradiation doses.

Unit	Doses	H_o (Gpa)	h^* (nm)
As-received	0	4.20	243
dpa	0.01	4.06	259
	0.1	3.70	312
	1	4.10	260
	5	4.0	217
appm	100	3.81	294
	1000	4.32	229
	5000	4.85	182

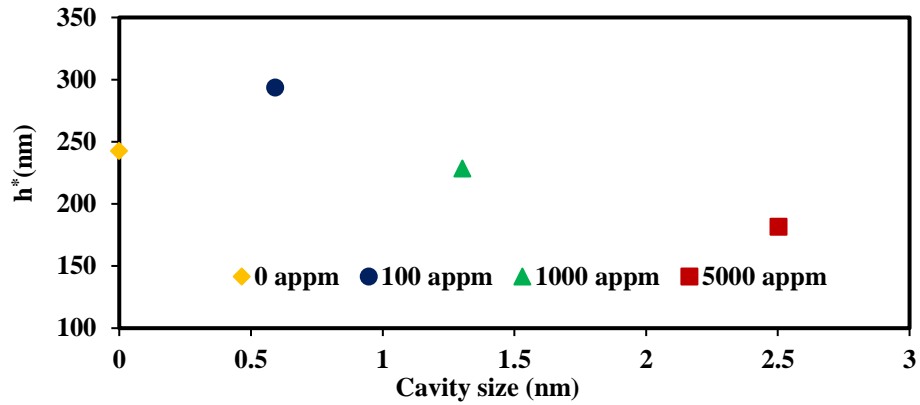
(a)



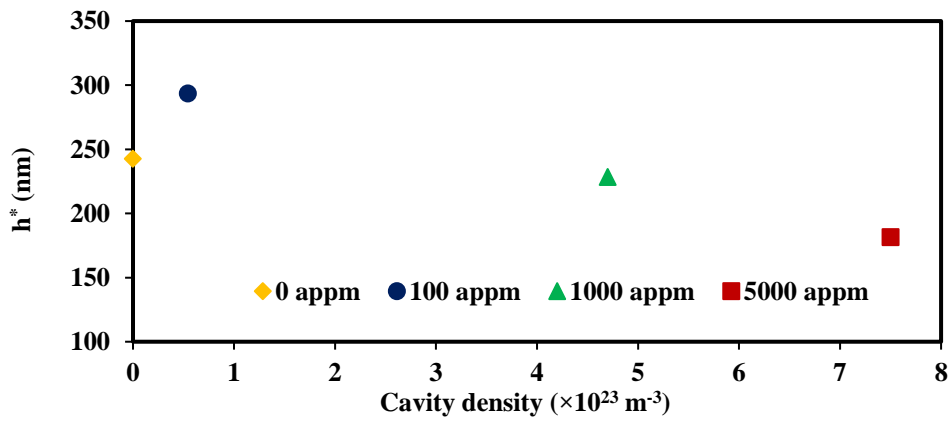
(b)



(c)



(d)



(e)

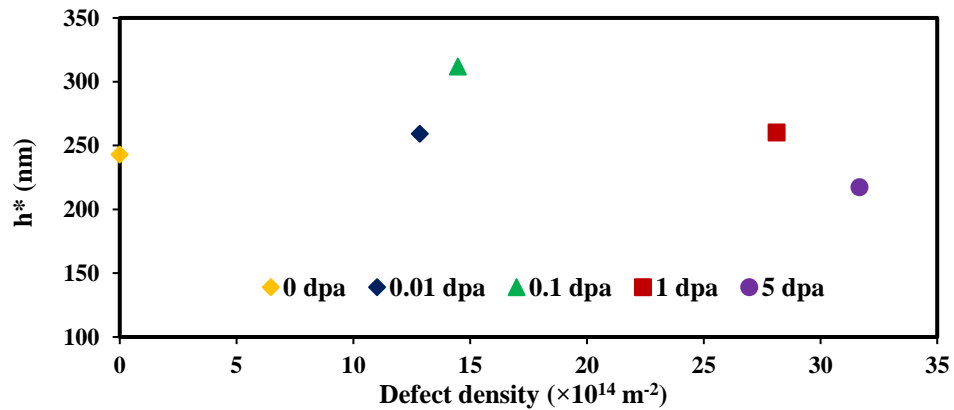


Figure 3.9: The characteristic indentation depth (h^*) reflecting the ISE of the measured hardness versus (a) C_{He} (appm) (b) ψ_{Ni} (dpa) (c) cavity size (d) cavity density (e) defect density.

Based on Nix and Gao model (Eq. 3.3) of the indentation size effect (ISE) prior plastic deformation and cold-work should decrease the ISE. Hosemann et al [20] argued that radiation damage will have a similar effect on ISE in a decreased characteristic depth h^* , as radiation-induced defects result in a higher density of existing SSDs after irradiation and therefore contribute to less pronounced ISE in the same manner as that of unirradiated cold-worked materials. A similar case was also observed in Cu nanopillars [38], Inconel X-750 [22] and He⁺ implanted steel [39]. The hardness data from our study indicate that in He⁺ implanted X-750 samples, the characteristic indentation depth h^* follows a decreasing trend with increasing accumulated helium from C_{He} = 100-5000 appm (Table 3-2, Figure 3.9-a). This could be attributed to the fact that accumulated helium resides as nano-bubbles within the microstructure and act as statistically stored obstacles to dislocation movement. This is further evident from (Figures 3.9 c-d) showing that there is a linear decrease in h^* with increases in both cavity size and density with increasing He⁺ implanted doses. However, Ni⁺ implantation displays increased h^* (Table 3-2, Figure 3.9-b). It is interesting to note that h^* increases rapidly with small increases in dpa and appears to reach a maximum at about 0.1 dpa. This corresponds to the level of irradiation damage that generates dislocation sources by introducing a high density of defects (Figure 3.9-e). However, after 0.1 dpa with increases in defect density there is a decreasing trend in h^* (Figure 3.9-e).

3.4 Conclusion

The influence of He⁺ and Ni⁺ implantation, at 300 °C and 25 °C on the nanoindentation hardness of the aged Ni-based Inconel X-750 alloy was investigated. Inconel X-750 exhibited a softening in hardness ($h = 400$ nm) caused by the radiation induced disordering and dissolution of the γ' precipitates from as received to $\psi_{Ni} = 0.01$ and 0.1 dpa (~6.8% and 10% reduction in grain by grain nano indentation hardness). High density of defects (i.e. dislocation loops, SFT) generated during irradiation and reformation of Al/Ti-rich regions (precipitates) are strong obstacles for subsequent dislocation movement resulting in higher hardness of about 5.1% increase in 1 dpa compared to 0.1 dpa. However, in $\psi_{Ni} = 5$ dpa γ' starts to dissolve into the matrix and saturation of defects occurs, so the hardness

values decreased. The ISE calculations according to NG model showed a linear trend for un-irradiated and irradiated materials. For irradiated materials this is attributed to the effect of irradiation-induced defects, which act as dislocation sources particularly for indents of smaller size when the deformation volume is smaller than 500 nm. Characteristic depth vs both cavity size and density decreased linearly with increasing helium concentrations. However, two main mechanism were responsible in deformation observed in Ni⁺ irradiated samples such that at lower doses (up to 0.1 dpa) gamma prime disordering/dissolution outweighed the increase in defect density resulting in higher h^* whereas at higher doses (beyond 0.1 dpa) increases in defect density was the main reason for lower h^* .

3.5 Acknowledgments

The authors wish to thank the Natural Science and Engineering Research Council of Canada (NSERC) and the University Network of Excellence in Nuclear Engineering (UNENE) who provided financial support for this research. The assistance of Mr. Jack Hendriks at the Tandatron Ion Accelerator facilities at the Western University (London, Ontario, Canada) for his support with performing ion implantations of the Inconel X-750 samples. The assistance of Dr. T. Simpson at Western University Nanofabrication Laboratory in preparing the SEM images is gratefully acknowledged. The authors wish to acknowledge the assistance of Mr. Ivan Barker at the Zircon and Accessory Phase Laboratory (ZAPLab) for EBSD data.

3.6 References

- [1] E. Schulson, The ordering and disordering of solid solutions under irradiation, *Journal of Nuclear Materials* 83(2) (1979) 239-264.
- [2] H.K. Zhang, Z. Yao, M.A. Kirk, M.R. Daymond, Stability of Ni₃(Al, Ti) gamma prime precipitates in a nickel-based superalloy inconel X-750 under heavy ion irradiation, *Metallurgical and Materials Transactions A* 45(8) (2014) 3422-3428.

- [3] M. Stopher, The effects of neutron radiation on nickel-based alloys, *Materials Science and Technology* 33(5) (2017) 518-536.
- [4] R. Nelson, J. Hudson, D. Mazey, The stability of precipitates in an irradiation environment, *Journal of Nuclear Materials* 44(3) (1972) 318-330.
- [5] E. Camus, C. Abromeit, F. Bourdeau, N. Wanderka, H. Wollenberger, Evolution of long-range order and composition for radiation-induced precipitate dissolution, *Physical Review B* 54(5) (1996) 3142.
- [6] H.K. Zhang, Z. Yao, G. Morin, M. Griffiths, TEM characterization of in-reactor neutron irradiated CANDU spacer material Inconel X-750, *Journal of Nuclear Materials* 451(1-3) (2014) 88-96.
- [7] M. Griffiths, The effect of irradiation on Ni-containing components in CANDU® reactor cores: a review, *Nuclear Review* 2(1) (2014) 1-16.
- [8] D.J. Edwards, F.A. Garner, S.M. Bruemmer, P. Efsing, Nano-cavities observed in a 316SS PWR flux thimble tube irradiated to 33 and 70 dpa, *Journal of nuclear materials* 384(3) (2009) 249-255.
- [9] C.D. Judge, N. Gauquelin, L. Walters, M. Wright, J.I. Cole, J. Madden, G.A. Botton, M. Griffiths, Intergranular fracture in irradiated Inconel X-750 containing very high concentrations of helium and hydrogen, *Journal of Nuclear Materials* 457 (2015) 165-172.
- [10] J. Knapp, D. Follstaedt, S. Myers, Hardening by bubbles in He-implanted Ni, *Journal of applied physics* 103(1) (2008) 013518.
- [11] H. Zhang, Z. Yao, M.R. Daymond, M.A. Kirk, Cavity morphology in a Ni based superalloy under heavy ion irradiation with hot pre-injected helium. II, *Journal of Applied Physics* 115(10) (2014) 103509.

- [12] H. Zhang, Z. Yao, M.R. Daymond, M.A. Kirk, Cavity morphology in a Ni based superalloy under heavy ion irradiation with cold pre-injected helium. I, *Journal of Applied Physics* 115(10) (2014) 103508.
- [13] M. Griffiths, G. Bickel, S. Donohue, P. Feenstra, C. Judge, D. Poff, L. Walters, M. Wright, L. Greenwood, F. Garner, Degradation of Ni-alloy components in CANDU® reactor cores, Atomic Energy of Canada Limited, 2013.
- [14] G. Was, Z. Jiao, E. Getto, K. Sun, A. Monterrosa, S. Maloy, O. Anderoglu, B. Sencer, M. Hackett, Emulation of reactor irradiation damage using ion beams, *Scripta Materialia* 88 (2014) 33-36.
- [15] H.K. Zhang, Z. Yao, C. Judge, M. Griffiths, Microstructural evolution of CANDU spacer material Inconel X-750 under in situ ion irradiation, *Journal of Nuclear Materials* 443(1-3) (2013) 49-58.
- [16] J.C. Lippold, S.D. Kiser, J.N. DuPont, *Welding metallurgy and weldability of nickel-base alloys*, John Wiley & Sons 2011.
- [17] J.F. Ziegler, M.D. Ziegler, J.P. Biersack, *SRIM—The stopping and range of ions in matter* (2010), *Nuclear Instruments and Methods in Physics Research Section B: Beam Interactions with Materials and Atoms* 268(11-12) (2010) 1818-1823.
- [18] F. Bachmann, R. Hielscher, H. Schaeben, Texture analysis with MTEX—free and open source software toolbox, *Solid State Phenomena*, Trans Tech Publ, 2010, pp. 63-68.
- [19] P. Hosemann, D. Kiener, Y. Wang, S.A. Maloy, Issues to consider using nano indentation on shallow ion beam irradiated materials, *Journal of Nuclear Materials* 425(1-3) (2012) 136-139.

- [20] P. Hosemann, C. Shin, D. Kiener, Small scale mechanical testing of irradiated materials, *Journal of Materials Research* 30(9) (2015) 1231.
- [21] A.C. Fischer-Cripps, Critical review of analysis and interpretation of nanoindentation test data, *Surface and coatings technology* 200(14-15) (2006) 4153-4165.
- [22] P. Changizian, C. Lu, Z. Yao, L. Wang, Indentation behaviour of ion-irradiated X-750 Ni-based superalloy, *Philosophical Magazine Letters* 97(3) (2017) 101-109.
- [23] M.N. Tawfeeq, R.J. Klassen, Ni⁺ and He⁺ Implantation Effects on the Hardness and Microstructure of Heat-Treated X750 Superalloy.
- [24] J. Hunn, E. Lee, T. Byun, L. Mansur, Ion-irradiation-induced hardening in Inconel 718, *Journal of nuclear materials* 296(1-3) (2001) 203-209.
- [25] H.K. Zhang, Z. Yao, M.R. Daymond, M.A. Kirk, Elevated temperature irradiation damage in CANDU spacer material Inconel X-750, *Journal of Nuclear Materials* 445(1-3) (2014) 227-234.
- [26] N. Hashimoto, J. Hunn, T. Byun, L. Mansur, Microstructural analysis of ion-irradiation-induced hardening in inconel 718, *Journal of nuclear materials* 318 (2003) 300-306.
- [27] C. Abromeit, S. Müller, N. Wanderka, Stability of γ' phase in the stoichiometric Ni 3 Al alloy under ion irradiation, *Scripta metallurgica et materialia* 32(10) (1995) 1519-1523.
- [28] F. Bourdeau, E. Camus, C. Abromeit, H. Wollenberger, Disordering and dissolution of γ' precipitates under ion irradiation, *Physical Review B* 50(22) (1994) 16205.
- [29] W.S. Cunningham, J.M. Gentile, O. El-Atwani, C.N. Taylor, M. Efe, S.A. Maloy, J.R. Trelewicz, Softening due to grain boundary cavity formation and its competition with

hardening in helium implanted nanocrystalline tungsten, *Scientific reports* 8(1) (2018) 1-10.

[30] W.D. Nix, H. Gao, Indentation size effects in crystalline materials: a law for strain gradient plasticity, *Journal of the Mechanics and Physics of Solids* 46(3) (1998) 411-425.

[31] G.M. Pharr, E.G. Herbert, Y. Gao, The indentation size effect: a critical examination of experimental observations and mechanistic interpretations, *Annual Review of Materials Research* 40 (2010) 271-292.

[32] K. Durst, B. Backes, M. Göken, Indentation size effect in metallic materials: Correcting for the size of the plastic zone, *Scripta Materialia* 52(11) (2005) 1093-1097.

[33] J. Swadener, E. George, G. Pharr, The correlation of the indentation size effect measured with indenters of various shapes, *Journal of the Mechanics and Physics of Solids* 50(4) (2002) 681-694.

[34] J. Swadener, A. Misra, R. Hoagland, M. Nastasi, A mechanistic description of combined hardening and size effects, *Scripta materialia* 47(5) (2002) 343-348.

[35] X.G. Qiao, M.J. Starink, N. Gao, The influence of indenter tip rounding on the indentation size effect, *Acta Materialia* 58(10) (2010) 3690-3700.

[36] Z. Shan, R.K. Mishra, S.S. Asif, O.L. Warren, A.M. Minor, Mechanical annealing and source-limited deformation in submicrometre-diameter Ni crystals, *Nature materials* 7(2) (2008) 115-119.

[37] D. Kiener, A.M. Minor, O. Anderoglu, Y. Wang, S.A. Maloy, P. Hosemann, Application of small-scale testing for investigation of ion-beam-irradiated materials, *Journal of Materials Research* 27(21) (2012) 2724.

[38] D. Kiener, P. Hosemann, S. Maloy, A. Minor, In situ nanocompression testing of irradiated copper, *Nature materials* 10(8) (2011) 608-613.

[39] Z. Fu, P. Liu, F. Wan, Q. Zhan, Helium and hydrogen irradiation induced hardening in CLAM steel, *Fusion Engineering and Design* 91 (2015) 73-78.

Chapter 4

4 Effect of high temperature He⁺ implantation on the kinetic deformation nanoindentation of Inconel X-750

In this study we have undertaken a characterization of the strength of helium implantation induced micro-cavities for impeding the plastic deformation during nano-indentation of age-hardened Inconel X-750. Nanoindentation tests were performed on Inconel X-750 samples of various levels of accumulated helium up to $C_{He} = 5000$ appm. The resulting indentation stress versus strain rate data of the deformation rate limiting obstacle were analyzed to determine the apparent activation strength ΔG_0 , activation volume V^* and activation characteristic area Δa of the indentation deformation process. A clearly increasing uptrend in the apparent activation strength of the obstacles was observed with increasing He⁺ doses up to $C_{He} = 5000$ appm. Furthermore, the apparent activation volume V^* decreases with increasing cavity size and density and indentation stress suggesting that the inter-obstacle spacing of obstacles to the glide of dislocations is decreasing and widely spaced when the stress and dislocation density are increased. At higher helium concentrations, the apparent activation area Δa is much smaller compared to the as-received sample. The resulting data on the effect of He⁺ implantation is particularly important for arriving at conservative predictions of the rate neutron-irradiation induced embrittlement of age-hardened Inconel X-750 annulus gas spacers in CANDU nuclear reactors.

4.1 Introduction

Helical spring annulus gas spacers in the fuel channels of current CANDU nuclear reactors are made from age-hardened Ni-based alloy Inconel X-750 [1-3]. Neutron irradiation is known to cause microstructural and mechanical property changes within these spacers, and this is an ongoing concern for the operation of these reactors. The microstructural degradation is in the form of radiation induced crystal damage and the accumulation of significant hydrogen and helium through nuclear transmutation processes [4]. In particular,

the $^{59}\text{Ni}(n,\alpha)^{56}\text{Fe}$ transmutation reaction results in helium accumulation rates in the order of about 300 appm/year in the Inconel X-750 spacers of a CANDU reactor [1, 5, 6].

The effect of neutron-induced crystal damage and helium accumulation on the microstructural and mechanical property degradation of Inconel X-750 annulus gas spacers has been, and continues to be, an active area of research. High energy ion irradiation techniques are now commonly used to simulate the microstructural effects of neutron irradiation without rendering the test material radioactive [7].

Knapp et al. demonstrated that He^+ implantation performed at room temperature on pure nickel, to concentrations of $C_{\text{He}} = 1 - 10$ at%, resulted in a fine dispersion of helium micro-cavities which acted as barriers to dislocation motion [8, 9]. Helium implantation, performed at 400 °C to concentrations of $C_{\text{He}} = 400$ to 5000 appm, in Inconel X-750 confirmed the existence of these internal micro-cavities and demonstrated that their mean size and density increased with increasing helium concentration [10]. Bending tests performed on bicrystalline cantilever micro-beams of He^+ implanted, $C_{\text{He}} = 5000$ appm, Inconel X-750 demonstrated that the implanted helium accumulated at grain boundaries resulting in enhanced grain boundary resistance to dislocation nucleation and transmission [11]. In summary, it is now well established that the accumulation of helium in the Inconel X-750 alloy results in the formation of small helium nano-cavities, the number and size of which increases with increasing C_{He} . The helium is quite mobile within the alloy and thus the cavities tend to accumulate at high angle grain boundaries. The cavities interact with crystal defects and thus represent obstacles to dislocation glide. At the moment however the strength of these obstacles, and how the strength varies with factors such as temperature and helium content, has not been quantified.

In this study we have undertaken a characterization of the obstacle strength of implanted helium micro-cavities in age hardened Inconel X-750. This was done by performing nanoindentation tests at various indentation strain rates to measure the strain rate dependence of the indentation stress and then applying established theories relating the strain rate dependence to deduce the apparent activation energy ΔG_0 , apparent activation

volume V^* and activation characteristic area Δa of the obstacles that limit the indentation strain rate.

4.2 Experimental procedure

4.2.1. Test material

The chemical composition of the Inconel X-750 alloy used in this study was given in Table 3-1 in chapter 3. The alloy was annealed at 1010 °C (30 min) followed by air cooling to room temperature, cold working by 18%, and then ageing at 728°C (16 h). The average grain size was found to be between 15 to 25 μm . Samples ($6 \times 6 \times 3$ mm) were cut from the aged material and surfaces were mechanically ground with successively finer grit SiC impregnated papers followed by polishing with an aqueous slurry of 0.02 μm colloidal SiO_2 . This process created a surface free of polishing-induced plastic deformation.

4.2.2 Ion implantation

The polished sample surfaces were then exposed to multiple He^+ ion irradiations at 300 °C at the Tandetron dual beam ion accelerator located at the University of Western Ontario. Fourteen sequential implantations were performed, at He^+ energy levels from 0.3 to 1.6 MeV, to establish a uniform level of implanted helium to a depth of about 3 μm into the sample (Figure 4.1). The duration of the implantations was controlled to achieve samples with $C_{\text{He}} = 100, 1000, \text{ and } 5000$ appm. The implanted helium concentration was determined with the SRIM (2013) software using the Kinchin–Pease approximation and threshold atom displacement energy of 40 eV [12]. It should be noted that high energy He^+ results in small amounts of ion-induced displacement of the substrate atoms. Our SRIM calculations indicate that the average level of displacements per substrate atom (dpa) were about 0.001, 0.01, and 0.05 dpa for the $C_{\text{He}} = 100, 1000, \text{ and } 5000$ appm implanted samples respectively.

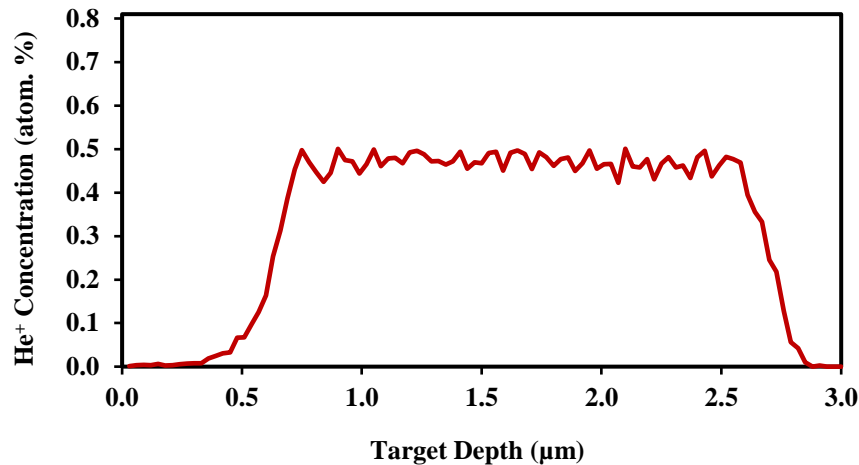


Figure 4.1: SRIM simulation for helium implantation, showing helium concentration as a function of target depth.

4.2.3 Nanoindentation testing

Nanoindentation tests were performed at 25 °C on the polished, ion-implanted, surfaces with a diamond Berkovich indenter on a Micro Materials NanoTest indentation testing platform [13, 14]. Indentation tests were performed at constant indentation loading rates of $\dot{P} = 0.3, 3.0$ and 30 mN/s to a maximum indentation depth of about $h_{max} = 1400$ nm. The resulting indentation force – depth, $P-h$, responses were recorded. Three indentation tests were performed at each value of \dot{P} and each level of C_{He} . Twenty-seven indentation tests were performed in total.

4.3 Results

4.3.1 Calculation of projected area function of indentation

All Berkovich indenters, including the one used in this study, have a certain amount of rounding at the indenter tip. The profile of the pyramidal indenter used in this study was imaged with SEM, and the radius R of the rounded tip was found to be 250.8 nm (Figure 4.2).

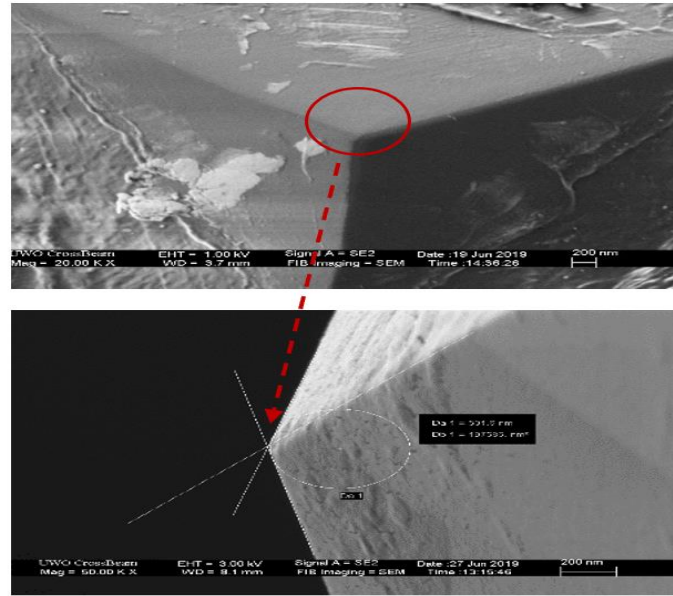


Figure 4.2: Images (SEM) of Berkovich indenter that was used in present study: radius of indenter tip is 250.8 nm.

The minimum indentation depth for geometrically self-similar deformation in this experimental study was estimated to be $h_{min} = 15 \text{ nm}$ by using the previously reported equation [15-18]

$$h_{min} = R(1 - \sin 70.3^\circ) = 0.06R \quad (4.1)$$

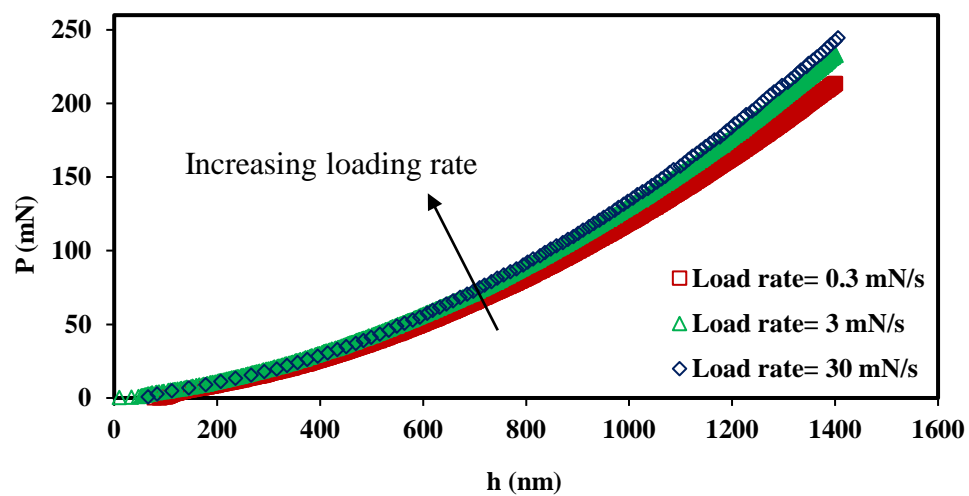
The projected indentation contact area was calculated as [17, 19, 20]:

$$A(h) = 24.56(h + 0.06R)^2 \quad (4.2)$$

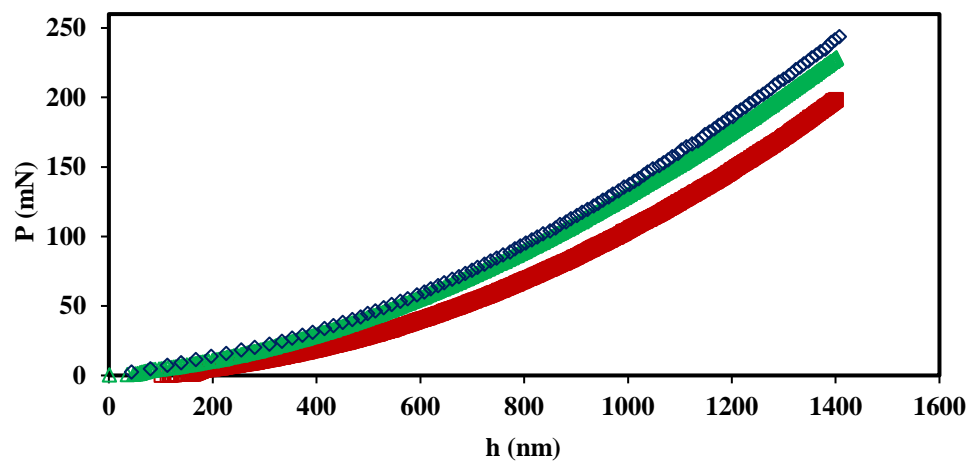
4.3.2 Indentation force -depth ($P-h$) plots

Figure 4.3 shows plots of the average indentation force P versus indentation depth h for representative tests performed on the Inconel X-750 samples at the various levels of \dot{P} and C_{He} . The magnitude of P at the maximum indentation depth of 1400 nm is clearly larger for the heavily implanted, $C_{He} = 5000 \text{ appm}$, condition than the other conditions. This indicates the effect of accumulated helium on increasing the flow stress of this alloy. At any given indentation depth, P increases with increasing loading rate indicating the strain rate sensitivity of the indentation stress.

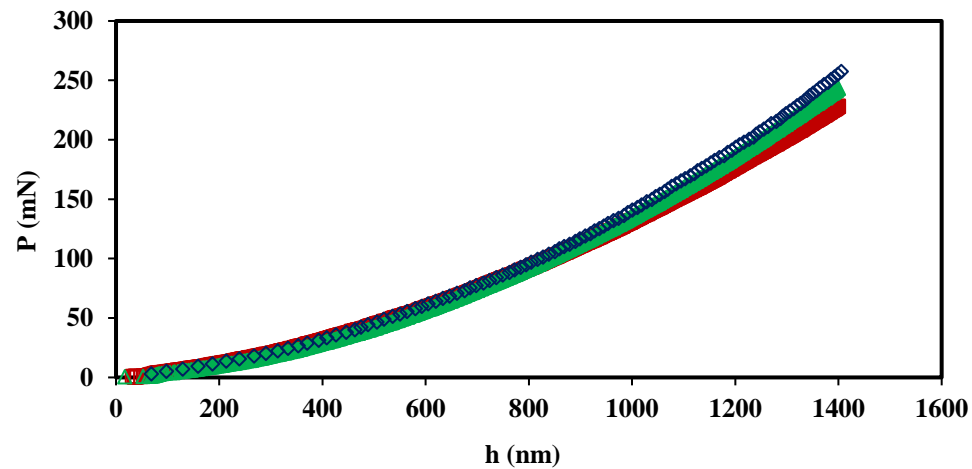
(a)



(b)



(c)



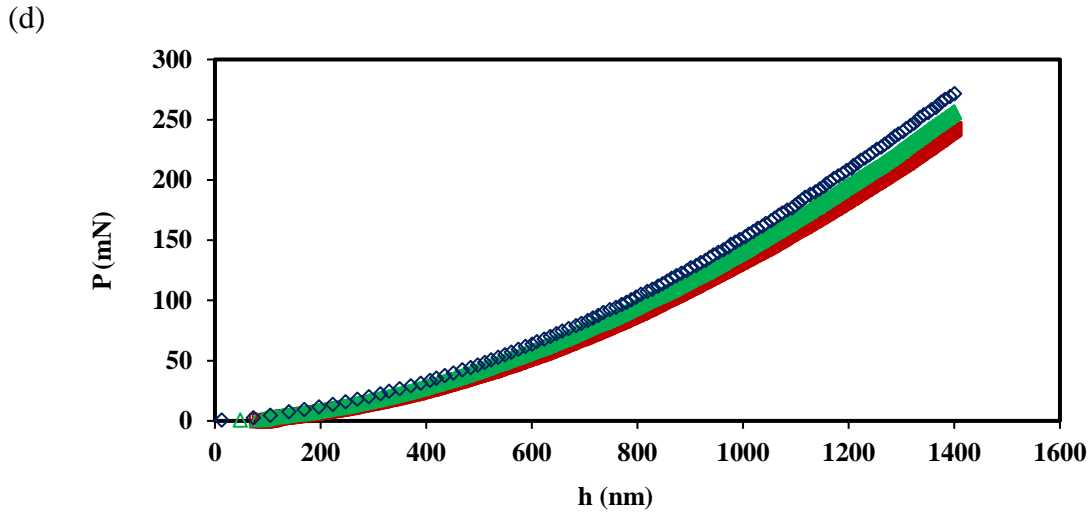


Figure 4.3: Representative indentation force P versus depth h curves for the tested Inconel X-750 alloy subjected to various levels of implanted helium concentration: (a) $C_{He} = 0$ (b) $C_{He} = 100$ appm (c) $C_{He} = 1000$ appm (d) $C_{He} = 5000$ appm.

4.3.3 Indentation stress σ_{ind} versus indentation depth, h

The average indentation stress was calculated from the load, P , and depth, h , data as [21-23]

$$\sigma_{ind} = \frac{P}{CA(h)} = \frac{P}{24.56C(h+0.06R)^2} \quad (4.3)$$

where $R = 250.8$ nm is the radius of the indenter tip and C is a metal sink-in/pile-up factor. For geometrically self-similar indentations performed on mechanically isotropic material C will be independent of indentation depth [24]. The actual contact area of the indentation was calculated from equation (4.2) and compared with the ideal projected area, $A_{ideal} = 24.56h^2$, of a perfect Berkovich indentation. The parameter C is then [24-26]:

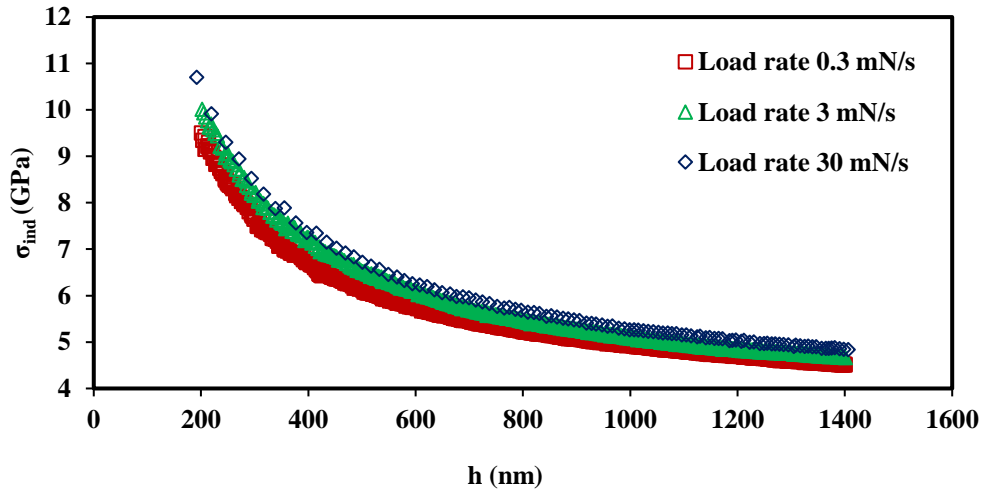
$$C = \frac{A_{actual}}{A_{ideal}} \quad (4.4)$$

In our study $C = 1.023$.

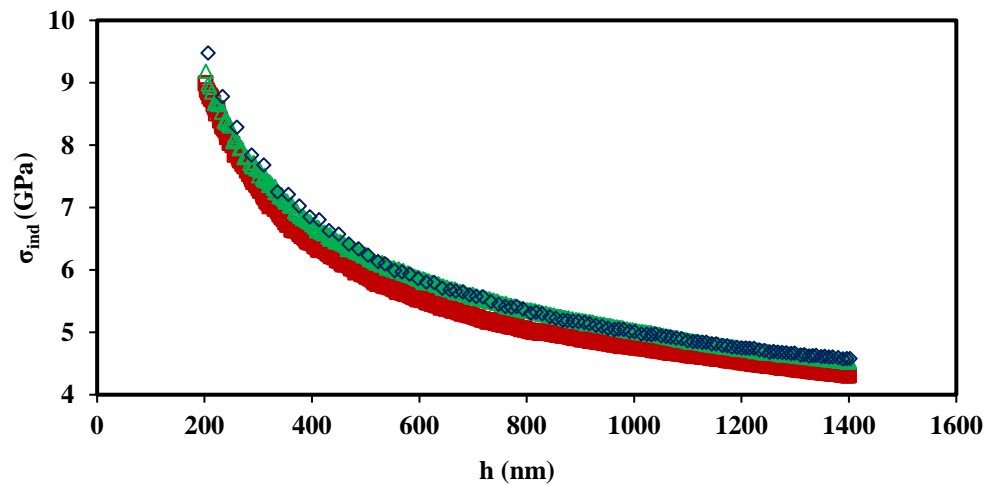
It should be noted that the parameter C is also dependent upon the plastic deformation behavior of indented material. Thus, C may change with ion implantation. In our study

however, we assume that $C = 1.023$ for all our indented materials. It should be noted that σ_{ind} Eq. (4.3) differs from the commonly reported indentation hardness since it is calculated with the use of the total indentation depth h , which includes both the elastic and the plastic indentation depth, whereas conventional indentation hardness is calculated with only the residual plastic indentation depth. We observe that for all the materials tested, for any given indentation depth, σ_{ind} increases with increased loading rate. Also, σ_{ind} increases significantly when h is small and reflects the commonly observed indentation size effect (Figure 4.4).

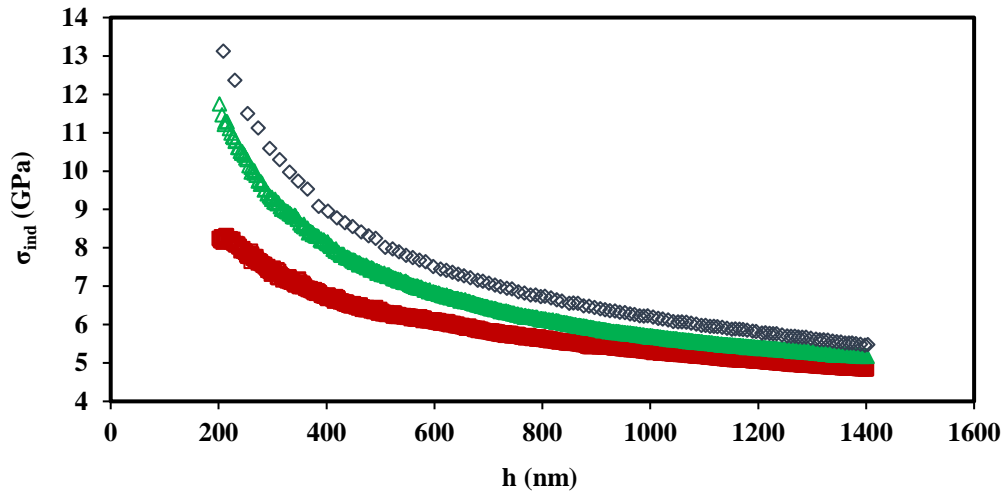
(a)



(b)



(c)



(d)

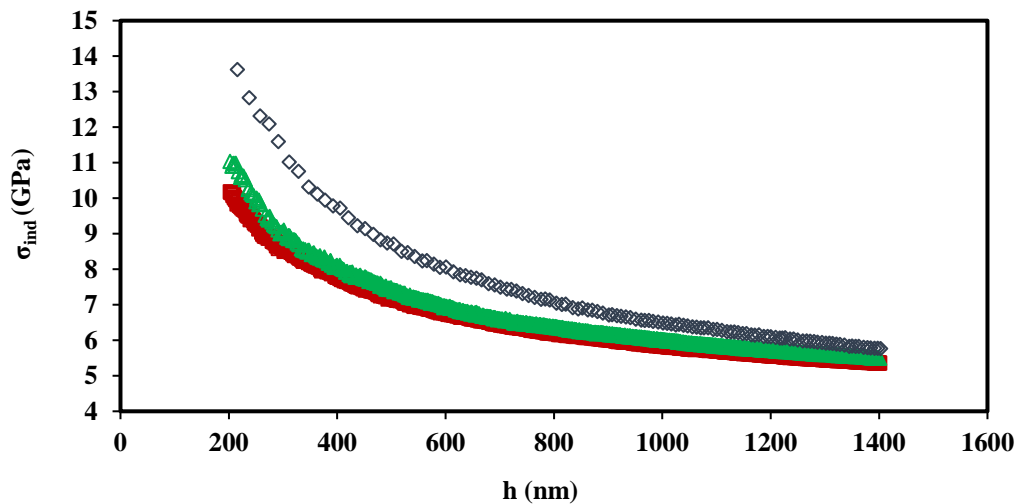


Figure 4.4: Average indentation stress σ_{ind} versus indentation depth h for the tested Inconel X-750 alloy subjected to various levels of implanted helium concentration: (a) $C_{He} = 0$ (b) $C_{He} = 100$ appm (c) $C_{He} = 1000$ appm (d) $C_{He} = 5000$ appm.

4.3.4 Microstructure evaluation

In order to investigate the relationship between kinetic deformation parameters (V^* and Δa) determined in this study and the irradiation effect of He^+ on cavity size and density, previously published data from Zhang et al. [10, 27] were adapted. These data included

microstructural changes examined from TEM results after hot preinjected He⁺ at 400 °C ($C_{He} = 400, 1000$ and 5000 appm) on Inconel X-750. In order to derive equivalent microstructural changes for the doses used in the current study, the original data were replotted and fitted with the best fit curve (polynomial second order) and equivalent microstructural values were calculated from the equation derived (Figure 4.7-a,b) Zhang et al. [10] showed that there was a strong linear correlation between high temperature implanted He⁺ doses and both cavity size and density. Therefore, in this study we chose to show the most affected microstructural changes with He⁺ implantation doses meaning both cavity size and density.

4.4 Discussion

4.4.1 Obstacle-limited thermally-activated dislocation glide

The plastic shear strain rate $\dot{\gamma}$ that results in a single crystal when subjected to a constant applied shear stress τ can be expressed [23, 26, 28] as:

$$\dot{\gamma} = \dot{\gamma}_P \left(\frac{\tau_{ind}}{\mu} \right)^2 e^{-\frac{\Delta G_{Thermal}(\tau_{equiv})}{kT}} \quad (4.5)$$

where $\Delta G_{Thermal}(\tau_{equiv})$ is the stress dependent thermal activation energy required for a dislocation to overcome the rate limiting obstacles present within the microstructure. The term $\left(\frac{\tau_{ind}}{\mu} \right)^2$ is proportional to the dislocation density and the pre-exponent term $\dot{\gamma}_P$ is a constant function taken to be ($\approx 10^{11} \text{ sec}^{-1}$) [28].

4.4.2 Mechanism of indentation deformation

The experimental results shown in Figure 4 indicate that the indentation stress is a function of both indentation depth and indentation strain rate. Both dependencies reflect the nature of the dislocation – obstacle configuration at the various indentation depths in the helium implanted Inconel X-750. This dependence may arise from increased difficulty for

dislocation movement through He⁺induced crystal defects within the indentation plastic zone or the increased difficulty to nucleate a dislocation in the region of a shallow, compared to a deep, indentation. We can express the time dependent deformation during indentation as an obstacle limited dislocation glide process. We modified Eq. (4.5), which expressed shear strain rate as a function of stress for deformation by the mechanism of obstacle-limited dislocation glide in a single crystal subjected to simple shear stress to pertain to multiaxial nanoindentation. We use the Tabor equation relating the uniaxial normal yield stress of a metal to approximately one third the indentation stress [29]:

$$\sigma_{equiv} \approx \frac{\sigma_{ind}}{3} \quad (4.6)$$

We then convert this normal stress to an equivalent shear stress by applying the Taylor factor typical of FCC metals, namely $M = 3.06$ [28]

$$\tau_{equiv} = \frac{\sigma}{M} = \frac{\sigma_{ind}}{3(3.06)} = 0.109\sigma_{ind} \quad (4.7)$$

During pyramidal indentation the average indentation strain rate is directly proportional to the ratio \dot{h}/h . We therefore express an ‘apparent’ average indentation strain rate as:

$$\dot{\epsilon}_{ind} = \frac{1}{h} \left(\frac{dh}{dt} \right) \quad (4.8)$$

Similarly, the equivalent shear strain rate becomes:

$$\dot{\gamma}_{equiv} = \frac{\dot{\epsilon}_{ind}}{M} = \frac{0.327}{h} \left(\frac{dh}{dt} \right) \quad (4.9)$$

This allows us then to apply Eqs. (4.5, 4.7 and 4.9) as:

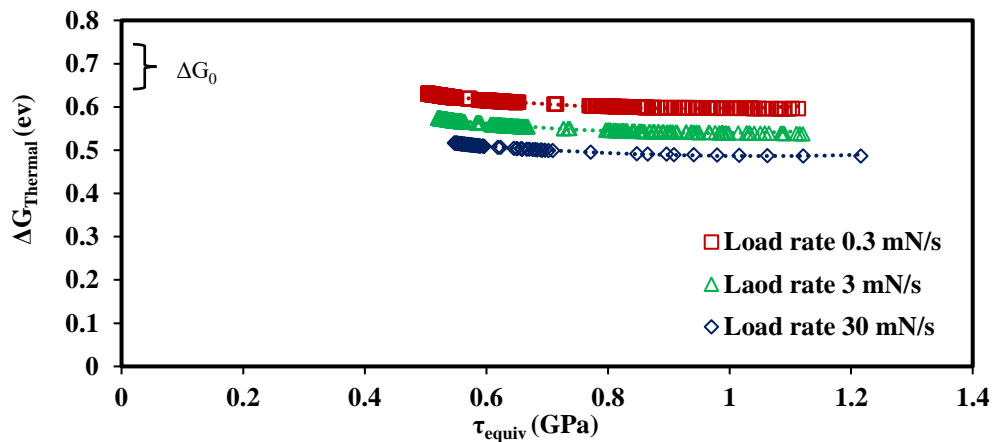
$$\dot{\gamma}_{equiv} = \frac{0.327}{h} \left(\frac{dh}{dt} \right) = \dot{\gamma}_P \left(\frac{\tau_{ind}}{\mu} \right)^2 e^{-\frac{\Delta G_{Thermal}(\tau_{equiv})}{kT}} \quad (4.10)$$

Rearranging terms in this equation allows us to express $\Delta G_{Thermal}(\tau_{ind})$ in terms of the experimentally obtained τ_{equiv} and $\dot{\gamma}_{equiv}$ as:

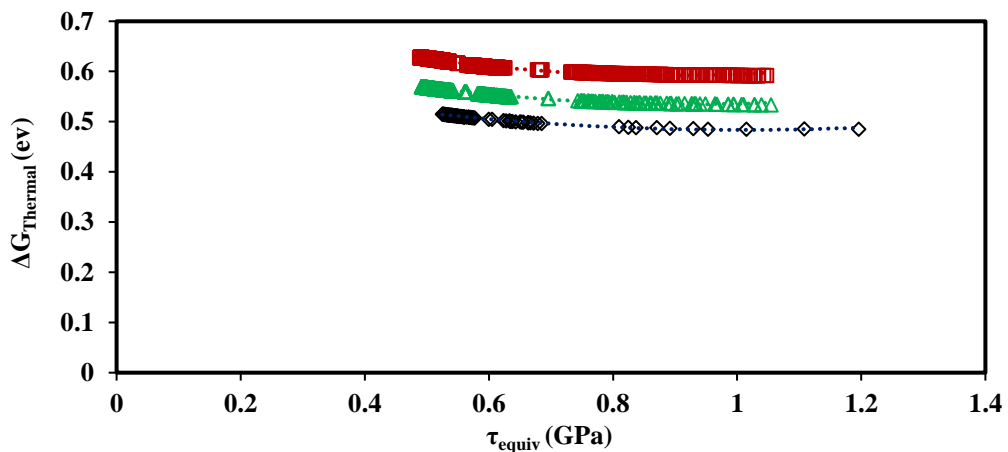
$$\Delta G_{Thermal}(\tau_{equiv}) = -kT \ln \left(\frac{\dot{\gamma}_{equiv}}{\dot{\gamma}_P \left(\frac{\tau_{ind}}{\mu} \right)^2} \right) \quad (4.11)$$

Figure 4.5 shows $\Delta G_{Thermal}(\tau_{equiv})$ plotted versus τ_{equiv} for all the C_{He} conditions in the different loading rates studied. The fact that the dependence of $\Delta G_{Thermal}(\tau_{equiv})$ upon τ_{equiv} is dependent upon both h and C_{He} and indicates that the strength of the obstacles change with both parameters as $\Delta G_{Thermal}(\tau_{equiv})$ decreases with increasing τ_{equiv} . There is an obvious increase of obstacle size and density with the increasing helium dosages. It has been shown that small (< 5nm) dislocation as well as a low-density large dislocation loops up to 20 nm in diameter are present after 1000 appm helium implantation [10].

(a)



(b)



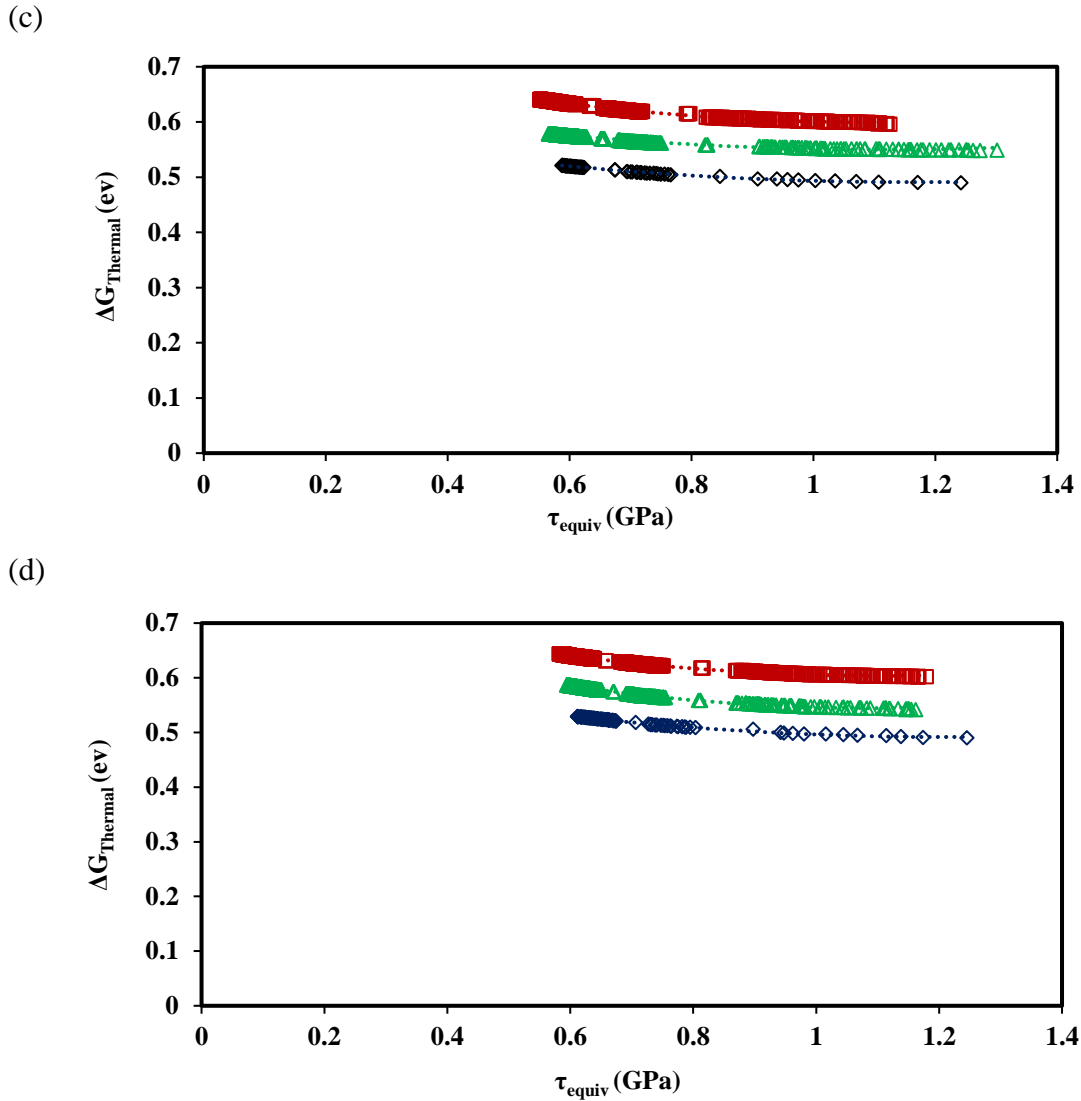


Figure 4.5: Plots of activation energy $\Delta G_{Thermal}$ versus τ_{equ} for (a) $C_{He} = 0$ (b) $C_{He} = 100$ appm (c) $C_{He} = 1000$ appm (d) $C_{He} = 5000$ appm.

4.4.3 Apparent activation strength and activation volume

It is common to express $\Delta G_{Thermal}(\tau_{equiv})$ in terms of a linear function of applied stress as:

$$\Delta G_{Thermal}(\tau_{equiv}) = \Delta G_0 - V^* \tau_{equiv} \quad (4.12)$$

Where ΔG_0 and V^* represent the characteristic activation energy and activation volume of the obstacles that limit the deformation process. These parameters describe the effectiveness of the microstructural obstacles at influencing the plastic deformation properties of the material. In this study we present the results of an investigation into the effect of accumulated helium, implanted at 300 °C, on the nano-indentation stress of age hardened Inconel X-750. Variations of Eqs. (4.11,4.12) are then applied to these data to deduce the effect of accumulate helium on the characteristic obstacle strength, as indicated by the parameters ΔG_0 and V^* . However, in this study we assumed that the average microstructure in the deforming region during indentation remains constant at a given indentation depth regardless of the magnitude of the loading rate.

We have used Eqs. (4.11, 4.12) to analyze the ΔG_0 and V^* for indentation tests performed on He^+ implanted samples in $C_{\text{He}} = 100, 1000, 5000$ appm and as received sample from 200 to 1400 nm depth. By extrapolating the data trends of $\Delta G_{\text{Thermal}}(\tau_{\text{equiv}})$ versus τ_{equiv} in Figure 4.5 we can define $\Delta G_{\text{Thermal}}(\tau_{\text{equiv}})$ occurring at a very low $\tau_{\text{equiv}} \sim 0$ as the activation energy ΔG_0 of the obstacles that are limiting the dislocation nucleation– glide process.

Figure 4.6 shows the resulting ΔG_0 versus He^+ concentration with a clear linear uptrend showing that the activation strength ΔG_0 of the deformation rate are controlled by a gradual increase in obstacles size and density with increasing C_{He} as it is shown in Figure 4.7-a,b. As cavities and implantation defects are increased when $C_{\text{He}} = 5000$ appm, ΔG_0 is increased by $\sim 4\%$ compared with that of as-received sample (0.74 to 0.78 eV).

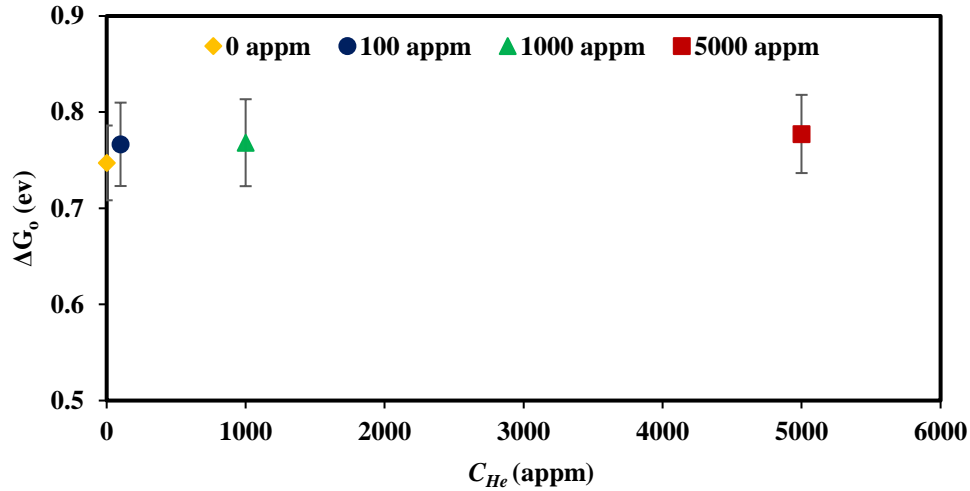


Figure 4.6: Apparent activation strength ΔG_0 of obstacles that limit dislocations glide versus helium concentration C_{He} (appm).

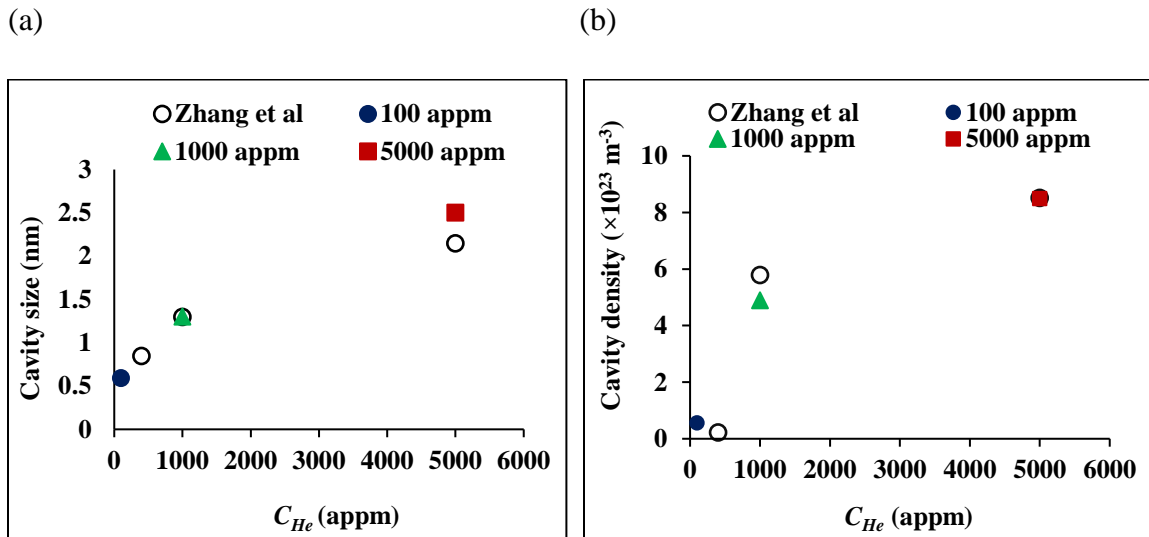


Figure 4.7: (a) Cavity size (nm) (b) density versus C_{He} (appm). Cavity size and density data are determined from [10].

We have used Eq. (4.12) to analyze the $\Delta G_{Thermal}(\tau_{equiv})$ versus h data obtained from our experiments and, in doing so, calculated values of ΔG_0 and V^* for indentation tests performed on the as-received and He^+ implanted samples, between 200-400, 600-800, and 1000-1400 nm depths. Figure 4.8 shows a plot of the calculated apparent activation volume V^* , normalized with respect to the Burgers vector cubed ($b_{Ni} = 0.249 \text{ nm}$ [28]), versus indentation depth for data from the indentation tests performed at the lowest loading rate, $\dot{P} = 0.3 \text{ mN}\cdot\text{s}^{-1}$. The data indicate that V^* increases with increasing indentation depth and

the dependence of V^* upon indentation depth is in agreement with the findings from displacement rate change indentation tests with findings from indentation tests performed on FCC and BCC metals [30-32].

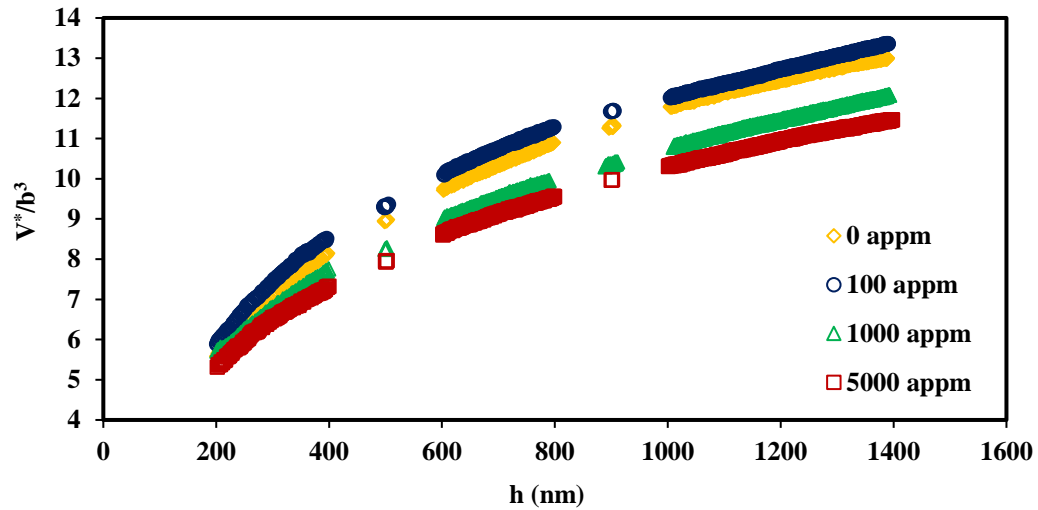


Figure 4.8: Normalized activation volume, V^*/b^3 , versus indentation depth for tests performed at $\dot{P} = 0.3$ mN/s for different helium concentrations.

As shown in (Figure 4.9 a-b), at $C_{He} = 100$ appm, V^* is higher ($\sim 8.5 b^3$) than the $C_{He} = 1000$ ($\sim 7.7 b^3$) and 5000 appm ($\sim 7.3 b^3$) samples. It is observed that as C_{He} increases from 100 to 5000 appm there is an increase in the formation of obstacles (cavities) and densities [10] which would resist the dislocation glide (Figure 4.7 a- b).

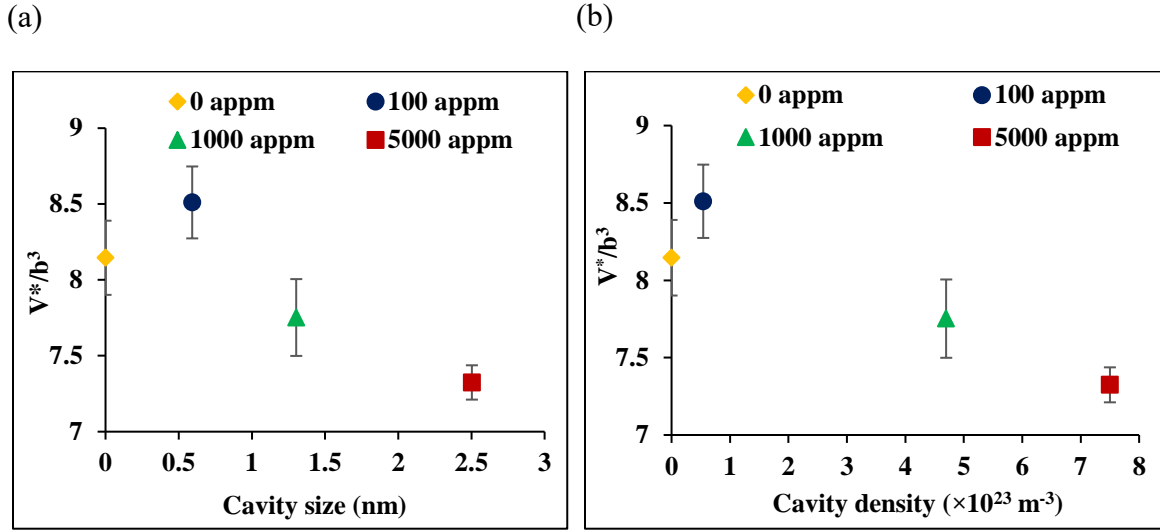


Figure 4.9: (a) Normalized activation volume, V^*/b^3 , at $\dot{P} = 0.3 \text{ mN/s}$ for different helium concentrations versus cavity size (nm) (b) and as cavity density as data are determined from [10].

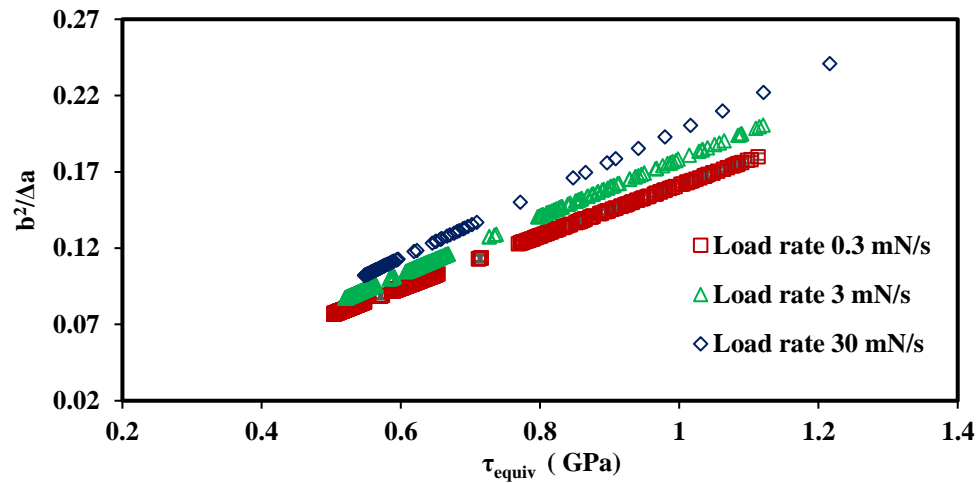
Also, when comparing as-received sample with 100 appm, it appears that 100 appm is the lowest helium dose that can impair the ductility of Inconel X-750 due to the formation of very small and widely spaced nanocavities [10]. This finding is significant for predicting the effect of helium accumulation rate on ductility of X-750 components in nuclear reactor as it would imply that ductility may already be impaired within the first few years of reactor operation.

4.4.4 Haasen plot activation analysis

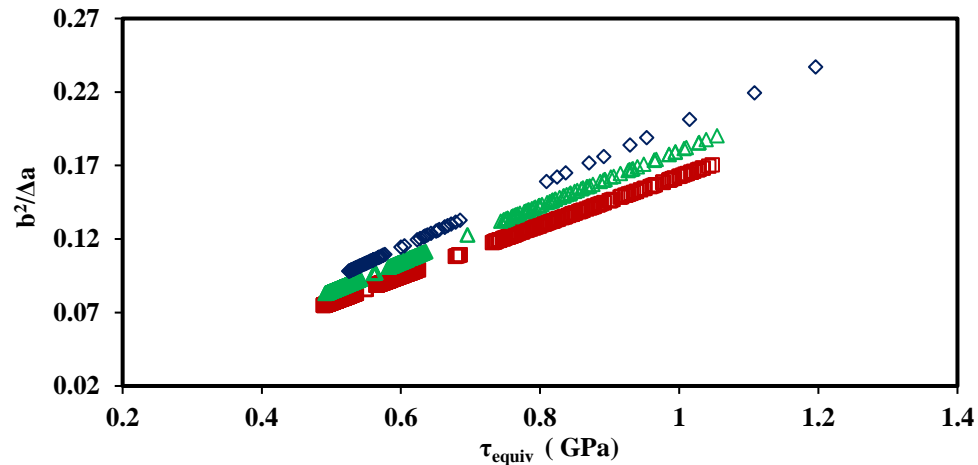
The data presented above indicate that when indentation is performed with a geometrically self-similar indenter under conditions of constant loading rate the resulting values of ΔG_0 and V^* are dependent upon both indentation depth and the level of prior plastic deformation of He^+ implanted samples. To assess these dependencies further we depict the data from our indentation tests on Haasen plots of inverse activation area, $1/\Delta\alpha$, versus applied equivalent indentation shear stress, τ_{equiv} [33, 34]. Activation area is the area which is covered by dislocation as overcome the obstacles. This type of plot is often referred to as a ‘‘Haasen Plot’’ and is used to identify the type of obstacles that control plastic deformation

when subjected to an τ_{equiv} . A Hassen plot that intersects the $1/\Delta a$ vertical axis indicates that the obstacles controlling deformation process are rate sensitive “thermal obstacles”. Previous analyses have shown that linear dependence of $1/\Delta a$ with τ_{equiv} results from plastic deformation that occurs by a mechanism of dislocation glide that is limited by dislocation–dislocation interactions [33, 35]. The slope of this linear trend is inversely proportional to the mechanical activation work ΔW of the obstacles that limits the rate of dislocation glide [34]. Figure 4.10 shows plots of $b^2/\Delta a$ versus τ_{equiv} for the indentation tests performed on the He⁺ implanted and as received samples of Inconel X-750 between different indentation depths from 200 to 1400 nm for different loading rates. The data show essentially linear trends with the slope which is decreasing with increasing τ_{equiv} .

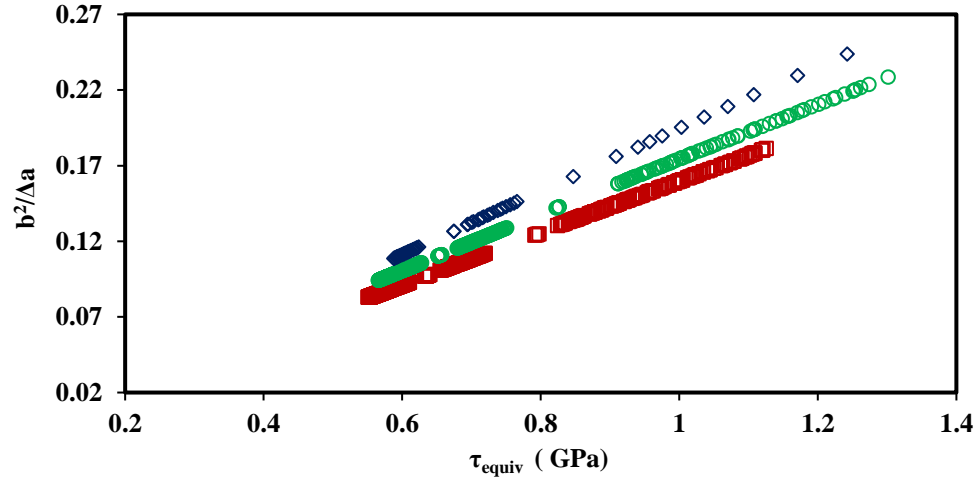
(a)



(b)



(c)



(d)

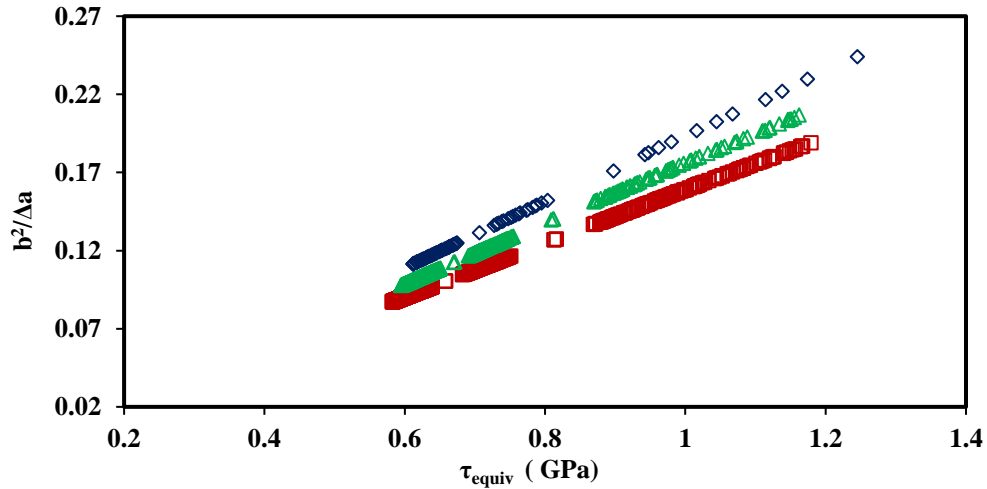


Figure 4.10: $b^2/\Delta a$ versus τ_{equiv} for the indentation test performed on (a) $C_{He} = 0$ (b) $C_{He} = 100$ appm (c) $C_{He} = 1000$ appm (d) $C_{He} = 5000$ appm.

The plot of $b^2/\Delta a$ in different levels of implanted He^+ at $C_{He} = 100, 1000, 5000$ appm versus equivalent shear stress (τ_{equiv}) is shown in Figure 4.11. When the Hassen plot intersects the $b^2/\Delta a$ vertical axis, that indicates that the thermal obstacles (solute atoms) are controlling the deformation process. In addition, Figure 4.12 indicates that the apparent activation area Δa is much smaller for the high helium content $C_{He} = 5000$ appm material compared to the as-received samples and, as a result, Δa decreased 11% due to the higher He^+ induced micro-cavities.

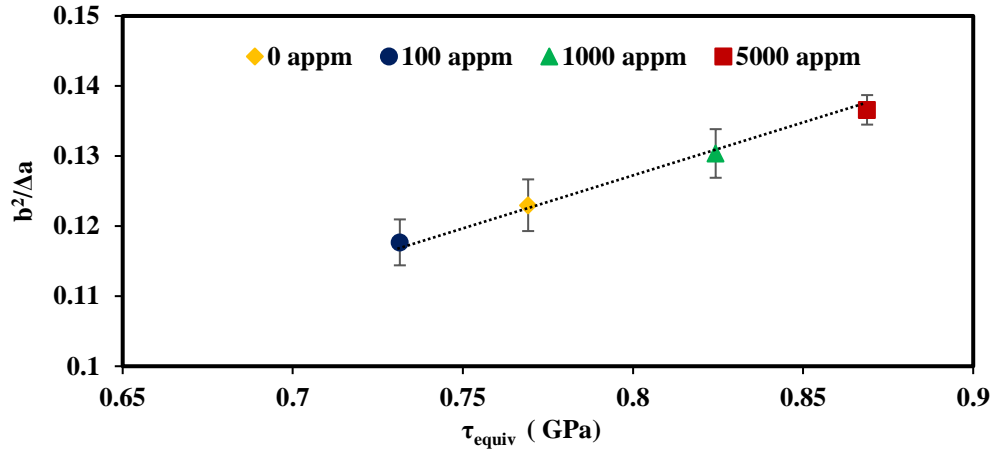


Figure 4.11: $b^2/\Delta a$ versus τ_{equiv} at 400 nm depth for different He⁺ implanted and as received samples.

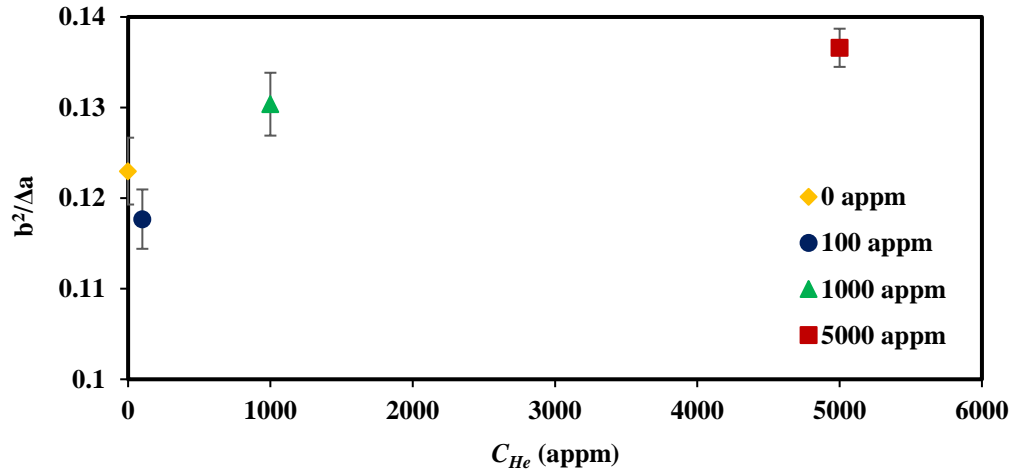


Figure 4.12: $b^2/\Delta a$ versus He⁺ concentration (appm) and as-received samples at 400 nm depth.

4.5 Conclusion

Indentation stress σ_{ind} is increased with decreasing indentation depth and increasing levels of He⁺ ion implantation. The depth dependence of the indentation stress is consistent with that predicted by the theories that attribute this to the increased density of geometrically necessary dislocations around sub-nanometer indentations. In addition, thermal activation energy $\Delta G_{Thermal}$ of the obstacles that either interfere with the glide of existing dislocations or represent sites for the nucleation of new dislocations was calculated and

found to decrease by increasing τ_{equiv} . Consistently, there was a clear increasing uptrend in strength of the obstacles (ΔG_0) with increasing He^+ dose up to $C_{He} = 5000$ appm. This is in line with microstructure changes showing that both cavity size and density is similarly increased by increasing He^+ doses. This demonstrates that the rate of dislocation glide is being limited during indentation from the measured indentation stress and strain rates. Furthermore, activation volume V^* decreases with increasing indentation stress suggesting that the inter-obstacle spacing of obstacles to the glide of dislocations is decreasing when the stress and dislocation density is increased. We observe also that at higher helium concentrations, the apparent activation area, Δa is much smaller compared to as-received sample. In addition, both cavity size and density showed an inverse relationship with activation volume V^* further confirming an increasingly smaller apparent activation area, Δa was associated with increasing He^+ doses. The resulting data on the effect of He^+ implantation on σ_{ind} and ΔG_0 are particularly important for arriving at conservative predictions of the rate neutron-irradiation induced embrittlement of age-hardened Inconel X-750 annulus gas spacers in CANDU nuclear reactors.

4.6 Acknowledgements

The authors wish to thank the Natural Science and Engineering Research Council of Canada (NSERC) and the University Network of Excellence in Nuclear Engineering (UNENE) who provided financial support for this research. The assistance of Mr. Jack Hendriks at the Tandetron Ion Accelerator facilities at the University of Western Ontario (London, Ontario, Canada) for his support with performing ion implantations of the Inconel X-750 samples. The assistance of Dr. T. Simpson of the University of Western Ontario Nanofabrication Laboratory in preparing the SEM images is gratefully acknowledged.

4.7 References

- [1] M. Griffiths, The effect of irradiation on Ni-containing components in CANDU® reactor cores: a review, Nuclear Review 2(1) (2014) 1-16.

- [2] J. Del Valle, A. Picasso, I. Alvarez, R. Romero, Age-hardening behavior of Inconel X-750 superalloy, *Scripta materialia* 41(3) (1999) 237-243.
- [3] W. Mills, Effect of temperature on the fracture toughness behavior of Inconel X-750, *Fractography and Materials Science*, ASTM International 1981.
- [4] C.D. Judge, N. Gauquelin, L. Walters, M. Wright, J.I. Cole, J. Madden, G.A. Botton, M. Griffiths, Intergranular fracture in irradiated Inconel X-750 containing very high concentrations of helium and hydrogen, *Journal of Nuclear Materials* 457 (2015) 165-172.
- [5] L. Wang, S. Zinkle, R. Dodd, G. Kulcinski, Effects of preinjected helium in heavy-ion irradiated nickel and nickel-copper alloys, *Metallurgical Transactions A* 21(7) (1990) 1847-1851.
- [6] M. Griffiths, G. Bickel, S. Donohue, P. Feenstra, C. Judge, D. Poff, L. Walters, M. Wright, L. Greenwood, F. Garner, Degradation of Ni-alloy components in CANDU® reactor cores, Atomic Energy of Canada Limited, 2013.
- [7] G. Was, Z. Jiao, E. Getto, K. Sun, A. Monterrosa, S. Maloy, O. Anderoglu, B. Sencer, M. Hackett, Emulation of reactor irradiation damage using ion beams, *Scripta Materialia* 88 (2014) 33-36.
- [8] J. Knapp, D. Follstaedt, S. Myers, Hardening by bubbles in He-implanted Ni, *Journal of applied physics* 103(1) (2008) 013518.
- [9] S.-H. Li, J. Zhang, W.-Z. Han, Helium bubbles enhance strength and ductility in small-volume Al-4Cu alloys, *Scripta Materialia* 165 (2019) 112-116.
- [10] H. Zhang, Z. Yao, M.R. Daymond, M.A. Kirk, Cavity morphology in a Ni based superalloy under heavy ion irradiation with hot pre-injected helium. II, *Journal of Applied Physics* 115(10) (2014) 103509.

- [11] M.N. Tawfeeq, R.J. Klassen, Effect of ion implantation on the grain boundary strength of heat treated Inconel X750, *Journal of Nuclear Materials* 516 (2019) 255-263.
- [12] J.F. Ziegler, M.D. Ziegler, J.P. Biersack, SRIM—The stopping and range of ions in matter (2010), *Nuclear Instruments and Methods in Physics Research Section B: Beam Interactions with Materials and Atoms* 268(11-12) (2010) 1818-1823.
- [13] J. Smith, S. Zheng, High temperature nanoscale mechanical property measurements, *Surface Engineering* 16(2) (2000) 143-146.
- [14] B.D. Beake, J.F. Smith, High-temperature nanoindentation testing of fused silica and other materials, *Philosophical Magazine A* 82(10) (2002) 2179-2186.
- [15] A.C. Fischer-Cripps, The sharpness of a Berkovich indenter, *Journal of Materials Research* 25(5) (2010) 927-934.
- [16] A.C. Fischer-Cripps, Critical review of analysis and interpretation of nanoindentation test data, *Surface and coatings technology* 200(14-15) (2006) 4153-4165.
- [17] J. Gong, H. Miao, Z. Peng, On the contact area for nanoindentation tests with Berkovich indenter: case study on soda-lime glass, *Materials letters* 58(7-8) (2004) 1349-1353.
- [18] M. Haghshenas, L. Wang, R. Klassen, Depth dependence and strain rate sensitivity of indentation stress of 6061 aluminium alloy, *Materials Science and Technology* 28(9-10) (2012) 1135-1140.
- [19] M.R. VanLandingham, T. Juliano, M. Hagon, Measuring tip shape for instrumented indentation using atomic force microscopy, *Measurement Science and Technology* 16(11) (2005) 2173.

- [20] X.G. Qiao, M.J. Starink, N. Gao, The influence of indenter tip rounding on the indentation size effect, *Acta Materialia* 58(10) (2010) 3690-3700.
- [21] M. Haghshenas, R. Klassen, Assessment of the depth dependence of the indentation stress during constant strain rate nanoindentation of 70/30 brass, *Materials Science and Engineering: A* 572 (2013) 91-97.
- [22] V. Bhakhri, R. Klassen, The depth dependence of the indentation creep of polycrystalline gold at 300 K, *Scripta materialia* 55(4) (2006) 395-398.
- [23] M. Haghshenas, R. Klassen, Indentation-based assessment of the dependence of geometrically necessary dislocations upon depth and strain rate in FCC materials, *Materials Science and Engineering: A* 586 (2013) 223-230.
- [24] K. McElhaney, J.J. Vlassak, W.D. Nix, Determination of indenter tip geometry and indentation contact area for depth-sensing indentation experiments, *Journal of Materials research* 13(5) (1998) 1300-1306.
- [25] W.C. Oliver, G.M. Pharr, An improved technique for determining hardness and elastic modulus using load and displacement sensing indentation experiments, *Journal of materials research* 7(6) (1992) 1564-1583.
- [26] V. Bhakhri, R.J. Klassen, The strain-rate dependence of the nanoindentation stress of gold at 300 K: A deformation kinetics-based approach, *Journal of Materials Research* 24(4) (2009) 1456-1465.
- [27] H.K. Zhang, Z. Yao, C. Judge, M. Griffiths, Microstructural evolution of CANDU spacer material Inconel X-750 under in situ ion irradiation, *Journal of Nuclear Materials* 443(1-3) (2013) 49-58.
- [28] H.J. Frost, M.F. Ashby, *Deformation mechanism maps: the plasticity and creep of metals and ceramics*, Pergamon press 1982.

- [29] D. Tabor, *The hardness of metals*, Oxford university press 2000.
- [30] Q. Wei, S. Cheng, K. Ramesh, E. Ma, Effect of nanocrystalline and ultrafine grain sizes on the strain rate sensitivity and activation volume: fcc versus bcc metals, *Materials Science and Engineering: A* 381(1-2) (2004) 71-79.
- [31] R. Klassen, B. Diak, S. Saimoto, Origin of the depth dependence of the apparent activation volume in polycrystalline 99.999% Cu determined by displacement rate change micro-indentation, *Materials Science and Engineering: A* 387 (2004) 297-301.
- [32] A. Elmustafa, M. Tambwe, D. Stone, Activation volume analysis of plastic deformation in fcc materials using nanoindentation, *MRS Online Proceedings Library Archive* 750 (2002).
- [33] A.H. Cottrell, R. Stokes, Effects of temperature on the plastic properties of aluminium crystals, *Proceedings of the Royal Society of London. Series A. Mathematical and Physical Sciences* 233(1192) (1955) 17-34.
- [34] R. Mulford, Analysis of strengthening mechanisms in alloys by means of thermal-activation theory, *Acta Metallurgica* 27(7) (1979) 1115-1124.
- [35] B.J. Diak, K.R. Upadhyaya, S. Saimoto, Characterization of thermodynamic response by materials testing, *Progress in materials science* 43(4) (1998) 223-363.

Chapter 5

5 Nano- scale kinetic deformation behavior of room temperature Ni⁺ irradiated Inconel X-750

Pyramidal constant loading rate nanoindentation tests were performed on Ni⁺ irradiated at $\psi_{Ni} = 0.1, 1, 5$ dpa at 25°C. The tests were performed over a range of loading rates ($\dot{P} = 0.3, 3.0, 30$ mNs⁻¹) to study the deformation behavior by assessment of changes in apparent activation energy $\Delta G_{Thermal}$, activation volume V^* , activation strength ΔG_0 and activation area Δa . We observed that $\Delta G_{Thermal}$ of the dislocations that either interfere with the glide of existing dislocations or represent sites for the nucleation of new dislocations decreased by increasing τ_{equiv} . Activation volume V^* increased as compared to as- received to $\psi_{Ni} = 0.1$ dpa by 8%. However, at $\psi_{Ni} = 1$ dpa is dropped by about 7% due to increased defect density. In addition, results in Δa has shown that the apparent activation area is decreased at $\psi_{Ni} = 1$ dpa as well. Collectively, these data suggest that, based upon the operative deformation mechanism, the strength of the dislocation–obstacle interactions that limit the rate of deformation could be attributed mainly due to disordering/dissolving of γ' precipitates.

5.1 Introduction

Radiation damage in materials used in nuclear industry is of a great concern. Performance prediction of super-alloys used in the nuclear industry is mainly defined by their mechanical properties degradation consequent to their operating environment. As such, over the past few decades, there has been a concerted effort to study the effect of irradiation on the mechanical properties of materials used in nuclear reactors [1-3]. Inconel X-750, a precipitation hardened Ni-based superalloy, with high strength, good creep properties and excellent corrosion resistance at high temperatures is currently used as spacer material in the CANada Deuterium Uranium (CANDU) heavy water reactor [4]. Mechanical examinations on X-750 spacers removed from CANDU reactors indicate an increased embrittlement, which depends on operation temperature and displacement damage caused by neutron irradiation, as well as lower load carrying capacity compared to the as-received condition [5, 6]. Microstructure instability and mechanical property degradation of

materials in nuclear environments are serious issues, hence understanding of the performance and failure mechanisms of reactor components is crucial. However, the testing reactor-irradiated materials has some limitations, including lengthy timescales and radioactive safety issues. Therefore, ion-beam irradiation has been developed as a proxy irradiation technique that allows materials evaluation under similar reactor condition but with the advantages of full control of irradiation parameters [7, 8]. Previous reports show that irradiation temperature, dose, and dose rate can affect microstructure of the material differently [8-10]. Further, in-situ TEM examination of heavy ion irradiated X-750 have revealed microstructural changes including the production of defects (stacking fault tetrahedra and dislocation loops) and γ' precipitate instability [8, 11, 12].

In addition, Zhang et al.[9] found that there is a critical temperature (~ 400 °C) for the disordering process and the γ' phase stays ordered under irradiation at temperatures higher than a critical point. One of the mechanical tests to study the effect of room temperature Ni^+ irradiation doses on deformation behavior of the X-750 is via investigating the strength of the dislocation/obstacle interactions.

During nano indentation testing the measured average σ_{ind} is significantly increased when the indentation depth (h) is less than several micrometers [13-15]. This has been explained in terms of the increased applied stress necessary for a dislocation to glide through the high density of ‘geometrically necessary dislocations’ required to accommodate the large localized strain gradients around submicrometric deep indentations [16, 17] or in terms of the increased stress necessary to nucleate dislocations from a small volume of metal, beneath the indentation, which may have no easy dislocation–nucleation sources. Either of these ‘glide limited’ or ‘nucleation limited’ mechanisms may affect the indentation stress σ_{ind} of shallow indentations compared to deep indentations. Simple dimensional analysis of a geometrically self-similar indentation, such as a pyramidal indentation, indicates that the average indentation strain rate $\dot{\epsilon}_{ind}$ must be directly dependent upon the ratio of the indentation velocity and the indent depth \dot{h}/h [18, 19]. Therefore, one would expect that, indentation strain rate ($\dot{\epsilon}_{ind}$) would become quite large when h is small.

However, constant load nano-indentation tests have been used to study the kinetics of plastic deformation of a variety of non-irradiated/ irradiated materials [14, 20-26] and the results of such tests are usually interpreted in terms of deformation occurring by a mechanism of dislocation glide limited by discrete obstacles distributed throughout the microstructure [27, 28]. The kinetics of γ' Ni based superalloy such as Inconel X-750 has not been reported.

Therefore, the objective of the present paper is to assess changes in $\Delta G_{Thermal}$, V^* , ΔG_0 , Δa consequent to damages induced by room temperature Ni^+ irradiation and the effect of γ' disordering /dissolution on Inconel X-750.

5.2 Experimental procedure

5.2.1 Material preparation and ion implantation

The chemical composition of the Inconel X-750 alloy used in this study was given in Table 3-1 in chapter 3. The alloy was annealed at 1010 °C (30 min) followed by air cooling to room temperature, cold working by 18%, and then ageing at 728 °C (16 h). The average grain size was found to be between 15 to 25 μm .

Three samples ($6 \times 6 \times 3$ mm) were cut by EDM from the aged X-750 material. The samples were mechanically ground with successively finer grit SiC impregnated papers and then polished in an aqueous slurry of 0.02 μm diameter colloidal SiO_2 . This process created a surface free of polishing-induced plastic deformation before helium implantation. Polished Inconel X-750 sample exposed to thirteen Ni^+ ion energy levels from 2 to 8 MeV were used at 25 °C to invoke different levels of irradiation damage at $\psi_{Ni} = 0, 0.1, 1, 5$ dpa (displacements per atom) while also obtaining a maximum implanted depth of around 3 μm . The Stopping Range of Ions in Matter (SRIM-2013) software, was used to calculate the average ion-induced crystal damage ψ using the Kinchin-Pease approximation [30]. Figure 5.1 depicts the variation of displacement damage versus target depth for different nickel beam energies to invoke levels of irradiation damage without significantly changing the chemical composition of the Ni-based alloy.

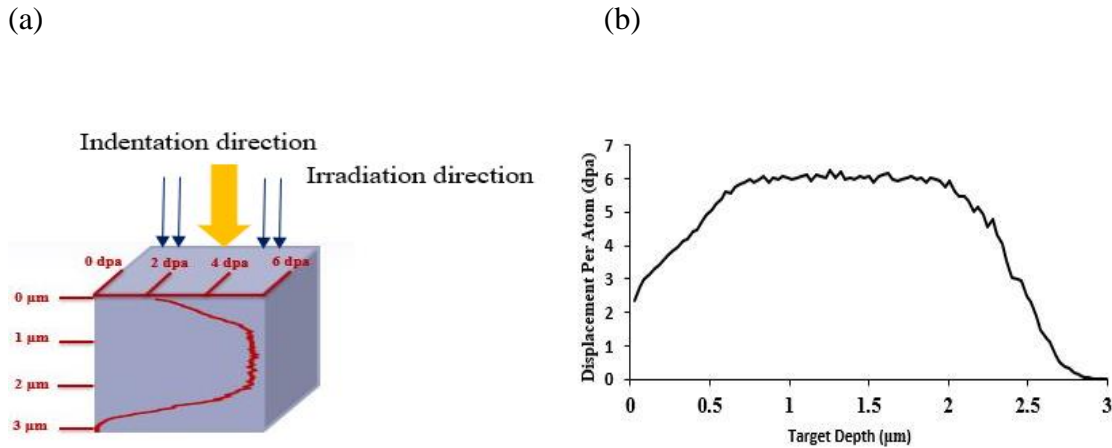


Figure 5.1: (a) Schematic illustration of irradiation and indentation direction with SRIM profile (b) Displacement damage profile versus target depth for samples irradiated up to $\psi_{Ni} = 5$ dpa.

5.2.2 Nano indentation testing

Room temperature nanoindentation tests were performed with a diamond Berkovich indenter on a NanoTest indentation testing platform made by Micro Materials Ltd (Wrexham, UK) [31, 32]. The Micro Materials NanoTest indenter works by measuring the indentation force and the indenter motion when it is in contact with the test material. The sequence begins by applying an increasing amount of force to the indenter to indent a polished sample to a predetermined force/depth at a defined loading rate [18, 33, 34]. The instrument was positioned on an anti-vibration base and was enclosed in a temperature-controlled cabinet. Indentation tests were performed at loading rates of $\dot{P} = 0.3, 3.0$ and 30 mNs^{-1} to a maximum load of 390 mN and max depth of $h_{max} = 1400 \text{ nm}$ in order to obtain σ_{ind} data as a function of h at different values of $\dot{\epsilon}_{ind}$. Three indentation tests were performed at each loading rate on each of the three-nickel ion irradiated samples each spaced 25 μm apart to ensure that the plastic zones of individual indentations did not overlap. Overall, twenty-seven indentation tests were performed in total.

A three-sided pyramidal diamond indenter (Berkovich) was used to perform the nanoindentation tests. This indenter had a tip radius of $R = 250.8 \text{ nm}$ as measured by scanning electron microscopy. In order to have a precise indenter tip, 15 nm of gold layer

was deposited at 0.1nm/s using the Angstrom Engineering electron beam evaporator. The effect of this spherical tip upon the actual projected area function $A(h)$ of a pyramidal indentation has been studied extensively [34-36]. The minimum indentation depth for self-similar deformation, projected indentation contact area and average indentation stress was calculated as from the load, P , and depth, h , data as in chapter 4 (section 4.3.1 and 4.3.3) where P is indentation load, h is instantaneous contact depth and R is indenter tip radius due to blunting at the tip (250.8 nm in our indenter), and C is sink-in/pile-up factor. The parameter C in the indentation stress equation was then determined experimentally by measuring, with scanning electron microscopy, the actual contact area. Actual contact area of an indentation of known depth was calculated and compared with the ideal projected area of an indentation of the same depth [20, 34, 37, 38]. For a pyramidal indentation where metal pile-up occurs, C is typically between 1 and 1.2 and should be independent of indentation depth, and in our study $C= 1.023$.

It should be noted that σ_{ind} is different from the indentation hardness values because it includes both the elastic and the plastic indentation depth, (i.e. $h_c = h_{plastic} + h_{elastic}$) in the calculated indentation area, whereas the conventional indentation hardness is calculated with the residual plastic depth (h_p).

5.2.3 Microstructure evaluation

Previously published data from Zhang et al. [11, 39] were adapted to explore the relation between kinetic deformation parameter V^* , ΔG_0 , and Δa determined in this study and the irradiation effect of Ni^+ on defect density. The data included microstructural changes examined from TEM results after Kr^{+2} at 60 °C irradiation at ($\psi_{Ni} = 0.01, 0.06, 0.27, 0.68, 2.7$ and 5.4 dpa) on Inconel X-750. In order to derive equivalent microstructural changes for the doses used in the current study, the original data were replotted and fitted with the best fit curve (polynomial second order) and equivalent microstructural values were calculated from the equation derived. Zhang et al. showed that there was a correlation between defect number density and heavy ion irradiation doses but not with the defect size

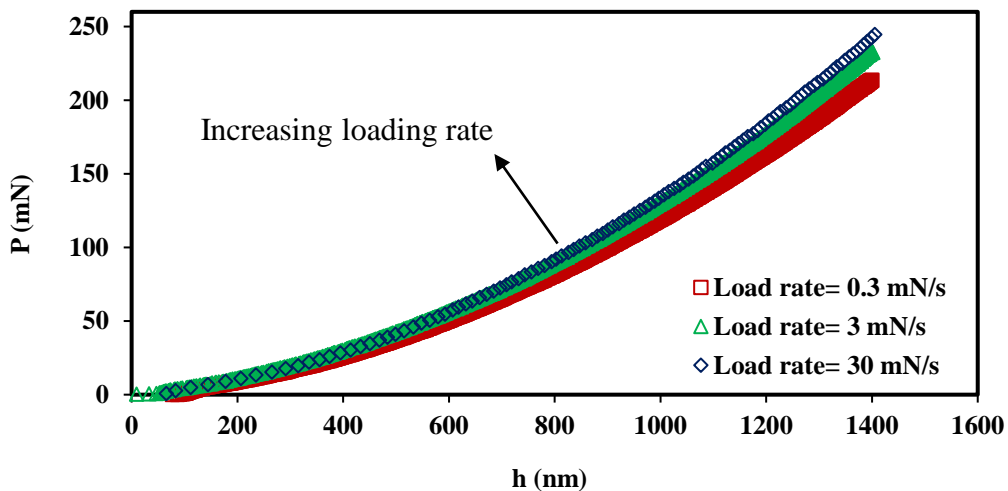
(SFT and dislocation loops) between 60 °C to 400 °C. Therefore, in this study we chose to show the most affected microstructural change with heavy ion irradiation meaning defect number density consequent to Ni⁺ irradiation.

5.3 Results

5.3.1 Indentation load -depth ($P-h$) plots

Figure 5.2 shows the curves of indentation force P versus depth h from tests performed under various levels of \dot{P} and irradiation damage. Although these figures do not show data from all the indentation tests performed in this study, the shape of the curves shown is typical of the other indentation tests performed. The magnitude of P_{max} at $\psi_{Ni} = 1$ dpa is higher compare to other doses which is approximately 255 mN at indentation depth of $h_{max} = 1400$ nm. This indicates the increased flow stress at $\psi_{Ni} = 1$ dpa is higher. At any given indentation depth, P increases with increasing loading rates indicating the strain rate sensitivity of the indentation stress.

(a)



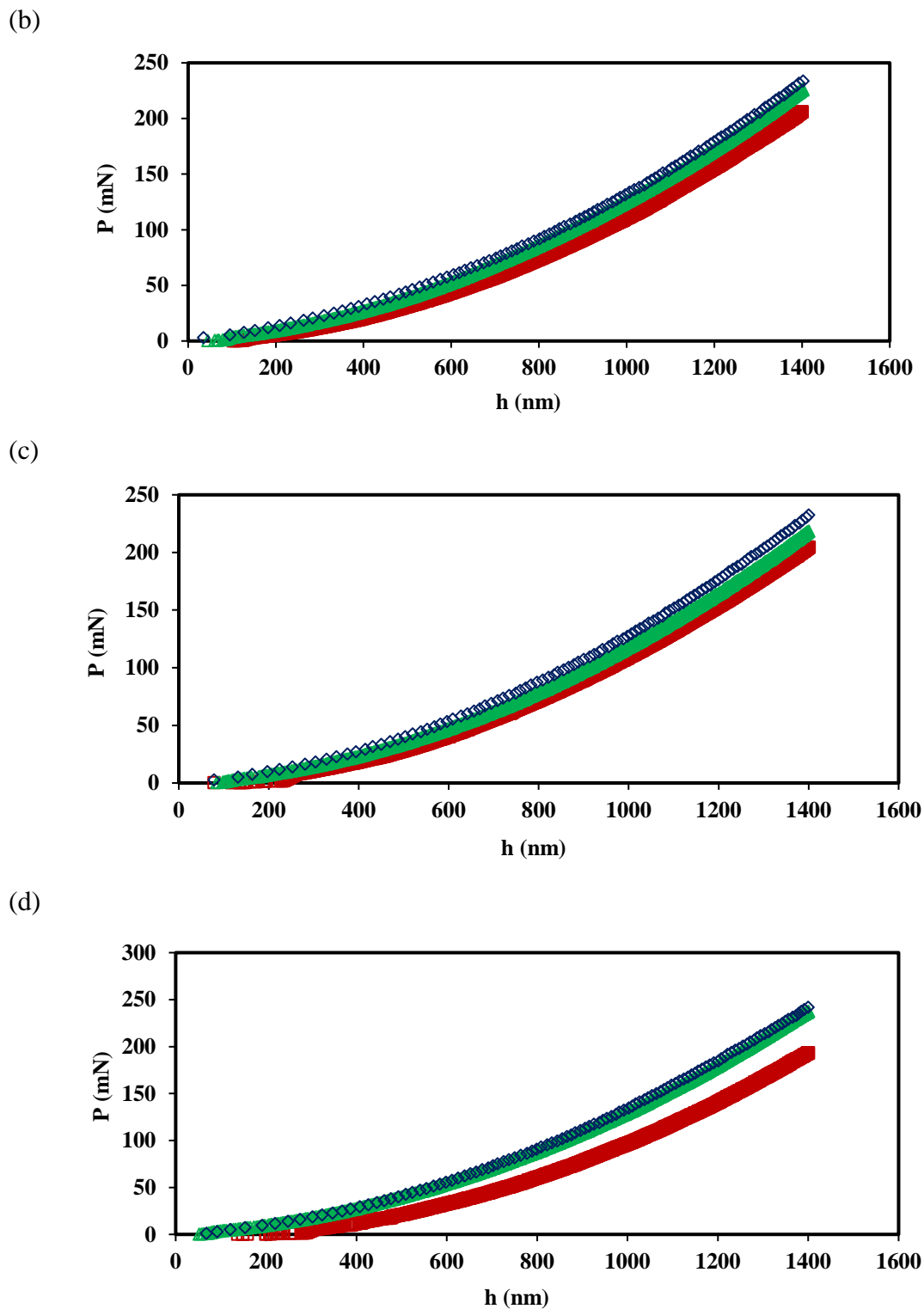


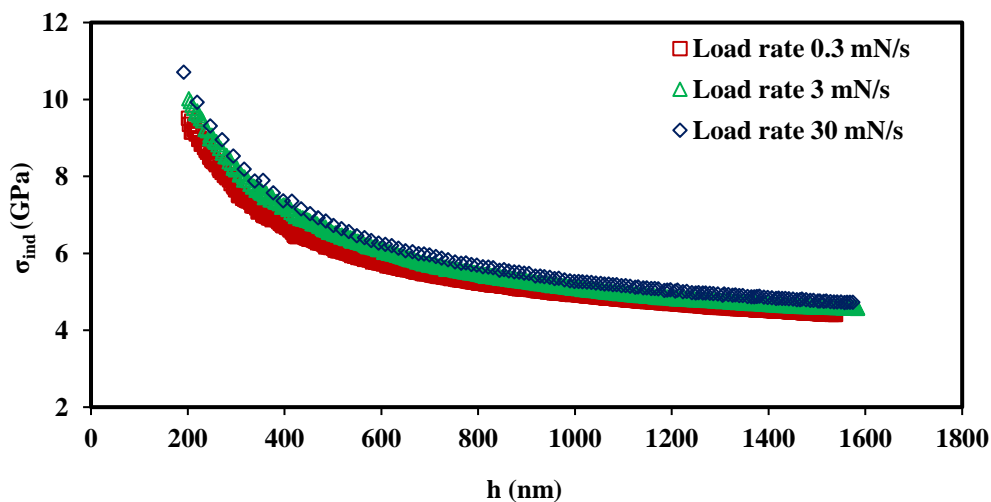
Figure 5.2: Representative indentation force P versus depth h curves for the tested Inconel X-750 alloy subjected to various levels of Ni^+ irradiation damages, in (a) $\psi_{\text{Ni}} = 0$ (b) $\psi_{\text{Ni}} = 0.1$ (c) $\psi_{\text{Ni}} = 1$ (d) $\psi_{\text{Ni}} = 5$.

5.3.2 Indentation depth dependence of σ_{ind}

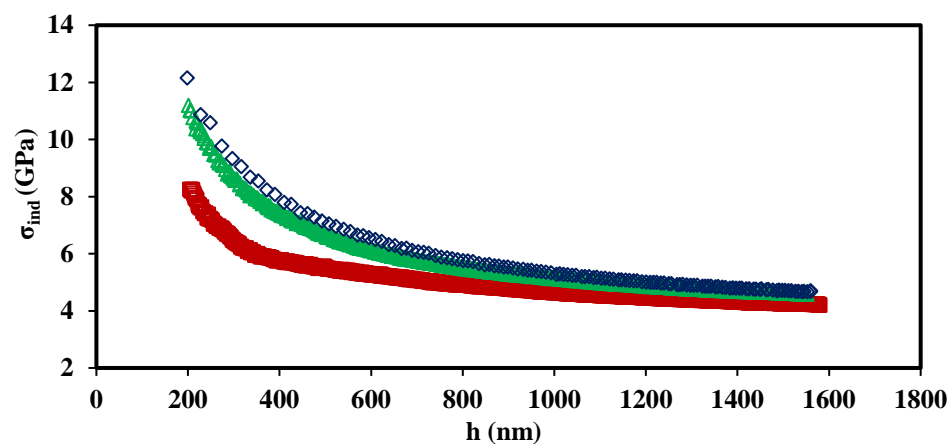
Figure 5.3 shows the average indentation stress σ_{ind} versus indentation depth h for as received and irradiated samples. We observed that for all the materials tested, for any given indentation depth, σ_{ind} increases when the loading (strain) rate increases. Also, σ_{ind} increases significantly when h is less than about 600 nm. For example, in the case of $\psi_{Ni} = 1$ dpa, σ_{ind} increased up to 7.30 GPa when $h = 400$ nm. The reason for considering the parameters measurement at 400 nm depth is to make sure that the measurements are carried out in the irradiated depth of sample.

If we assume that the plastic zone is 5 times bigger than the actual indent size [40] then for sampling just at the irradiated depth about 3 μm the indentation size should be less than 600 nm. In addition, the bigger the indentation size, the smaller the indentation size effect. Therefore, to avoid the effect of significant ISE on the indentation stress and strain estimation, the depth of 400 nm depth was chosen.

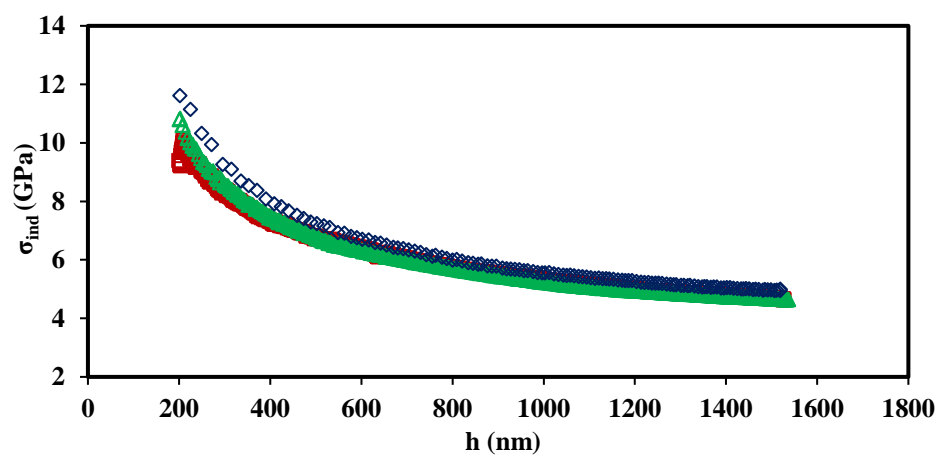
(a)



(b)



(c)



(d)

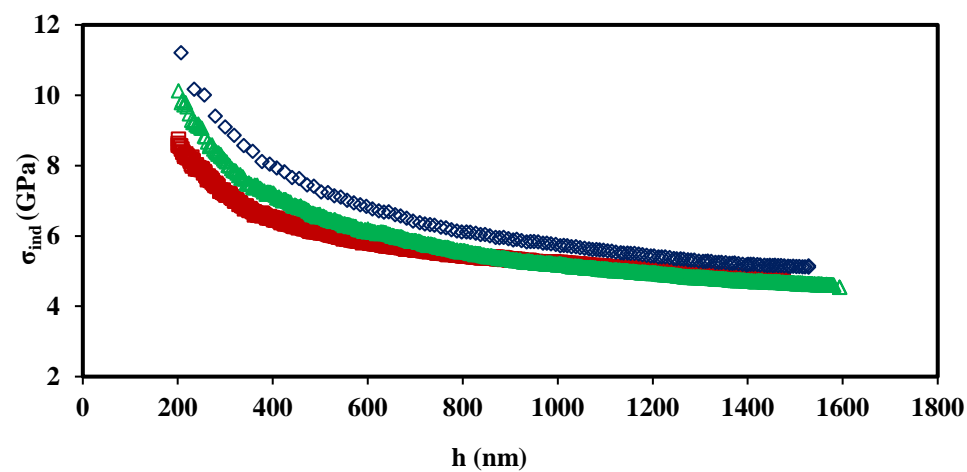


Figure 5.3: Average indentation stress σ_{ind} versus indentation depth for all levels of irradiation damage materials, indented at three loading rates, in (a) $\psi_{Ni} = 0$ (b) $\psi_{Ni} = 0.1$ (c) $\psi_{Ni} = 1$ (d) $\psi_{Ni} = 5$ dpa.

5.3.3 Indentation strain rate $\dot{\epsilon}_{ind}$ versus indentation depth, h

The average indentation plastic strain rate during indentation, $\dot{\epsilon}_{ind}$, is correlated to the indentation displacement, h , and the indentation displacement rate, $\frac{\partial h}{\partial t}$, as, $\dot{\epsilon}_{ind} =$

$$k \frac{\frac{\partial h}{\partial t}}{h} = k \frac{\dot{h}}{h}$$

where k is a geometrical constant, taken to be equal to 1 [37]. Figure 5.4 shows the variation in the average indentation strain rate, $\dot{\epsilon}_{ind}$, versus indentation depth, h , for as received Inconel X-750 indented at different loading rates. At each constant load rate $\dot{\epsilon}_{ind}$ shows a decreasing trend with increasing indentation depth, h .

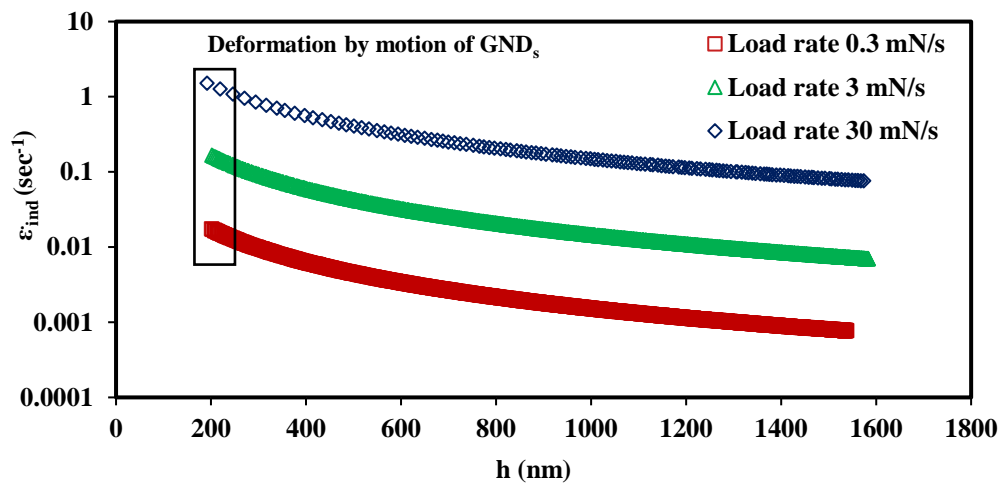


Figure 5.4: Apparent average indentation strain rate $\dot{\epsilon}_{ind}$ versus indentation depth for as received sample as indented at three loading rates. The shape of the curve is the same for the all irradiated Inconel X-750 at different dpa.

5.3.4 Indentation stress σ_{ind} indentation strain rate, $\dot{\epsilon}_{ind}$

Logarithmic plot of σ_{ind} versus $\dot{\epsilon}_{ind}$ at loading rate of $\dot{P} = 0.3$ mN/s, is shown in Figure 5.5 and indicates that the test materials all show a nonlinear logarithmic dependence of σ_{ind} upon $\dot{\epsilon}_{ind}$. Although this figure does not show data from indentation tests performed at the other loading rates, the shape of the curves shown is typical of the other indentation tests performed. The shape of the curves in Figure 5.5 is a characteristic of a deformation

process that is occurring by the mechanism of obstacle-limited dislocation glide. The gradual increase in σ_{ind} , when $\dot{\epsilon}_{ind}$ is greater than about 0.001 s^{-1} , reflects that the dislocation motion past obstacles is forced to occur at a rate that requires a combination from both thermal atomic vibration and applied stress with the amount of the necessary applied stress increasing with increasing $\dot{\epsilon}_{ind}$.

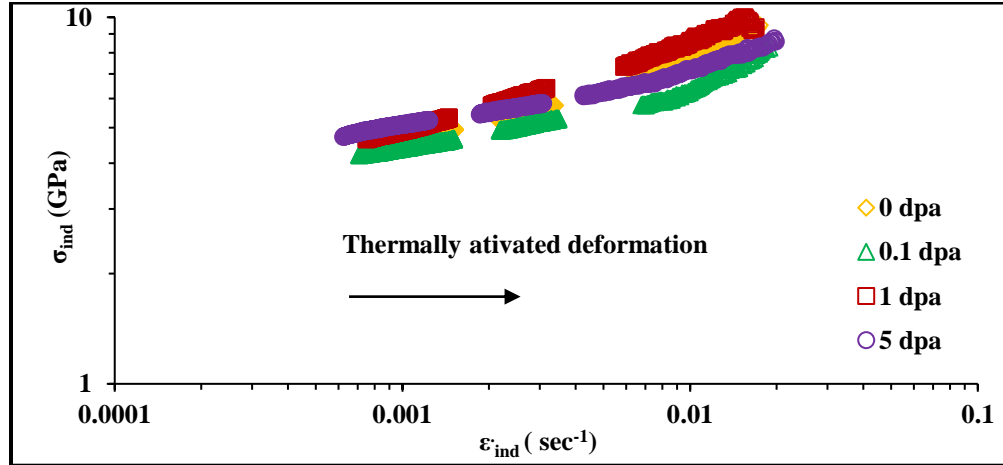


Figure 5.5: Logarithmic plot of σ_{ind} versus $\dot{\epsilon}_{ind}$ at loading rate of $\dot{P}=0.3 \text{ mN/s}$ for all samples.

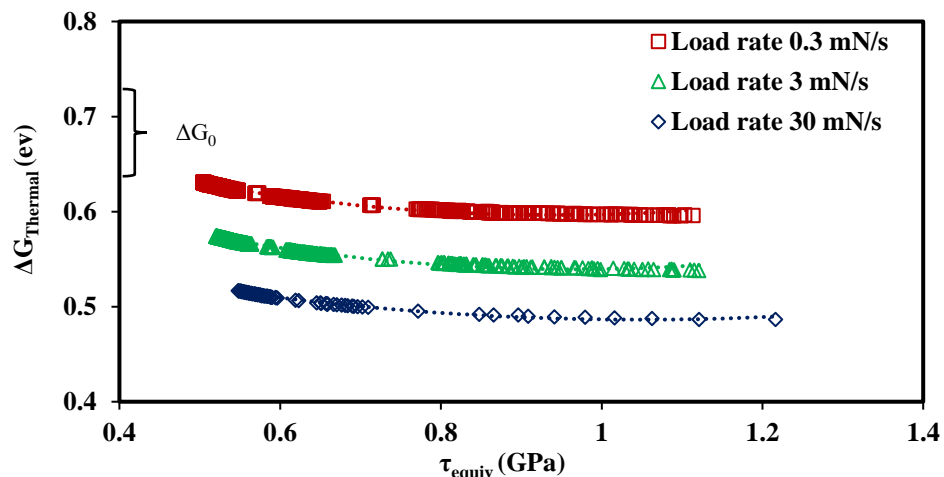
5.4 Discussion

5.4.1 Mechanism of indentation deformation

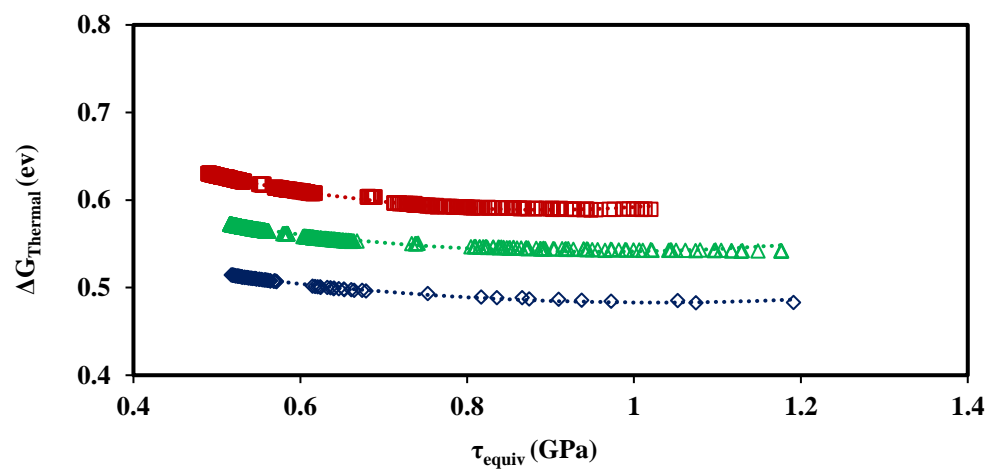
The results of our indentation tests performed at three levels of constant loading rate indicate that the indentation depth-dependence of the average indentation stress σ_{ind} is dependent upon irradiation damages (number of dpa) [24, 41] or work hardening of the materials [42, 43]. The experimental results shown in Figure 3 indicate that the indentation stress is a function of both indentation depth and indentation strain rate. Both dependencies reflect the nature of the dislocation – obstacle configuration at the various indentation depths in the Ni^+ irradiated Inconel X-750 at $25 \text{ }^\circ\text{C}$ in different conditions $\psi_{Ni} = 0.1, 1, 5 \text{ dpa}$. This dependence may arise from increased difficulty to glide a dislocation through irradiation induced defects in the indentation of plastic zone or the increased difficulty to nucleate a dislocation in the

region of a shallow, compared to a deep, indentation. Also, it is shown that the indentation size effect is expected to be influenced by prior dislocations and the additional irradiation damages that occurs during indentation. The Arrhenius-type equation describes the equivalent indentation shear strain rate $\dot{\gamma}$ that results in a single crystal when subjected to a constant applied shear stress τ [27] can be expressed as it was determined in (chapter 4, section 4.4.1). $\Delta G_{Thermal}(\tau_{equiv})$ is the stress dependent thermal activation energy required for a dislocation to overcome the rate limiting obstacles present within microstructure. In this study, we use the Tabor equation relating the uniaxial normal yield stress of a metal to approximately one third the indentation stress [44] as $\sigma_{equiv} \approx \frac{\sigma_{ind}}{3}$ we then convert this normal indentation stress to an equivalent shear stress by applying the Taylor factor typical of FCC metals, which allows us to determine $\dot{\gamma}_{equiv}$ (chapter 4, section 4.4.2). $\Delta G_{Thermal}(\tau_{equiv})$ is the thermal energy that must be supplied in order for (i) a dislocation to either overcome an obstacle that exists within the microstructure (i.e. a dislocation glide limited mechanism) or (ii) a new dislocation to be nucleated within the indented material (i.e. a dislocation nucleation limited mechanism). $\Delta G_{Thermal}(\tau_{equiv})$ is clearly stress dependent and will decrease when τ_{equiv} is large. Figure 5.6 shows $\Delta G_{Thermal}(\tau_{equiv})$ plotted versus τ_{equiv} for all the ψ_{Ni} conditions in the different loading rates studied. The fact that the dependence of $\Delta G_{Thermal}(\tau_{equiv})$ upon τ_{equiv} is dependent upon both h and ψ_{Ni} and indicates that the strength of the obstacle change with both parameters as $\Delta G_{Thermal}(\tau_{equiv})$ decreases with increasing τ_{equiv} .

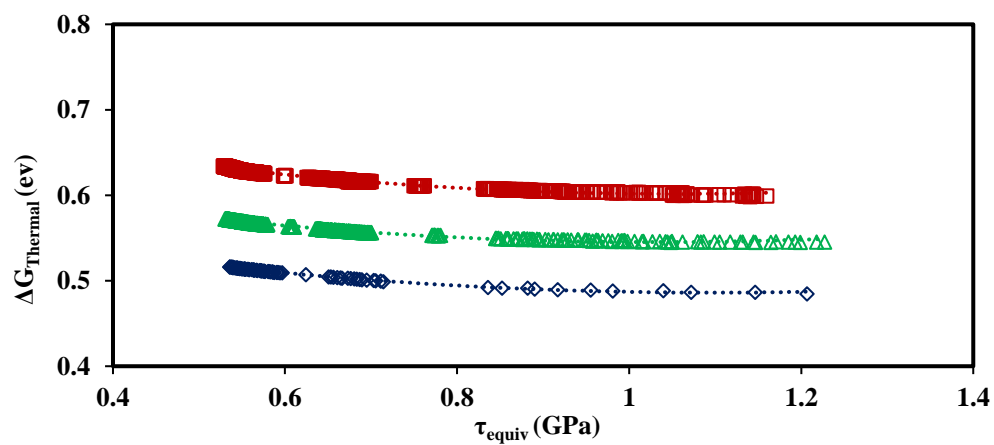
(a)



(b)



(c)



(d)

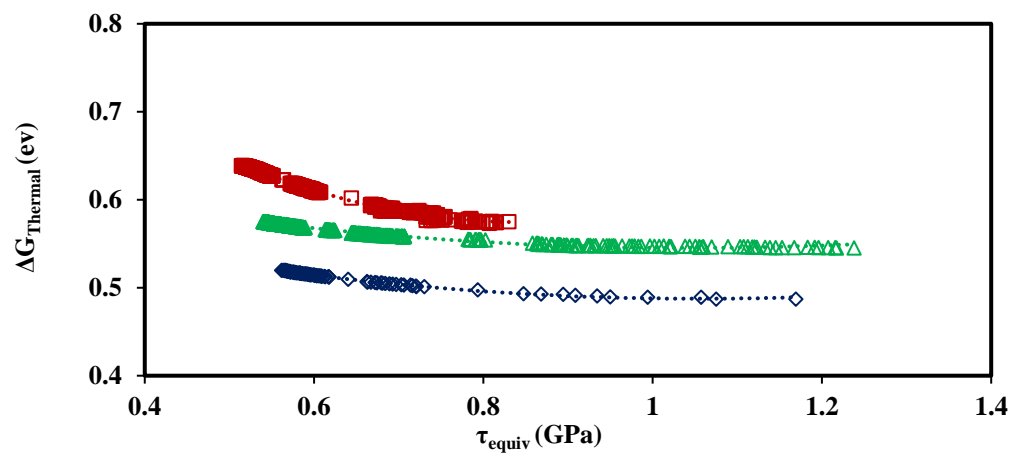


Figure 5.6: Plots of activation energy $\Delta G_{Thermal}$ versus τ_{equiv} for (a) $\psi_{Ni} = 0$ (b) $\psi_{Ni} = 0.1$ (c) $\psi_{Ni} = 1$ (d) $\psi_{Ni} = 5$ dpa.

It is believed that the induced damage during heavy ion irradiation revolves around two main mechanisms: ballistic mixing arising from collision cascade that leads to disordering of precipitates and dynamic reordering of the γ' phase during thermal recovery [45, 46]. Although ballistic dissolution can occur regardless of the temperature, higher temperatures will allow for an easier diffusion and hence re-formation of the precipitate [47]. Furthermore, irradiation to higher doses can change the chemical composition of the γ' phase. Indeed, diffusion of Ti and Al from the γ' structure to the matrix and of Cr and Fe from the matrix to the γ' phase occur at higher irradiation doses. EDX analysis of irradiated X-750 alloy show that 1 MeV Kr⁺ ion up to about $\psi_{Kr} = 5$ dpa can cause dissolution of γ' precipitates into the matrix [9].

5.4.2 Apparent activation strength and activation volume

Another deformation rate-controlling parameter that can be evaluated in order to identifying the underlying deformation mechanism is the activation volume V^* . V^* is obtained from derivative of $\Delta G_{Thermal}$ with respect to τ_{equiv} , [27, 48] as a result, it is common to express $\Delta G_{Thermal}(\tau_{equiv})$ in terms of a linear function of applied stress as in (chapter 4, section 4.4.4) was evaluated.

As ΔG_0 is the apparent activation strength of the obstacles that limit the dislocation motion. These are the fundamental parameters that describe the effectiveness of the microstructural obstacles at influencing the plastic deformation properties of the material. However, in this study we assumed that the average microstructure in the deforming region during indentation remains constant at a given indentation depth regardless of the magnitude of the loading rate. We have used $\Delta G_{Thermal}(\tau_{equiv})$ versus h data obtained from our experiments and, in doing so, calculated values of ΔG_0 and V^* for indentation tests performed on the as received and Ni⁺ irradiated samples, between 200-400, 600-800, and 1000-1400 nm depths.

By extrapolating the data trends of $\Delta G_{Thermal}(\tau_{equiv})$ versus τ_{equiv} in Figure 5.6 we can define $\Delta G_{Thermal}(\tau_{equiv})$ occurring at a very low $\tau_{equiv} \sim 0$ as the activation energy ΔG_0

of the obstacles that are limiting the dislocation nucleation– glide process. Figure 5.7 shows a down trend of ΔG_0 versus increasing defect density, as we speculate that the softening effect of γ' disordering/dissolution outweighed the hardening impact of irradiation-induced defects. Therefore, ΔG_0 decreased by increasing defect density.

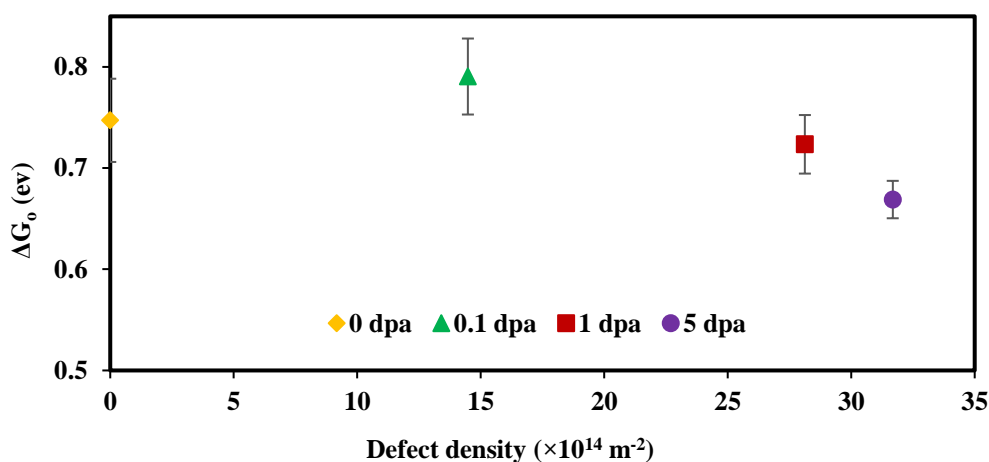


Figure 5.7: Apparent activation strength ΔG_0 of obstacles that limit dislocations glide versus defect density. Defect density data were determined from [11].

The ordered γ' precipitate is the main reason for the high strength of X-750 alloy, particularly at high temperatures; hence, γ' disordering/dissolution changes the deformation behavior and concurrently alters the mechanical properties of the superalloy. Based on a previous report, γ' precipitate disordering occurs after a low dose irradiation (0.06 dpa; ≤ 400 °C) [9] and at the higher implantation level, $\psi_{Ni} = 1$ dpa, a re-formation of Ti/Al rich regions are observed but in a disordered state (i.e. no super-lattice diffraction spots arise) [49]. Similar formation of precipitates at $\psi_{Ni} = 1$ dpa was previously reported, under similar ion implantation conditions (dose and temperature), and it starts to dissolve into the matrix at higher doses (~ 5 dpa) in other Ni superalloys [9, 50, 51].

Plot of Figure 5.8 the calculated apparent activation volume V^* , normalized with respect to the Burger vector ($b_{Ni} = 0.249$) nm [27]), versus indentation depth, for data from the indentation tests performed at the lowest loading rate, $\dot{P} = 0.3 \text{ mN}\cdot\text{s}^{-1}$. The data indicate that V^* increases with increasing indentation depth and the dependence of V^* upon indentation depth is in agreement with the findings from displacement rate change

indentation tests with findings from indentation tests performed on FCC and BCC metals [22, 38, 42, 43, 52-54].

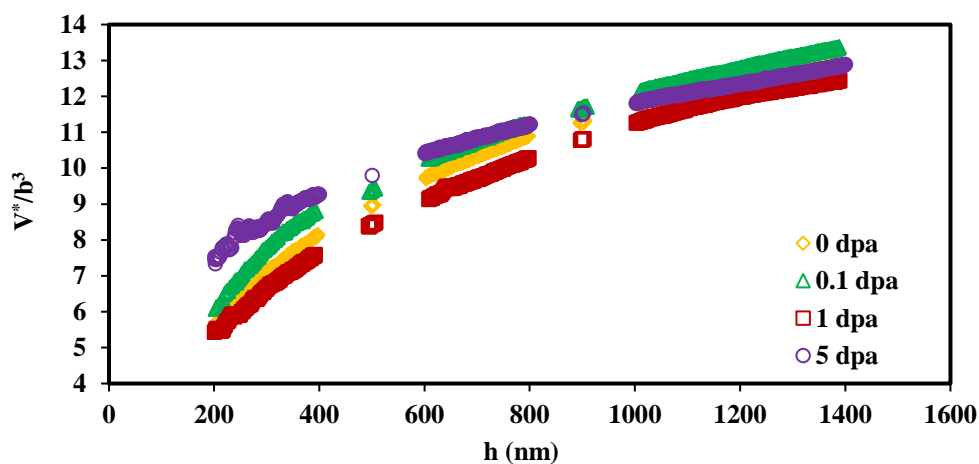


Figure 5.8: Normalized activation volume, V^*/b^3 , versus indentation depth for tests performed at $\dot{P} = 0.3$ mN/s for different conditions.

It is clear from the graph in Figure 5.9 that V^* decreases with increasing shear stress suggesting the inter-obstacle spacing of obstacles to the glide of dislocations is decreasing when the stress and dislocation density is increased which is in agreement of [14, 20, 42, 53]. The instability of the ordered phase during irradiation is basically attributed to cascade-induced ballistic mixing, but at higher irradiation temperature, a thermally activated reordering process occurs simultaneously and prevents phase instability [9].

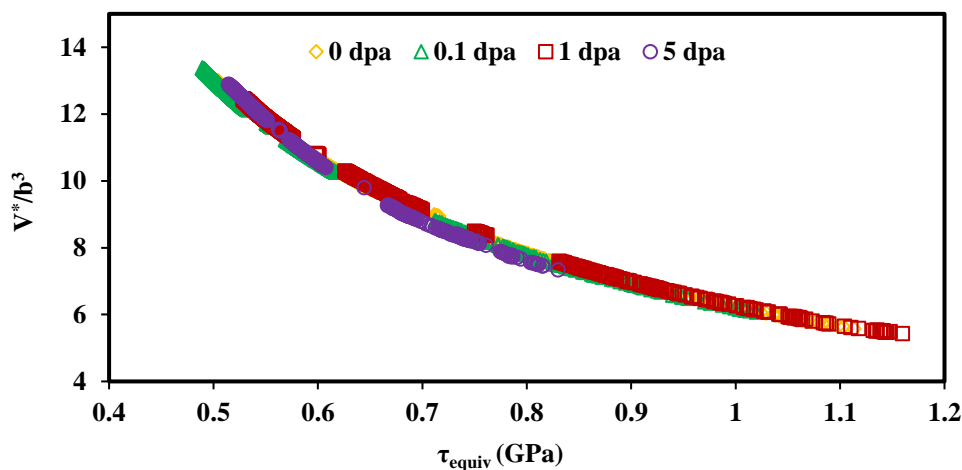


Figure 5.9: Normalized activation volume, V^*/b^3 , versus average indentation stress τ_{equiv} for tests performed at $\dot{P} = 0.3$ mN/s.

The relation between defect density and ψ_{Ni} at different doses is indicated in Figure 5.10 where defect density increases linearly up to $\psi_{Ni} = 1$ dpa and then starts to plateau (saturate) up to $\psi_{Ni} = 5$ dpa. However, this increased defect density doesn't seem to be the main mechanism behind deformation.

Because normalized activation volume versus defects density doesn't follow a linear relationship (Figure 5.11). This further and indirectly solidifies the dominant effect of γ' precipitates disordering/dissolution in deformation mechanism. At $\psi_{Ni} = 0.1$ dpa (400 nm nanoindentation depth) where density defects are increased (Figure 10), V^* is higher than that of as received sample (Figure 5.11). This is because, as it has been previously shown [9, 11], at $\psi_{Ni} = 0.1$ dpa γ' precipitates are disordered. Thereafter, between $\psi_{Ni} = 0.1$ and 1.0 dpa, the role of defect density becomes prominent and results in lower V^* compared with that of 0.1 dpa. In addition, $\psi_{Ni} = 5$ dpa has been shown to result in saturation of defects due to their overlaps where a balance was reached between formation and deconstruction of defects [11]. This together with the absence of γ' precipitates, results in higher V^* compared with those of all other doses.

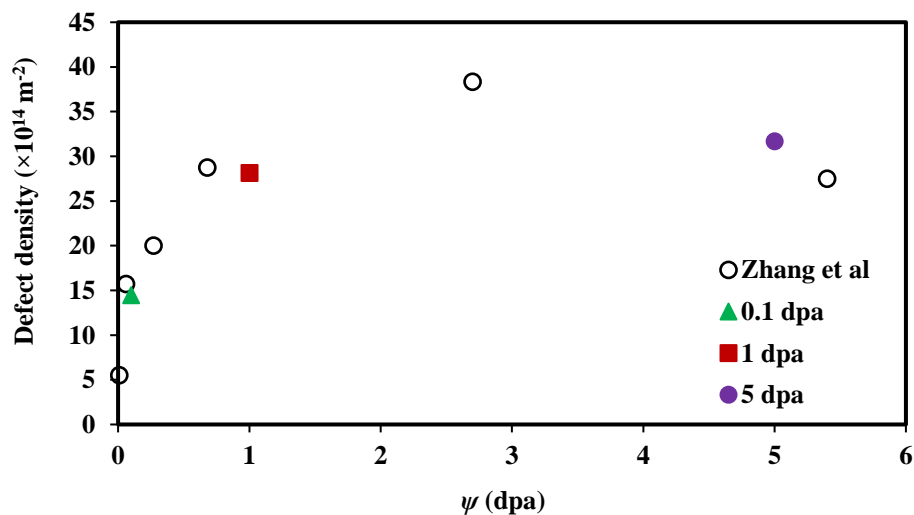


Figure 5.10: Defect density versus ψ_{Ni} (dpa) as defect density data is determined from [11].

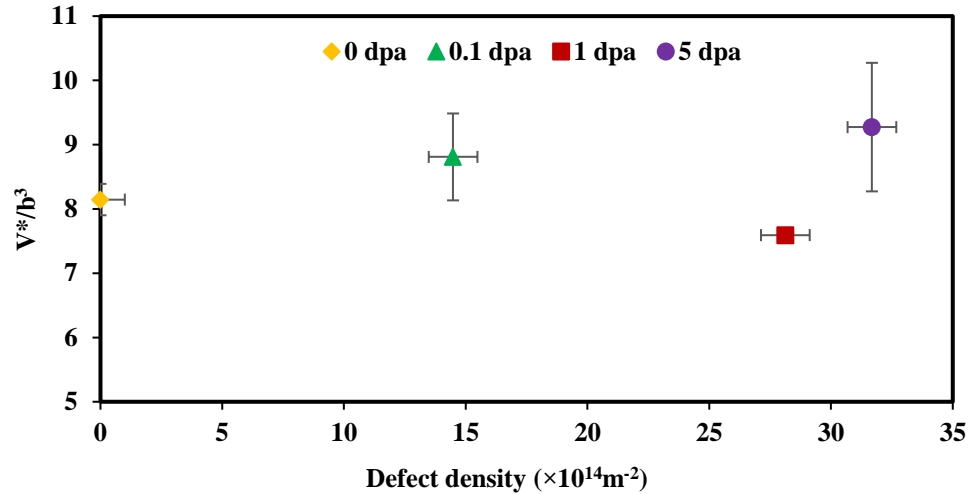
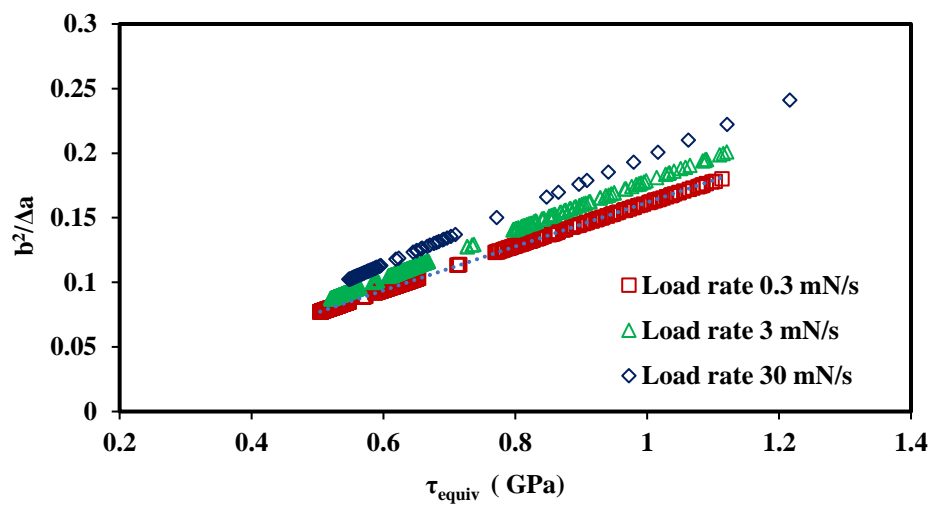


Figure 5.11. Normalized activation volume, V^*/b^3 versus defect density. Defect density data is extracted from [11].

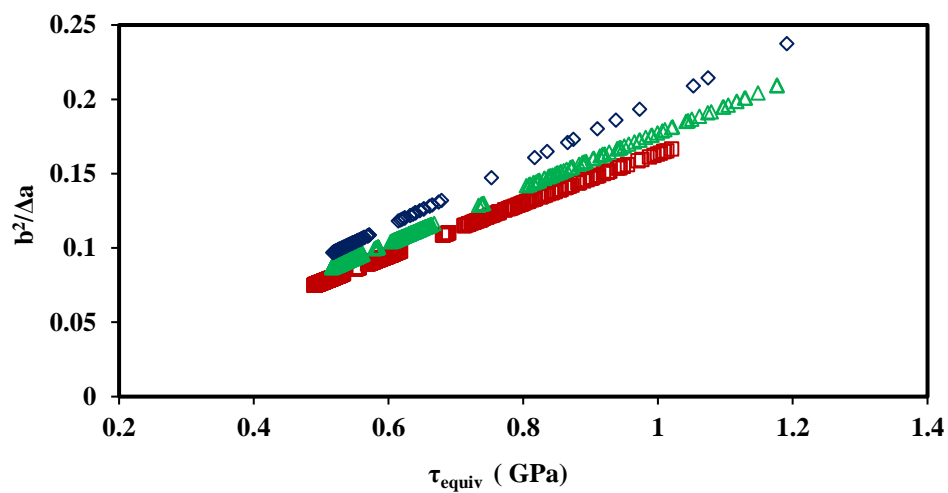
5.4.3 Haasen plot activation analysis

The Haasen plot is a graph of the experimentally determined inverse activation area, $1/\Delta a$, versus applied equivalent shear stress, τ_{equiv} [55, 56]. Linear trends of $1/\Delta a$ versus τ_{equiv} indicate that the plastic deformation in the test material occurs by a time-dependent obstacle-limited dislocation glide process (i.e. the Cottrell-Stokes law is maintained). Nonlinear trends in $1/\Delta a$ versus τ_{equiv} can arise from the cumulative effect of several types of obstacles to dislocation glide or to a changing microstructural state within the deformed test material. A Haasen plot intersecting the $1/\Delta a$ vertical axis indicates that the obstacle controlling the deformation process are rate sensitive “thermal” obstacles. The slope of this linear trend is inversely proportional to the mechanical activation work ΔW of the obstacles that limits the rate of dislocation glide [56]. Figure 5.12 shows plots of $b^2/\Delta a$ versus σ_{equiv}/M for the indentation tests performed on the Ni^+ irradiated and as received samples of Inconel X-750 between different indentation depths between 200-400, 600-800, and 1000-1400 nm for different loading rates. The data show essentially linear trends with the slope which is decreasing with increasing τ_{equiv} .

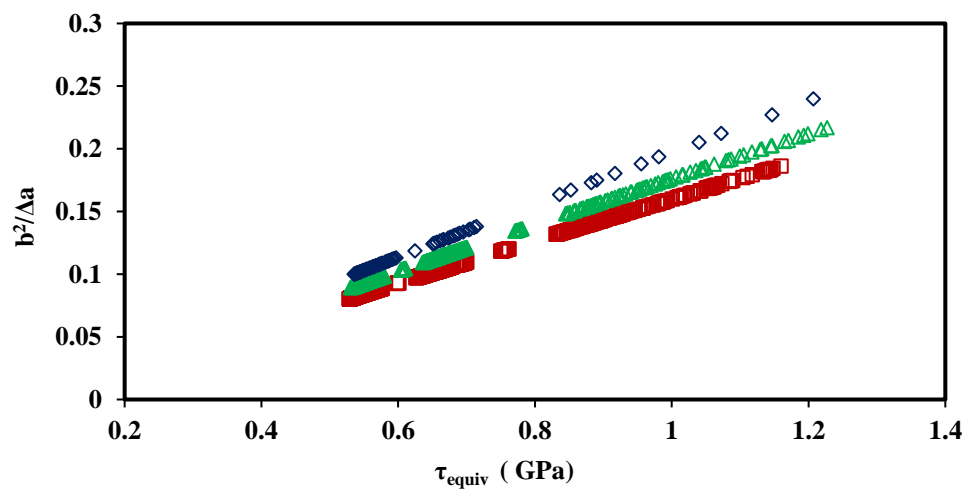
(a)



(b)



(c)



(d)

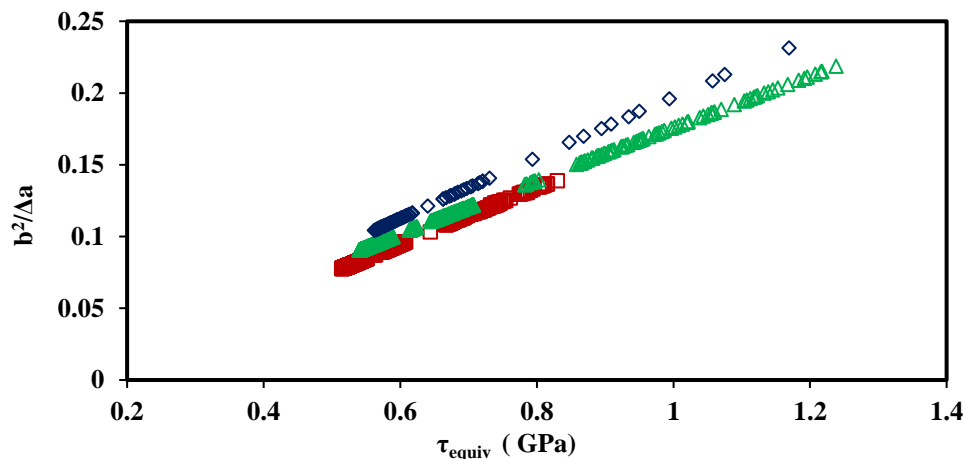


Figure 5.12: $b^2/\Delta a$ versus τ_{equiv} for the indentation test performed on (a) $\psi_{Ni}=0$ (b) $\psi_{Ni}=0.1$ (c) $\psi_{Ni}=1$ (d) $\psi_{Ni}=5$ dpa.

Figure 5.13 displays $b^2/\Delta a$ versus τ_{equiv} for different level of displacement damages ψ and as-received samples at 400 nm depth. As Hassen plot intersects the $b^2/\Delta a$ vertical axis that indicates the thermal obstacles (solute atoms) controlling the deformation process.

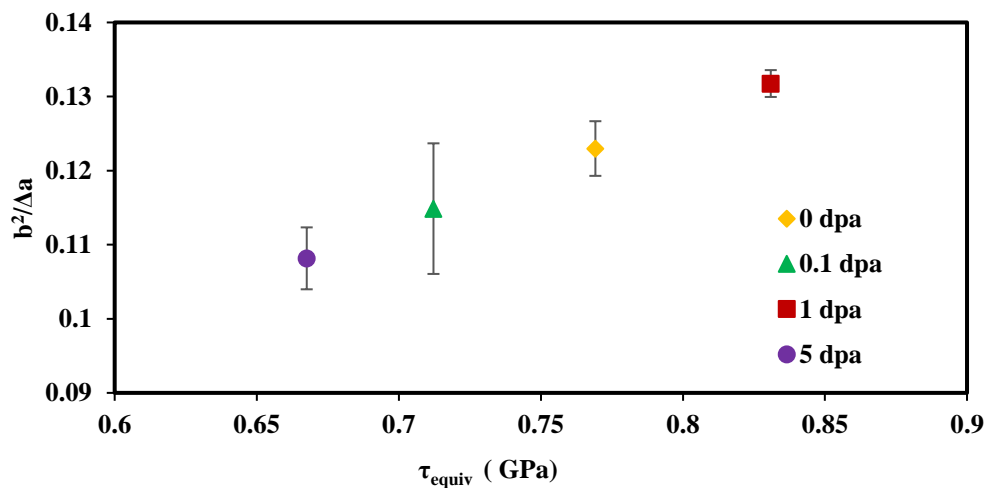


Figure 5.13: $b^2/\Delta a$ versus τ_{equiv} at 400 nm depth for different Ni^+ irradiated and as received samples.

In addition, Figure 5.14 indicates that the apparent activation area Δa is much smaller for $\psi_{Ni}=1$ dpa due to the irradiation hardening however, Δa increased at $\psi_{Ni}=5$ dpa due to start dissolution of γ' precipitate and saturation of defects.

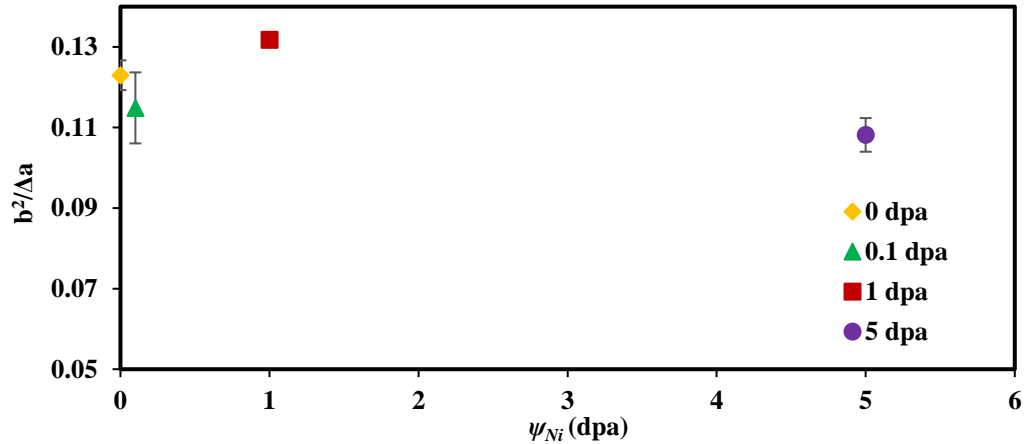


Figure 5.14: $b^2/\Delta a$ versus dpa for different levels and as-received samples at 400 nm depth.

5.5 Conclusion

The influence of room-temperature operative kinetic deformation behavior of Ni^+ irradiated of Inconel X-750 was investigated via changes in $\Delta G_{Thermal}$, ΔG_0 , V^* , and Δa . Our initial observation indicates that the indentation stress σ_{ind} is increased with decreasing indentation depth and increasing levels of Ni^+ ion irradiation. The depth dependence of the indentation stress is consistent with the theories that attribute this to the increased density of geometrically necessary dislocations around sub-nanometer indentations.

The $\Delta G_{Thermal}$ of the obstacles that either interfere with the glide of existing dislocations or represent sites for the nucleation of new dislocations was calculated and found to decrease by increasing τ_{equiv} . Consistently, there was a decreasing trend in ΔG_0 from 0.74 to 0.66 eV by increasing level of irradiation damages from as-received to 5 dpa. The trend shows that the softening effects of γ' precipitate overcome the irradiation hardening by increasing irradiation damages. In addition, V^* decreases with increasing stress suggesting that the inter-obstacle spacing of obstacles to the glide of dislocations is decreasing when

the stress and dislocation density is increased. Increase in defect density at $\psi_{Ni} = 1$ dpa results in lower V^* compared with that of $\psi_{Ni} = 0.1$ dpa. This is consistent with the idea of decreasing inter-obstacle spacing at 1 vs that of $\psi_{Ni} = 0.1$ dpa. However, at $\psi_{Ni} = 5$ dpa V^* and Δa are higher than $\psi_{Ni} = 0, 0.1, \text{ and } 1$ dpa as γ' precipitates at this dose is started to dissolve, and crystallographic defects are in saturated states.

5.6 Acknowledgements

The authors wish to thank the Natural Science and Engineering Research Council of Canada (NSERC) and the University Network of Excellence in Nuclear Engineering (UNENE) who provided financial support for this research. The assistance of Mr. Jack Hendriks at the Tandatron Ion Accelerator facilities at Western University (London, Ontario, Canada) for his support with performing ion implantations of the Inconel X7-50 samples. The assistance of Dr. T. Simpson at Western University Nanofabrication Laboratory in preparing the SEM images is gratefully acknowledged.

5.7 References

- [1] C. Sun, M. Kirk, M. Li, K. Hattar, Y. Wang, O. Anderoglu, J. Valdez, B. Uberuaga, R. Dickerson, S. Maloy, Microstructure, chemistry and mechanical properties of Ni-based superalloy Rene N4 under irradiation at room temperature, *Acta Materialia* 95 (2015) 357-365.
- [2] K. Jin, W. Guo, C. Lu, M.W. Ullah, Y. Zhang, W.J. Weber, L. Wang, J.D. Poplawsky, H. Bei, Effects of Fe concentration on the ion-irradiation induced defect evolution and hardening in Ni-Fe solid solution alloys, *Acta Materialia* 121 (2016) 365-373.
- [3] F. Long, L. Balogh, D.W. Brown, P. Mosbrucker, T. Skippon, C.D. Judge, M.R. Daymond, Effect of neutron irradiation on deformation mechanisms operating during tensile testing of Zr-2.5 Nb, *Acta Materialia* 102 (2016) 352-363.

- [4] H.K. Zhang, Z. Yao, G. Morin, M. Griffiths, TEM characterization of in-reactor neutron irradiated CANDU spacer material Inconel X-750, *Journal of Nuclear Materials* 451(1-3) (2014) 88-96.
- [5] C.D. Judge, N. Gauquelin, L. Walters, M. Wright, J.I. Cole, J. Madden, G.A. Botton, M. Griffiths, Intergranular fracture in irradiated Inconel X-750 containing very high concentrations of helium and hydrogen, *Journal of Nuclear Materials* 457 (2015) 165-172.
- [6] C. Judge, M. Griffiths, L. Walters, M. Wright, G. Bickel, O. Woo, M. Stewart, S. Douglas, F. Garner, Embrittlement of Nickel Alloys in a CANDU Reactor Environment
CANDU (CANadian Deuterium Uranium)® is a registered trademark of Atomic Energy of Canada Limited, *Effects of Radiation on Nuclear Materials: 25th Volume*, ASTM International 2013.
- [7] G. Was, Z. Jiao, E. Getto, K. Sun, A. Monterrosa, S. Maloy, O. Anderoglu, B. Sencer, M. Hackett, Emulation of reactor irradiation damage using ion beams, *Scripta Materialia* 88 (2014) 33-36.
- [8] H.K. Zhang, Z. Yao, M.R. Daymond, M.A. Kirk, Elevated temperature irradiation damage in CANDU spacer material Inconel X-750, *Journal of Nuclear Materials* 445(1-3) (2014) 227-234.
- [9] H.K. Zhang, Z. Yao, M.A. Kirk, M.R. Daymond, Stability of Ni₃(Al, Ti) gamma prime precipitates in a nickel-based superalloy inconel X-750 under heavy ion irradiation, *Metallurgical and Materials Transactions A* 45(8) (2014) 3422-3428.
- [10] P. Changizian, A. Brooks, Z. Yao, M. Daymond, Nano-scale Mechanical Properties and Microstructure of Irradiated X-750 Ni-Based Superalloy, *Metallurgical and Materials Transactions A* 49(2) (2018) 498-514.

- [11] H.K. Zhang, Z. Yao, C. Judge, M. Griffiths, Microstructural evolution of CANDU spacer material Inconel X-750 under in situ ion irradiation, *Journal of Nuclear Materials* 443(1-3) (2013) 49-58.
- [12] H. Zhang, Z. Yao, M.R. Daymond, M.A. Kirk, Cavity morphology in a Ni based superalloy under heavy ion irradiation with cold pre-injected helium. I, *Journal of Applied Physics* 115(10) (2014) 103508.
- [13] W.D. Nix, H. Gao, Indentation size effects in crystalline materials: a law for strain gradient plasticity, *Journal of the Mechanics and Physics of Solids* 46(3) (1998) 411-425.
- [14] V. Bhakhri, R. Klassen, The depth dependence of the indentation creep of polycrystalline gold at 300 K, *Scripta materialia* 55(4) (2006) 395-398.
- [15] G.Z. Voyiadjis, D. Faghihi, C. Zhang, Analytical and experimental determination of rate-and temperature-dependent length scales using nanoindentation experiments, *Journal of Nanomechanics and Micromechanics* 1(1) (2011) 24-40.
- [16] W.D. Nix, J.R. Greer, G. Feng, E.T. Lilleodden, Deformation at the nanometer and micrometer length scales: Effects of strain gradients and dislocation starvation, *Thin Solid Films* 515(6) (2007) 3152-3157.
- [17] D. Faghihi, G. Voyiadjis, Size effects and length scales in nanoindentation for body-centred cubic materials with application to iron, *Proceedings of the Institution of Mechanical Engineers, Part N: Journal of Nanoengineering and Nanosystems* 224(1-2) (2010) 5-18.
- [18] A.C. Fischer-Cripps, *Contact mechanics, Nanoindentation*, Springer2004, pp. 1-20.

- [19] Y. Champion, S. Nowak, Activation volume in fine grained metals from stress relaxation and nano-indentation, *Materials Science Forum*, Trans Tech Publ, 2008, pp. 399-404.
- [20] V. Bhakhri, R.J. Klassen, The strain-rate dependence of the nanoindentation stress of gold at 300 K: A deformation kinetics-based approach, *Journal of Materials Research* 24(4) (2009) 1456-1465.
- [21] B. Diak, S. Saimoto, Assessment of decomposition products in an Al–Mg–Si alloy by instrumented micro-indentation, *Materials Science and Engineering: A* 319 (2001) 909-913.
- [22] R. Klassen, B. Diak, S. Saimoto, Origin of the depth dependence of the apparent activation volume in polycrystalline 99.999% Cu determined by displacement rate change micro-indentation, *Materials Science and Engineering: A* 387 (2004) 297-301.
- [23] V. Bhakhri, R. Klassen, Investigation of high-temperature plastic deformation using instrumented microindentation tests. Part I The deformation of three aluminum alloys at 473 K to 833 K, *Journal of materials science* 41(8) (2006) 2259-2270.
- [24] B. Bose, R. Klassen, Effect of ion irradiation and indentation depth on the kinetics of deformation during micro-indentation of Zr–2.5% Nb pressure tube material at 25° C, *Journal of nuclear materials* 399(1) (2010) 32-37.
- [25] J. Böhmert, G. Müller, Thermally activated deformation of irradiated reactor pressure vessel steel, *Journal of nuclear materials* 301(2-3) (2002) 227-232.
- [26] E. Hasenhuettl, R. Kasada, Z. Zhang, K. Yabuuchi, A. Kimura, Ion-Irradiation Effect on Strain Rate Sensitivity of Nanoindentation Hardness of W Single Crystal, *Materials transactions* (2017) ML201603.

- [27] H.J. Frost, M.F. Ashby, Deformation mechanism maps: the plasticity and creep of metals and ceramics, Pergamon press 1982.
- [28] U.F. Kocks, A. AS, A. MF, Thermodynamics and kinetics of slip, (1975).
- [29] M. Griffiths, G. Bickel, S. Donohue, P. Feenstra, C. Judge, D. Poff, L. Walters, M. Wright, L. Greenwood, F. Garner, Degradation of Ni-alloy components in CANDU® reactor cores, Atomic Energy of Canada Limited, 2013.
- [30] J.F. Ziegler, M.D. Ziegler, J.P. Biersack, SRIM—The stopping and range of ions in matter (2010), Nuclear Instruments and Methods in Physics Research Section B: Beam Interactions with Materials and Atoms 268(11-12) (2010) 1818-1823.
- [31] J. Smith, S. Zheng, High temperature nanoscale mechanical property measurements, Surface Engineering 16(2) (2000) 143-146.
- [32] B.D. Beake, J.F. Smith, High-temperature nanoindentation testing of fused silica and other materials, Philosophical Magazine A 82(10) (2002) 2179-2186.
- [33] F.F.L.W.O. Winer, A.E. Bergles, G.A. Klutke, K.K. Wang, I. Finnie, J. Welty, M.D. Bryant, H.T. Yang, V.C. Mow, F.A. Leckie, Mechanical Engineering Series.
- [34] W.C. Oliver, G.M. Pharr, An improved technique for determining hardness and elastic modulus using load and displacement sensing indentation experiments, Journal of materials research 7(6) (1992) 1564-1583.
- [35] M.R. VanLandingham, T. Juliano, M. Hagon, Measuring tip shape for instrumented indentation using atomic force microscopy, Measurement Science and Technology 16(11) (2005) 2173.

- [36] X.G. Qiao, M.J. Starink, N. Gao, The influence of indenter tip rounding on the indentation size effect, *Acta Materialia* 58(10) (2010) 3690-3700.
- [37] K. McElhane, J.J. Vlassak, W.D. Nix, Determination of indenter tip geometry and indentation contact area for depth-sensing indentation experiments, *Journal of Materials research* 13(5) (1998) 1300-1306.
- [38] M. Haghshenas, A. Khalili, N. Ranganathan, On room-temperature nanoindentation response of an Al–Li–Cu alloy, *Materials Science and Engineering: A* 676 (2016) 20-27.
- [39] H. Zhang, Z. Yao, M.R. Daymond, M.A. Kirk, Cavity morphology in a Ni based superalloy under heavy ion irradiation with hot pre-injected helium. II, *Journal of Applied Physics* 115(10) (2014) 103509.
- [40] P. Hosemann, D. Kiener, Y. Wang, S.A. Maloy, Issues to consider using nano indentation on shallow ion beam irradiated materials, *Journal of Nuclear Materials* 425(1-3) (2012) 136-139.
- [41] B. Bose, R. Klassen, Temperature dependence of the anisotropic deformation of Zr–2.5% Nb pressure tube material during micro-indentation, *Journal of nuclear materials* 419(1-3) (2011) 235-240.
- [42] M. Haghshenas, R. Klassen, Indentation-based assessment of the dependence of geometrically necessary dislocations upon depth and strain rate in FCC materials, *Materials Science and Engineering: A* 586 (2013) 223-230.
- [43] M. Haghshenas, R. Klassen, Assessment of the depth dependence of the indentation stress during constant strain rate nanoindentation of 70/30 brass, *Materials Science and Engineering: A* 572 (2013) 91-97.
- [44] D. Tabor, *The hardness of metals*, Oxford university press 2000.

- [45] C. Abromeit, H. Wollenberger, S. Matsumura, C. Kinoshita, Stability of ordered phases under irradiation, *Journal of nuclear materials* 276(1-3) (2000) 104-113.
- [46] K. Russell, Phase instability under cascade damage irradiation, *Journal of nuclear materials* 206(2-3) (1993) 129-138.
- [47] P. Changizian, C. Lu, Z. Yao, L. Wang, Indentation behaviour of ion-irradiated X-750 Ni-based superalloy, *Philosophical Magazine Letters* 97(3) (2017) 101-109.
- [48] D. Kiener, Z. Zhang, S. Šturm, S. Cazottes, P.J. Imrich, C. Kirchlechner, G. Dehm, Advanced nanomechanics in the TEM: effects of thermal annealing on FIB prepared Cu samples, *Philosophical Magazine* 92(25-27) (2012) 3269-3289.
- [49] M.N. Tawfeeq, R.J. Klassen, Ni⁺ and He⁺ Implantation Effects on the Hardness and Microstructure of Heat-Treated X750 Superalloy.
- [50] C. Abromeit, S. Müller, N. Wanderka, Stability of γ' phase in the stoichiometric Ni₃Al alloy under ion irradiation, *Scripta metallurgica et materialia* 32(10) (1995) 1519-1523.
- [51] F. Bourdeau, E. Camus, C. Abromeit, H. Wollenberger, Disordering and dissolution of γ' precipitates under ion irradiation, *Physical Review B* 50(22) (1994) 16205.
- [52] Q. Wei, S. Cheng, K. Ramesh, E. Ma, Effect of nanocrystalline and ultrafine grain sizes on the strain rate sensitivity and activation volume: fcc versus bcc metals, *Materials Science and Engineering: A* 381(1-2) (2004) 71-79.
- [53] A. Elmustafa, M. Tambwe, D. Stone, Activation volume analysis of plastic deformation in fcc materials using nanoindentation, *MRS Online Proceedings Library Archive* 750 (2002).

[54] M. Haghshenas, L. Wang, R. Klassen, Depth dependence and strain rate sensitivity of indentation stress of 6061 aluminium alloy, *Materials Science and Technology* 28(9-10) (2012) 1135-1140.

[55] A.H. Cottrell, R. Stokes, Effects of temperature on the plastic properties of aluminium crystals, *Proceedings of the Royal Society of London. Series A. Mathematical and Physical Sciences* 233(1192) (1955) 17-34.

[56] R. Mulford, Analysis of strengthening mechanisms in alloys by means of thermal-activation theory, *Acta Metallurgica* 27(7) (1979) 1115-1124.

Chapter 6

6 Conclusions and Future Scope

6.1 Conclusions

The research presented in this dissertation aims to understand the degradation mechanism of mechanical properties and fundamental kinetic deformation of CANDU spacers made of Inconel X-750 in the non-irradiated and irradiated conditions under different temperatures and doses. This dissertation has attempted to overcome this scarcity of data by providing a series of fundamental investigations, involving the use of novel study designs of grain by grain nanoindentation hardness and constant-load pyramidal indentation testing to assess the time dependent plastic deformation parameters of Inconel X-750 for different doses. In addition, results were compared with the microstructure derived from previously published data to better explain the mechanisms involved in deformation.

In the first study (Chapter 3) both He^+ and Ni^+ implantation-induced hardening on Inconel X-750 was investigated by using grain by grain and random series nano-indentation. Results indicated a softening effect on the X-750 alloy at lower doses ($C_{\text{He}}= 100$ appm and $\psi_{\text{Ni}}= 0.01$ and 0.1 dpa). This might be attributed to the diffusion of He^+ atoms to dislocations, and precipitate-matrix interfaces at $300\text{ }^\circ\text{C}$ (100 appm) and disordering of γ' precipitates at $25\text{ }^\circ\text{C}$ (0.01 and 0.1 dpa) corresponding to (~10% reduction in hardness). With He^+ implantation ($300\text{ }^\circ\text{C}$) at 1000, and 5000 appm, the indentation hardness increased due to production of larger cavity size and density. Characteristic depth (h^*) is less pronounced in He^+ compared to Ni^+ implanted samples which can be attributed to the fact that accumulated helium resides as nano-bubbles within the microstructure and act as statistically stored obstacles to dislocation movement. Although the Ni^+ induced statistically stored defect density (i.e. dislocation loops and stacking fault tetrahedra) increase continuously with increasing dpa, the concurrent effect of Ni^+ induced γ' phase disordering, which occurs in this alloy at low doses of dpa, decreases the overall statistically stored dislocation density.

In the subsequent study (Chapter 4), constant-load pyramidal nanoindentation tests were performed on He⁺ implanted $C_{He} = 100, 1000, 5000$ appm at 300 °C Inconel X-750. The tests were performed over a range of loading rates $\dot{P} = 0.3, 3.0, 30$ mNs⁻¹ to study the operative dislocation-obstacle mechanisms by assessment of changes in dislocation thermal energy and activation strength of the obstacles. Such an investigation can lead one to answer whether helium implantation in a nickel based super alloy such as Inconel X-750 lead to markedly change rate-sensitivity of plastic flow? If so, what are the mechanistic contributions to such rate-sensitivity of deformation? Our initial observation indicates that the indentation stress σ_{ind} is increased with decreasing indentation depth and increasing levels of He⁺ ion implantation where the depth dependence of the indentation stress is consistent with that predicted by the theories that attribute this to the increased density of geometrically necessary dislocations around sub-nanometer indentations. It has been observed that the calculated apparent thermal activation energy of dislocations ($\Delta G_{Thermal}$) that either interfere with the glide of existing dislocations or represent sites for the nucleation of new dislocations, decrease by increasing τ_{equiv} . The constant load nanoindentation testing results from Inconel X-750 showed that the activation strength ΔG_0 of the deformation rate controlling obstacles depends upon He⁺ concentrations and there was a clear increasing uptrend in strength of the obstacles (ΔG_0 with increasing He⁺ dose up to $C_{He} = 5000$ appm . This is in line with microstructure changes showing that both cavity size and density is similarly increased by increasing He⁺ doses. Linear trends of $b^2/\Delta a$ versus τ_{equiv} indicated that the plastic deformation occurs by thermally activated time-dependent obstacle-limited dislocation glide process. Furthermore, at higher helium concentration activation volume (V^*) decreases with increasing stress, suggesting that the inter-obstacle spacing of obstacles to the glide of dislocations is decreasing when the stress and dislocation density is increased. and also, we observed that at higher helium concentration, apparent activation area (Δa) is much smaller compared to as-received sample.

Next study (Chapter 5) investigated the influence of room-temperature operative kinetic deformation behavior of heavy Ni⁺ irradiation on Inconel X-750 via changes in apparent thermal activation energy ($\Delta G_{Thermal}$), thermal activation strength (ΔG_0), and activation

volume(V^*). This is confirmed by our observation that the $\Delta G_{Thermal}$ of the obstacles was found to decrease by increasing τ_{equiv} . Consistently, there was a decreasing trend in ΔG_0 from 0.74 to 0.66 eV by increasing level of irradiation damages. In addition, V^* decreases with increasing stress. Increase in defect density at $\psi_{Ni}=1$ dpa results in lower V^* compared with that of $\psi_{Ni}=0.1$ dpa. This is consistent with the idea of decreasing inter-obstacle spacing at $\psi_{Ni}=1$ versus that of $\psi_{Ni}=0.1$ dpa. However, at $\psi_{Ni}=5$ dpa V^* and Δa are higher than $\psi_{Ni}=0, 0.1, \text{ and } 1$ dpa as γ' precipitates at this dose is started to dissolve, and crystallographic defects are in saturated states.

Pyramidal constant-load nano indentation in chapter 4, and 5 shows that σ_{ind} (in all irradiated tested materials) is clearly depth dependent. This dependency results from an increase in the local dislocation density (GND_s) around shallow, compared to deep, indentations, irradiation damages (via defect density) and helium accumulation (via cavity size and density). Nano-indentation testing is, therefore, a consistent and systematic technique to explain the micro/nano mechanical behavior and mechanisms (i.e. in terms of size effect, dislocation's motion and interaction, activation energy, activation volume, strength and type of dislocations limited obstacles) occurring during irradiation.

6.2 Suggestion for future work

The mechanical properties, and fundamental deformation parameters via grain by grain nano indentation hardness and pyramidal constant load testing of Inconel X-750 implanted by different levels of ions (He^+ and Ni^+) have been investigated for the first time. As a result, there are many remaining, open ended questions, which warrant continued research to help explain. The work presented in this dissertation is only a small part of a large, ongoing, industrial research program. There are some recommendations which are introduced here as future works:

1. In our study, we used two mechanical testing techniques (nanoindentation and pyramidal constant load testing) to assess the X-750 hardness and the deformation parameters before and after irradiation. In future work, it will be useful to the nuclear research community if a known oriented single crystal micro pillars compression test can be used to investigate the uniaxial stress state across the whole

sample in irradiated and non-irradiated conditions. This method delivers a direct stress-strain curve and offers the possibility for in situ observation of the sample deformation, thus allowing for a direct determination of the deformation mechanisms.

2. In a constant-load nano indentation test, the strain rate is not constant (i.e. strain rate non-linearly diminishing with indentation load or depth). It is, therefore, difficult to directly convert a constant loading rate to a representative strain rate which might be a more useful parameter than loading rate for analyzing deformation based on the microstructure. However, most of the indentation experiments in the previous works were made under constant load rate condition probably due to the instrumental limitations.
3. Performing constant strain rate nano indentation testing to assess the step-by-step plastic deformation parameters and investigate the interaction between dislocation and radiation defects, and cavities may help us to understand the failure mechanism much deeper on neutron irradiated X-750.
4. In addition to helium, significant amount of hydrogen is formed as a result of transmutation reaction within the X-750 alloy during service in the CANDU reactor. Therefore, investigating the effect of hydrogen implantation on mechanical response and also cavity distribution may be valuable.
5. Finite Element (FE) analysis methods to predict the local stress and plastic strain distributions within irradiation plastic zone and then predicting the onset of cracking in the Inconel X-750 will be very useful. Developing a suitable material damage model, i.e. defining damage initiation criteria and damage evolution mechanisms, may be one of the key aspects in the FE simulation of cracking failures.

Curriculum Vitae

Name: Loabat Shojaei-Kavan

Post-secondary Education and Degrees: Western University
London, Ontario, Canada
2010-2014 B.Eng

Western University
London, Ontario, Canada
2015-2016 M.Eng

Western University
London, Ontario, Canada
2016-2021 Ph.D.

Honours and Awards: Western Engineering Scholarship
2016-2020

Province of Ontario Graduate Scholarship
2018-2019

Related Work Experience: Teaching Assistant
The University of Western Ontario
2016-2020

Research Scientist
Canadian Nuclear Laboratories (CNL)
2020- present

Publications:

Loabat S. Kavan, Abhijeet Wadkar, Samuel F. Asokanthan “Computational Study of Onset Dynamics in Neuron-Spiking with Threshold Adaptation”. ASME 2018 International Mechanical Engineering Congress and Exposition. American Society of Mechanical Engineers Digital Collection, 2018.

Loabat S. Kavan, R.J. Klassen, “Effect of high temperature He⁺ and room temperature Ni⁺ implantation on grain by grain indentation hardness of Inconel X-750”, Will be submitted to the journal of Philosophical Magazine A.

Loabat S. Kavan, R.J. Klassen, “Effect of high temperature He⁺ implantation on the kinetic deformation nanoindentation of Inconel X-750”, Will be submitted to the journal of Material Science and Engineering A.

Loabat S. Kavan, R.J. Klassen, “Nano- scale kinetic deformation behavior of room temperature Ni⁺ irradiated Inconel X-750” Will be submitted to the journal of Material Science and Engineering A.

Conference Presentations

Maisaa N. Tawfeeq, **Loabat S. Kavan**, Robert J. Klassen, Poster presentation in “12th CANDU owners Group Fuel Channel”, May 2017, Toronto, Ontario, Canada.

Loabat S. Kavan, R.J. Klassen, poster presentation in the “Nuclear Materials Conference (NuMat)”, October 2018, Seattle, WA, USA.

Loabat S. Kavan, Abhijeet Wadkar, Samuel F. Asokanthan, poster presentation in “The American Society of Mechanical Engineers (ASME)”, November 2018, Pittsburgh, PA, USA.

Loabat S. Kavan, R.J. Klassen, oral presentation in the “Canadian Society for Mechanical Engineering (CSME)”, June 2019, London, Ontario, Canada.